

RD-A175 267

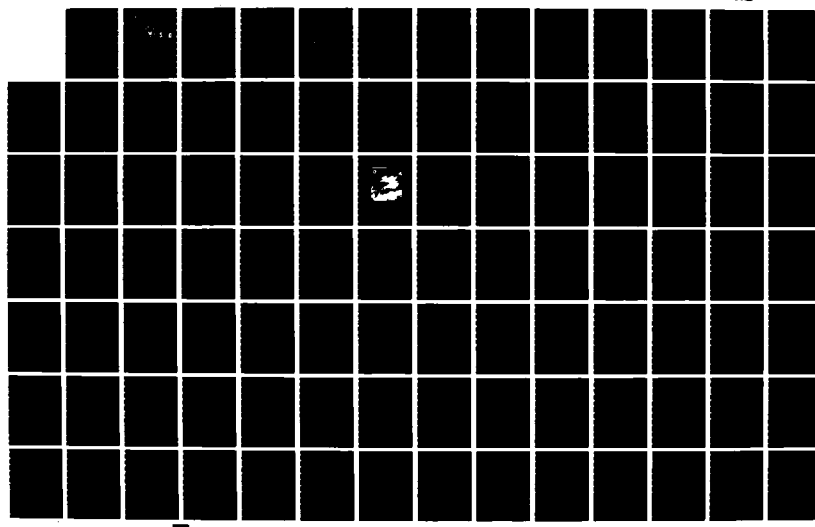
A NUMERICAL SIMULATION OF THE MEI-YU FRONT AND THE  
ASSOCIATED LOW-LEVEL JET(U) NAVAL POSTGRADUATE SCHOOL  
MONTEREY CA L C CHOU SEP 86

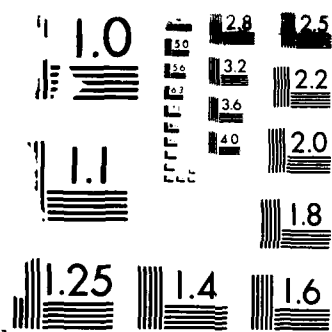
1/2

UNCLASSIFIED

F/G 4/2

NL





MICROSCOPY RESOLUTION TEST CHART

AD-A175 267

(2)

# NAVAL POSTGRADUATE SCHOOL

## Monterey, California



DTIC  
ELECTED  
DEC 24 1986  
S D

# THESIS

A NUMERICAL SIMULATION OF THE MEI-YU  
FRONT AND THE ASSOCIATED LOW-LEVEL JET

by

Lang C. Chou

September 1986

Thesis Advisors:

Dr. C. P. Chang  
Dr. R. T. Williams

Approved for public release, distribution unlimited

DTIC FILE COPY

## REPORT DOCUMENTATION PAGE

1a REPORT SECURITY CLASSIFICATION <b>UNCLASSIFIED</b>		1b. RESTRICTIVE MARKINGS			
2a SECURITY CLASSIFICATION AUTHORITY		3 DISTRIBUTION/AVAILABILITY OF REPORT Approved for public release; distribution is unlimited.			
2b DECLASSIFICATION/DOWNGRADING SCHEDULE		4 PERFORMING ORGANIZATION REPORT NUMBER(S)			
5 PERFORMING ORGANIZATION REPORT NUMBER(S)		6. MONITORING ORGANIZATION REPORT NUMBER(S)			
6a. NAME OF PERFORMING ORGANIZATION Naval Postgraduate School	6b OFFICE SYMBOL (If applicable) 63	7a. NAME OF MONITORING ORGANIZATION Naval Postgraduate School			
6c. ADDRESS (City, State, and ZIP Code) Monterey, California 93943-5100		7b. ADDRESS (City, State, and ZIP Code) Monterey, California 93943-5100			
8a NAME OF FUNDING/SPONSORING ORGANIZATION	8b. OFFICE SYMBOL (If applicable)	9. PROCUREMENT INSTRUMENT IDENTIFICATION NUMBER			
8c. ADDRESS (City, State, and ZIP Code)		10. SOURCE OF FUNDING NUMBERS			
		PROGRAM ELEMENT NO	PROJECT NO	TASK NO	WORK UNIT ACCESSION NO
11. TITLE (Include Security Classification) <b>A NUMERICAL SIMULATION OF THE MEI-YU FRONT AND THE ASSOCIATED LOW-LEVEL JET</b>					
12. PERSONAL AUTHOR(S) Lang C. Chou					
13a. TYPE OF REPORT Doctor of Philosophy	13b. TIME COVERED FROM _____ TO _____		14. DATE OF REPORT (Year, Month, Day) 1986, September	15. PAGE COUNT 161	
16. SUPPLEMENTARY NOTATION					
17. COSATI CODES		18. SUBJECT TERMS (Continue on reverse if necessary and identify by block number) Front Frontogenesis Mei-Yu Convection Asian Monsoon Low-Level Jet			
19. ABSTRACT (Continue on reverse if necessary and identify by block number) The Mei-Yu front is a quasi-stationary belt of heavy precipitation imbeded in the summer monsoon trough over East Asia. This work used a two dimensional frontogenesis model to study the Mei-Yu front, especially its associated low-level jet (LLJ) which often occurs during intense convection. Several numerical experiments were carried out to simulate the quasi-steady frontal structures in different environments. The results resemble many observed features, such as the stronger temperature and moisture gradients in the midlatitude fronts and the stronger horizontal shear and LLJ in the subtropical fronts. The LLJ is most conspicuous in the subtropical simulation when high humidity and surface fluxes are included. The results further suggest that the LLJ is developed through the Coriolis torque that is exerted by the low-level poleward branch of a "reversed Hadley cell" equatorward of					
20. DISTRIBUTION/AVAILABILITY OF ABSTRACT <input checked="" type="checkbox"/> UNCLASSIFIED/UNLIMITED <input type="checkbox"/> SAME AS RPT <input type="checkbox"/> DTIC USERS			21. ABSTRACT SECURITY CLASSIFICATION UNCLASSIFIED		
22a. NAME OF RESPONSIBLE INDIVIDUAL Robert J. Renard			22b. TELEPHONE (Include Area Code) (408) 646-2516	22c. OFFICE SYMBOL Code 63Rd	

UNCLASSIFIED

SECURITY CLASSIFICATION OF THIS PAGE (When Data Entered)

20. Abstract (Continued)

the front. This thermally direct cell is different from the normal cross-frontal secondary circulation. Its development depends on the occurrence of intense convection.

S N 0102-LF-014-6601

UNCLASSIFIED

SECURITY CLASSIFICATION OF THIS PAGE (When Data Entered)

Approved for public release, distribution unlimited.

A Numerical Simulation of the Mei-Yu Front  
and the Associated Low-Level Jet

by

Lang C. Chou  
B.S., Tunghai University, 1968  
M.S., University of Washington, 1977

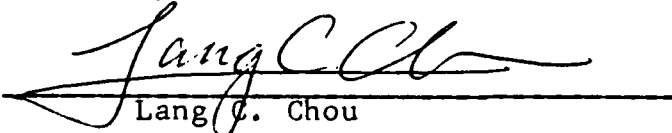
Submitted in partial fulfillment of the  
requirements for the degree of

DOCTOR OF PHILOSOPHY IN METEOROLOGY

from the

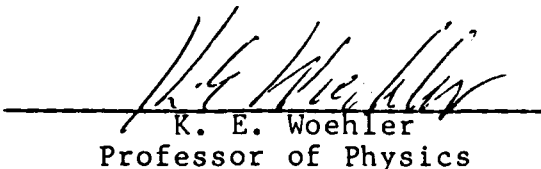
NAVAL POSTGRADUATE SCHOOL  
September 1986

Author:

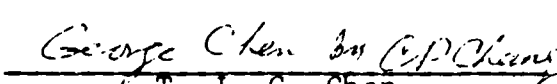
  
Lang C. Chou

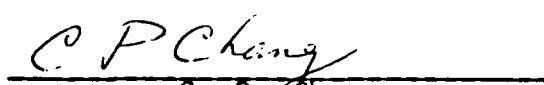
Approved by:

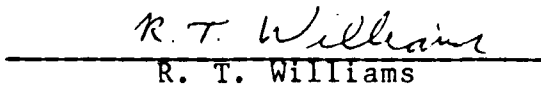
  
A. L. Schoenstadt  
Professor of Mathematics

  
K. E. Woehler  
Professor of Physics

  
R. L. Elsberry  
Professor of Meteorology

  
T.-J. G. Chen  
Professor of Meteorology  
National Taiwan University

  
C.-P. Chang  
Professor of Meteorology  
Dissertation Co-Supervisor

  
R. T. Williams  
Professor of Meteorology  
Dissertation Co-Supervisor

Approved by:   
R. J. Renard  
Chairman, Department of Meteorology

Approved by:   
D. A. Schrady, Academic Dean

Availability Codes	
Dist	Avail and/or Special
A-1	

QUALITY INSPECTED  
1

## ABSTRACT

The Mei-Yu front is a quasi-stationary belt of heavy precipitation imbedded in the summer monsoon trough over East Asia. This work used a two dimensional frontogenesis model to study the Mei-Yu front, especially its associated low-level jet (LLJ) which often occurs during intense convection. Several numerical experiments were carried out to simulate the quasi-steady frontal structures in different environments. The results resemble many observed features, such as the stronger temperature and moisture gradients in the midlatitude fronts and the stronger horizontal shear and LLJ in the subtropical fronts. The LLJ is most conspicuous in the subtropical simulation when high humidity and surface fluxes are included. The results further suggest that the LLJ is developed through the Coriolis torque that is exerted by the low-level poleward branch of a "reversed Hadley cell" equatorward of the front. This thermally direct cell is different from the normal cross-frontal secondary circulation. Its development depends on the occurrence of intense convection.

## TABLE OF CONTENTS

I.	INTRODUCTION -----	12
	A. OBSERVATIONAL STUDIES -----	12
	1. Mei-Yu -----	12
	2. Mei-Yu Front -----	14
	3. Low Level Jet (LLJ) -----	17
	4. Mesoscale Convective Systems (MCS's) -----	18
	B. THEORETICAL STUDIES -----	19
	1. Front -----	19
	2. Symmetric Instability -----	21
	3. Low Level Jet -----	24
	C. OBJECTIVES -----	25
II.	NUMERICAL MODEL -----	33
	A. BASIC EQUATIONS -----	34
	B. CONVECTIVE ADJUSTMENT PROCESSES AND LATENT HEATING -----	42
	C. BOUNDARY LAYER PARAMETERIZATION -----	47
	D. INITIAL CONDITIONS -----	49
III.	NUMERICAL EXPERIMENTS AND RESULTS -----	52
	A. EXPERIMENT CASES AND PARAMETERS -----	53
	B. MIDLATITUDE SIMULATIONS -----	56
	1. Typical Midlatitude Case (M60) -----	56
	2. Other Midlatitude Cases -----	59

C. SUBTROPICAL SIMULATIONS -----	67
1. Typical Subtropical Case (S90) -----	67
2. Other Subtropical Cases -----	75
D. SUMMARY OF THE RESULTS -----	80
IV. MECHANISM FOR THE LOW LEVEL JET (LLJ) -----	116
V. SUMMARY AND CONCLUSIONS -----	136
APPENDIX	
A. SPECIFICATION OF MODEL GRIDS -----	145
B. GRID ARRANGEMENTS -----	147
C. FINITE DIFFERENCE FORMULATION -----	148
LIST OF REFERENCES -----	151
INITIAL DISTRIBUTION LIST -----	158

## LIST OF FIGURES

1.1	Mean daily rainfall (y-axis, mm) for the period of 1951-1970 at Taichung, Taiwan, which is a typical station having a Mei-Yu rainfall maximum (Chen, 1977). -----	28
1.2	Mean onset date of the summer monsoon and the onset date of Mei-Yu season in East Asia (Tao and Chen, 1986). -----	29
1.3	Frequency of frontogenesis at $1^{\circ}$ longitude by $1^{\circ}$ latitude grid intervals during the Taiwan Mei-Yu period of May 15 to June 15, 1968-1977 (Chen and Chi, 1980). -----	30
1.4	Vertical cross-section of (a) east-west wind ( $u$ ; solid) and north-south wind ( $v$ ; dash) components in $m s^{-1}$ ; (b) total wind speed (solid) in $m s^{-1}$ and mixing ratio (dash) in $g kg^{-1}$ along $120^{\circ}E$ at 12 GMT 11 June 1975. J indices from left to right increase from south to north with a grid distance of 240 km. The Mei-Yu front at 850mb is near $J=7$ (Chen, 1978). -----	31
1.5	GMS-1 satellite IR picture at 00 GMT 28 May 1981. a,b and c indicate organized mesoscale convective systems. -----	32
3.1	Initial potential temperature (solid), $\theta(^{\circ}K)$ , and equivalent potential temperature (dash), $\theta_e(^{\circ}K)$ , soundings at the center of the model domain for midlatitude cases - M60 and M90 and subtropical cases - S60 and S90 (see text). -----	83
3.2	Cross-section of (a) mixing ratio (solid), $q(g kg^{-1})$ , and potential temperature (dash), $\theta(^{\circ}K)$ , (b) westerly (solid) and easterly (dash) zonal wind, $U (m s^{-1})$ for typical midlatitude case, M60, at day 0. -----	84
3.3	Cross-section of mixing ratio (solid), $q(g kg^{-1})$ , and potential temperature (dash), $\theta(^{\circ}K)$ , for typical midlatitude case M60, at (a) day 1.0, (b) day 2.0, (c) day 3.0 and (d) day 4.0. -----	85

3.4	As in Fig. 3.3, except for horizontal potential temperature gradient, $\partial\theta/\partial y$ ( $^{\circ}\text{K km}^{-1}$ ). Heavy dash lines at day 4, ( $-0.02 ^{\circ}\text{K km}^{-1}$ ) indicate frontal zone. -----	86
3.5	As in Fig. 3.3, except for vertical pressure velocity, $-\omega(10^{-4} \text{ cb s}^{-1})$ . -----	87
3.6	As in Fig. 3.3, except for zonal wind speed, $U(\text{m s}^{-1})$ . -----	88
3.7	As in Fig. 3.3, except for vorticity, $\zeta(10^{-4} \text{ s}^{-1})$ . Heavy dash lines indicate frontal zone. -----	89
3.8	Cross-section of mixing ratio (solid), $q(\text{g kg}^{-1})$ , and potential temperature (dash), $\theta(^{\circ}\text{K})$ , for different midlatitude cases at day 4, (a) M60, (b) M90, (c) M61 and (d) M91 (see text). -----	90
3.9	As in Fig. 3.8, except for horizontal potential temperature gradient, $\partial\theta/\partial y$ ( $^{\circ}\text{K km}^{-1}$ ). Heavy dash lines indicate frontal zone. -----	91
3.10	As in Fig. 3.8, except for vertical pressure velocity, $-\omega(10^{-4} \text{ cb s}^{-1})$ . -----	92
3.11	As in Fig. 3.8, except for zonal wind speed, $U(\text{m s}^{-1})$ . -----	93
3.12	As in Fig. 3.8, except for vorticity, $\zeta(10^{-4} \text{ s}^{-1})$ . -----	94
3.13	Precipitation rate for midlatitude cases in units of $\text{cm day}^{-1}$ , (a) M60, (b) M90, (c) M61 and M91. -	95
3.14	Cross-section of total heating rate for midlatitude cases in units of $\text{degree day}^{-1}$ , (a) M60, (b) M90, (c) M61 and M91. -----	96
3.15	Surface fluxes of momentum (dash; $-10^{-4} \text{ m cb s}^{-2}$ ), sensible heat (solid; $-10^{-4} ^{\circ}\text{K cb s}^{-1}$ ), and latent heat (dot; $-10^{-4} ^{\circ}\text{K cb s}^{-1}$ ). (a) M61 and (b) M91. -----	97
3.16	As in Fig. 3.2, except for typical subtropical case, S90. -----	98
3.17	As in Fig. 3.3, except for typical subtropical case, S90, (a) day 4 and (b) day 5. -----	99

3.18	Cross-section of 24-hour averaged mixing ratio (solid), $q(\text{g kg}^{-1})$ , and potential temperature (dash), $\theta(\text{°K})$ , for (a) day 2.0, (b) day 3.0, (c) day 4.0 and (d) day 5.0. -----	100
3.19	As in Fig. 3.18, except for horizontal potential temperature, $\partial\theta/\partial y(\text{°K km}^{-1})$ . Heavy dash line at day 5.0, $(-0.01 \text{°K km}^{-1})$ indicate frontal zone. -	101
3.20	As in Fig. 3.18, except for vertical pressure velocity, $-\omega(10^{-4} \text{ cb s}^{-1})$ . -----	102
3.21	Cross-section of vertical pressure velocity, $-\omega(10^{-4} \text{ cb s}^{-1})$ , at day 4.5 for case S90. -----	103
3.22	As in Fig. 3.18, except for zonal wind speed, $U(\text{m s}^{-1})$ . -----	104
3.23	As in Fig. 3.18, except for vorticity, $\zeta(10^{-4} \text{ s}^{-1})$ . -----	105
3.24	Cross-section of 24-hour averaged (a) mixing ratio (solid), $q(\text{g kg}^{-1})$ , and potential temperature (dash), $\theta(\text{°K})$ , (b) horizontal potential temperature gradient, $\partial\theta/\partial y(\text{°K km}^{-1})$ , (c) vertical pressure velocity, $-\omega(10^{-4} \text{ cb s}^{-1})$ and (d) zonal wind speed, $U(\text{m s}^{-1})$ at day 5.0 for the typical subtropical case, S90, integrated for 5 days from the 5-day averaged fields as initial conditions. -----	106
3.25	Cross-section of 24-hour averaged mixing ratio (solid), $q(\text{g kg}^{-1})$ , and potential temperature (dash), $\theta(\text{°K})$ , for different subtropical cases (a) S60, (b) S90, (c) S61 and (d) S91. -----	107
3.26	As in Fig. 3.25, except for horizontal potential temperature gradient, $\partial\theta/\partial y (\text{°K km}^{-1})$ . Heavy dash lines $(-0.01 \text{ °K km}^{-1})$ indicate frontal zone. -----	108
3.27	As in Fig. 3.25, except for vertical pressure velocity, $-\omega(10^{-4} \text{ cb s}^{-1})$ . -----	109
3.28	As in Fig. 3.25, except for zonal wind speed, $U(\text{m s}^{-1})$ . -----	110
3.29	As in Fig. 3.25, except for vorticity, $\zeta(10^{-4} \text{ s}^{-1})$ . -----	111

3.30	Precipitation rate for subtropical cases in units of $\text{cm day}^{-1}$ , (a) S60, (b) S90, (c) S61 and S91. -----	112
3.31	Cross-section of total heating rate for subtropical cases in units of degree $\text{day}^{-1}$ , (a) S60, (b) S90, (c) S61 and S91. -----	113
3.32	Surface fluxes of momentum (dash; $-10^{-4} \text{ m cb s}^{-2}$ ), sensible heat (solid; $-10^{-4} \text{ }^\circ\text{K cb s}^{-1}$ ), and latent heat (dot; $-10^{-4} \text{ }^\circ\text{K cb s}^{-1}$ ). (a) S61 and (b) S91. -----	114
3.33	Cross-section of 24-hour averaged zonal wind speed, $U(\text{m s}^{-1})$ , for different subtropical cases (a) S61, (b) S71, (c) S81 and (d) S91. -----	115
4.1	Schematic diagram to show the differences between (a) frontal secondary circulation, (b) upright convection and (c) slantwise convection. -----	127
4.2	Streamfunction, $\psi(\text{m cb s}^{-1})$ at day 4 for different midlatitude cases, (a) M60, (b) M90, (c) M61 and (d) M91. -----	128
4.3	24-hour averaged streamfunction, $\psi(\text{m cb s}^{-1})$ at day 5 for different subtropical cases, (a) S60, (b) S90, (c) S61 and (d) S91. -----	129
4.4	Cross-section of M-function (solid) in units of $\text{m s}^{-1}$ and equivalent potential temperature (dash), $\theta_e(\text{ }^\circ\text{K})$ for typical midlatitude case, M60, at (a) day 0.0, (b) day 1.0, (c) day 2.0, (d) day 3.0, (e) day 4.0 and (f) day 5.0. -----	130
4.5	Cross-section of 24-hour averaged M-function (solid) in units of $\text{m s}^{-1}$ and equivalent potential temperature (dash), $\theta_e(\text{ }^\circ\text{K})$ for typical subtropical case, S90, at (a) day 0.0, (b) day 1.0, (c) day 2.0, (d) day 3.0, (e) day 4.0 and (f) day 5.0. -	131
4.6	As in Fig. 4.2, except for M-function (solid) in units of $\text{m s}^{-1}$ and equivalent potential temperature (dash), $\theta_e(\text{ }^\circ\text{K})$ . -----	132
4.7	As in Fig. 4.3, except for M-function (solid) in units of $\text{m s}^{-1}$ and equivalent potential temperature (dash), $\theta_e(\text{ }^\circ\text{K})$ . -----	133
B.1	The model grid arrangement. -----	147

### Acknowledgments

I wish to express my appreciation to Professors C.-P. Chang and R. Terry Williams for their tireless guidance, assistance and encouragement throughout all phases of this work, to Professors George T.-J. Chen and Hock Lim for insightful discussions particularly on the observations of the Mei-Yu front and several related theories, and to Professor Russell L. Elsberry for reading the thesis and offering helpful comments and suggestions.

This work was supported in part by the National Science Foundation, Division of Atmospheric Sciences (Grant ATM 8315175) and Division of International Programs (Grant INT 8506450) and by the Naval Environmental Prediction Research Facility. The numerical computations were carried out at the W. R. Church Computer Center.

I wish to thank Ms. Kyong H. Lee for her expert processing of the manuscript. Finally, I want to say thank you to my wife, Betty, for her patience, understanding and support, and I dedicate this dissertation to her.

## I. INTRODUCTION

A review of recent observational studies of the main phenomena of this study, the Mei-Yu, and the associated disturbances will be presented first. There follows a review of the pertinent theoretical studies. A description of the objectives of this numerical study of the Mei-Yu front will then be given.

### A. OBSERVATIONAL STUDIES

#### 1. Mei-Yu

Over eastern Asia, the transition period from the northeast winter monsoon to the southwest summer monsoon possesses a distinctive climatological phenomenon which is important for regional weather forecasting. The seasonal rainfall reaches a maximum during this period (Fig. 1.1). The rainfall during this period is called "Mei-Yu" (plum rain) in China and "Baiu" in Japan. During this period, the rainfall may be continuous or intermittent for several days to a few weeks and is characterized by frequent rain-showers and thunderstorms, with rainfall rates of up to a few hundred millimeters per day (e.g., Chen, 1983; Ninomiya, 1980). The Mei-Yu season first appears in southern China in May, and influences the weather over southern China and Taiwan from mid-May to mid-June (Chen and Chi, 1980). It

then migrates over the Yangtze Valley and Japan from mid-June to mid-July.

Synoptically, the Mei-Yu rainfall is associated with the repeated occurrence of a front that develops in the midlatitudes and slowly moves southeastward to a quasi-stationary position extending from southern Japan to southern China. Satellite pictures reveal a nearly continuous cloud band accompanying this front, which is often called a Mei-Yu front or a Baiu front. The frontal position coincides with the early summer monsoon trough in eastern Asia and its existence may be viewed as a manifestation of the trough. The beginning of the rainy season also signifies the onset of the northern summer monsoon in this part of the world. The Mei-Yu often undergoes sequential jumps between May and July (Fig. 1.2; Tao and Chen, 1987) depending upon the strength and the position of the North Pacific Ocean subtropical high (Tao and Ding, 1981). As the Mei-Yu onset occurs in the Yangtze River region in June, the Indian monsoon is also being established and the westerly jet stream begins to retreat to the north of the Tibetan Plateau. At the same time, the subtropical high in the western Pacific area moves northward to 20-25°N. The Mei-Yu season lasts through mid-July, when the subtropical high moves northward to 30°N. At that time, the rain belt is to the north of the Yellow River, which signifies the beginning of heavy rainfall period in northern

China and the ending of the Mei-Yu in subtropical China (Tao and Chen, 1987).

## 2. Mei-Yu Front

The climatology of the Mei-Yu front over southern China and the adjacent areas was examined by Chen and Chi (1980) for the periods of 15 May-15 June, 1968-1977. They found that the Mei-Yu frontogenesis takes place in the subtropical part of southern China to the south of  $\sim 35^{\circ}\text{N}$ . All the Mei-Yu fronts were formed in the area of  $20^{\circ}\text{-}35^{\circ}\text{N}$  and  $100^{\circ}\text{-}130^{\circ}\text{E}$  (Fig. 1.3). The lifetime of individual cases of Mei-Yu fronts ranges from 3 days to 22 days with an average of 8 days. The kinematic background for the frontogenesis is the deformation field between the subtropical high over the Pacific and the migratory high over central China. They suggested that the sea-surface temperature contrast in the nearby South and East China Seas may also be a favorable factor for the frontogenesis.

In contrast to the polar front, the temperature contrast across the Mei-Yu front is typically small, but there is always a marked moisture gradient near the frontal zone (Akiyama, 1973a; Chen and Tsay, 1978; Matsumoto et al., 1970, 1971; Tao, 1980). An analysis of the kinematic structure of the Mei-Yu frontal system over Southeast Asia was carried out by Chen (1978). The Mei-Yu frontal system possesses a remarkable shear line which roughly coincides with a trough at 850 and 700 mb, although the associated

geopotential gradient is rather weak in the immediate vicinity of trough. The shear line approximately coincides with the maximum north-south gradients of mixing ratio and equivalent potential temperature. To the south of the shear line, a low level jet (LLJ) that is characterized by maximum mixing ratio and high equivalent potential temperature is found near 700 mb (Fig. 1.4). Strong cyclonic vorticity, horizontal convergence and upward motion are observed along and to the south of the shear line. The cloud band approximately coincides with the area of maximum cyclonic vorticity, horizontal convergence and upward motion. Intense convective clouds in the southern portion of the cloud band tend to be associated with the maximum values of these kinematic parameters as well with relative humidities greater than 80% in the lower-middle troposphere. Clear skies over the East China Sea and its vicinity are accompanied by downward motion of dry air (relative humidity less than 30% at 850 mb, less than 10% at 700 and 500 mb).

Chen and Chang (1980) studied the structure and calculated a vorticity budget for a Mei-Yu system during the period 10-15 June 1975. During the mature and decaying stages of the monsoon trough, the structure of the eastern section (southern Japan) and the central section (East China Sea) is different from that of the western section (southeastern China). In the eastern and central section, the structure resembles a typical midlatitude baroclinic

front with a strong vertical tilt toward an upper-level cold core low and a strong horizontal temperature gradient. On the other hand, the western section resembles a tropical disturbance with an equivalent barotropic, warm core structure, a relatively weak horizontal temperature gradient and a rather strong horizontal wind shear in the lower troposphere. In the mature stage, the upward motion reaches maximum values at 500 mb. It is located over the 850 mb monsoon trough in the western (W) section,  $4^{\circ}$  latitude south of the trough in the central (C) and  $3^{\circ}$  latitude southeast of the trough in the eastern (E) section. On the north side of the trough, downward motion prevails with a maximum at 400 mb in sections C and E, and at 700 mb in section W. This well-organized vertical velocity couplet is indicative of a well-developed secondary circulation normal to the trough. In the decaying stage, the circulation becomes substantially less vigorous in sections W and C, but it maintains intensity in section E. Tsay and Chen (1980) analyzed the processes which force the vertical motion in sections W, C and E. They found the eastern portion partially maintains the characteristics of a midlatitude system, while the western portion behaves similar to a tropical system.

The Mei-Yu front can be several thousand kilometers long, and therefore it is a large-scale monsoonal phenomenon. However, the cross-front scale is considerably

smaller, which is within the mesoscale range. Among the many mesoscale features that are observed near the Mei-Yu frontal zone, the most important are the organized mesoscale convective systems embedded within the broad Mei-Yu cloud band, which lies on the warm side of the front (Fig. 1.5). These convective systems tend to move along the front from west to east and produce locally heavy rainfall rates of  $> 100 \text{ mm day}^{-1}$  (Akiyama, 1974, 1978; Chen, 1977; Ninomiya and Akiyama, 1971, 1972, 1973, 1974).

### 3. Low Level Jet (LLJ)

To the south of the Mei-Yu (or Baiu) front, there is often a strong ageostrophic low level jet (LLJ) which is usually observed between 1.5 and 3 km (850-700 mb) and is strongly correlated to the heavy rainfall (Akiyama, 1973b; Chen, 1977, 1986; Matsumoto, 1972; Matsumoto, et al., 1971; Ninomiya and Akiyama, 1974; Tao and Chen, 1987). Akiyama (1973a) observed that the heavy rainfalls in the Japan Baiu season occur most frequently to the north of the low level jet stream and seldom occur in areas more than 200 km south of the jet axis. Matsumoto (1973) found that the peak of heavy rainfall precedes by 6 h the peak of the low level jet speed. He also found that the peak of heavy rainfall is in phase with the maximum acceleration of the LLJ.

In the Great Plains and Midwest areas of the United States, the low level jets are a climatological feature with the maximum frequency during the spring and summer months

(Bonner, 1968). The low level jets in this area are basically a boundary layer phenomenon that are characterized by a diurnal oscillation. The jet reaches maximum intensity by early morning, and is associated with a nocturnal temperature inversion (e.g., Blackadar, 1957; Bonner, 1968; Holton, 1967; Lettau, 1967; Wexler, 1961). Different theories (discussed later in section B) have been proposed to explain the generation of the low level jet and the seasonal, temporal and geographic variations. In the British Isles, a low level jet in conjunction with midlatitude cyclones was studied by Browning and Harrold (1970) using Doppler radar observations. Browning and Pardoe (1973) found that for six cases of ana-cold fronts occurring in the colder months in British Isles, the low level jet had a maximum velocity in the layer 900 to 850 mb of 25 to 30  $m s^{-1}$  and occurred during night or day.

#### 4. Mesoscale convective systems (MCS's)

Rainfall characteristics over Taiwan and vicinity were studied by Chen (1977) and Chen and Tsay (1978) using dense hourly rainfall reports, radar echoes and satellite pictures. The low level southwesterlies, especially the LLJ, tends to create potential instability to the warm side of Mei-Yu front. Continued large-scale ascent then leads to the release of potential instability through organized mesoscale convective systems. The mesoscale convective systems embedded within the broad Mei-Yu cloud band can be

of several different sizes (meso - $\alpha$ , - $\beta$ , or - $\gamma$ ). A case study by Chen and Tsay (1978) revealed the existence of these mesosystems in Taiwan with wavelengths of 60, 85 and 170 km and the corresponding periods of 2.6, 3.5 and 7.1 h. A spectrum analysis (Tao, 1980) of radar echoes in the rainbands along the Mei-Yu front over the Chinese mainland also showed the existence of organized mesoscale convective systems with wavelengths of 150, 84 and 50 km. Akiyama (1978) found that the echoes within the rainband in the Baiu season in Japan are organized into mesoscale clusters with spatial intervals on the order of 100-150 km.

Simulations of these mesoscale convective systems require a three-dimensional model. In our two-dimensional simulations, we will not study these phenomena.

## B. THEORETICAL STUDIES

### 1. Front

Quasi-geostrophic frontal theories (Stone, 1966; Williams, 1968; Williams and Plotkin, 1968) showed that large-scale deformation fields can lead to surface frontogenesis and result in strong horizontal temperature gradients that are characteristic of fronts. However, the structure of the front and the associated secondary circulation do not tilt with height. It also lacks cyclonic wind shear at the front and has several other unrealistic features, including the infinite time required for the front

to form. Later studies using primitive equations (Williams, 1972) and the semi-geostrophic equations (Hoskins and Bretherton, 1972) removed these unrealistic features by including the ageostrophic advections of temperature and momentum. In particular, Hoskins and Bretherton (1972) used the set of semi-geostrophic equations to show that the nonlinear effects of the ageostrophic advections can be represented by the quasi-geostrophic solutions, if these solutions are written in the geostrophic coordinates and then transformed to the physical space. Later, the semi-geostrophic theory was expanded to three dimensions by Hoskins (1975) and Hoskins and Draghici (1977).

Frictional and diabatic effects also have been studied by a number of investigators. Williams (1974) found that vertical mixing can determine the slope of a front, and, together with horizontal mixing, can determine the cross-width of the frontal zone. Keyser and Anthes (1982) showed that the proper simulation of the concentrated upward motion in the surface frontal zone depends on the planetary boundary layer parameterization. Williams et al. (1981), Ross and Orlanski (1978), and Hsie and Anthes (1984) found that latent heat release intensifies both the upper level westerlies and the low level easterlies poleward of the surface front, and the ageostrophic secondary circulation across the front.

## 2. Symmetric Instability

Within extratropical cyclones, banded structures in clouds and precipitation have been observed both in conditionally stable and unstable atmospheres (Hobbs, 1978). Bennetts and Hoskins (1979) suggested that these bands are a result of conditional symmetric instability. Emanuel (1979) demonstrated that circulations resulting from this instability are fundamentally mesoscale in character. Recent observations indicate that conditional symmetric instability is responsible for some precipitation bands within extratropical cyclones (Bennetts and Sharp, 1982; Moore, 1985; Parsons and Hobbs, 1983; Sanders and Bosart, 1985).

Bennetts and Hoskins (1979) and Emanuel (1982) assessed the degree of conditional symmetric instability based on infinitesimal displacements in saturated atmospheres. Emanuel (1983a,b) considered parcel instability which leads to a measure of the stability of the moist baroclinic atmosphere to finite slantwise reversible displacements of a two-dimensional air parcel or air "tube". Dynamically, inertial, symmetric and convective instabilities are very closely related. Each of these instabilities may be thought of as resulting from an imbalance of body forces acting on a fluid parcel. In the case of convective instability, the gravitational force acts vertically. In the case of inertial instability, the

centrifugal force acts horizontally. Symmetric instability simply represents motion resulting from a combination of these forces, and thus the motion is "slantwise." Following Emanuel (1983a,b), it can be shown that slantwise instability requires the slopes of the pseudo angular momentum ( $M$ ) surfaces to be smaller than those of the equivalent potential temperature ( $\theta_e$ ) surfaces. This is equivalent to stating that  $\theta_e$  decreases along the constant  $M$  surfaces upward or that  $M$  decreases in the cross-front direction toward warm air along a  $\theta_e$ -surface. From the definition of  $M$ , the latter implies that the absolute vorticity is negative along  $\theta_e$ -surfaces.

A case study by Emanuel (1983b) of a strongly baroclinic flow with observed linear bands of clouds and precipitation reveals that the atmosphere is initially conditionally unstable to upright convection and tends to become neutral with respect to slantwise displacements. Such an atmosphere possesses moist adiabatic lapse rates along  $M$  surfaces, even though it may be substantially stable to vertical displacements. In this case, conditionally unstable baroclinic flow undergoes a form of slantwise moist adiabatic adjustment that renders the atmosphere neutral to slantwise reversible displacements. The adjustment uses up the total slantwise convective available potential energy (SCAPE) rather than just the convective (gravitational part of) available potential energy (CAPE) for upright

convection. After such an adjustment, the SCAPE of the atmosphere is very close to zero while the CAPE actually becomes negative.

Emanuel (1985) carried out a diagnostic study using a semi-geostrophic model with small potential vorticity (i.e., small symmetric stability) in the region of upward motion and not so small potential vorticity in the region of downward motion. He demonstrated that frontal forcing results in a strong, concentrated, sloping updraft that is located ahead of the region of maximum geostrophic frontogenetical forcing. The distance between the "front" and the updraft will, in the atmosphere, have a typical value on the order of 50-200 km. This was observed by Sanders and Bosart (1985), who found that slantwise convection can persist even after a condition of near-neutrality has been achieved under frontogenetical forcing. It has also been shown by Thorpe and Emanuel (1985) that in an atmosphere which has small stability to slantwise convection, frontogenesis proceeds at a greatly increased rate (due to latent heat release) and the horizontal scale of the ascent in the warm air is considerably reduced. Cross-frontal circulations produced by geostrophic forcing are similar in structure to slantwise convection, despite the (small) stability to the latter.

### 3. Low Level Jet (LLJ)

In the vicinity of Japan, the Baiu front is accompanied by an ageostrophic LLJ near 700 mb, which is oriented along the heavy rainfall zone. The ageostrophic LLJ is suggested to be a result of the downward transport of horizontal momentum caused by cumulus convection (Akiyama, 1973a; Matsumoto, 1972; Matsumoto and Ninomiya, 1969; Matsumoto et al., 1971; Ninomiya, 1971; Ninomiya and Akiyama, 1974). In China, several different relationships between the low level jet and heavy rains have been observed in the Mei-Yu season. In one of these, a LLJ is coupled and parallel to the upper tropospheric jet. The formation and strengthening of the LLJ is often associated with the heavy rainfall. Chen (1982) suggests that coupling of upper and lower level jets can be explained by an unstable inertia-gravity wave that arises from a thermal wind adjustment process that corrects an imbalance due to the advection in the entrance region of the upper level jet. This coupling is in contrast to that studied by Uccellini and Johnson (1979) in the Great Plains of the United States, where the LLJ tends to be perpendicular to and in the exit region of the upper level jet.

Several theories have also been proposed to explain the formation and diurnal oscillation of the LLJ in the Great Plains region of the United States. Blackadar (1957) suggested that oscillation in the boundary-layer mixing

processes is responsible for the diurnal variation of the LLJ intensity which reaches maximum values by the early morning. The temporal and geographic preference of the LLJ have been further explained by diurnal radiation fluxes over sloped terrain (Holton, 1967; Hsueh, 1970; Lettau, 1967), and topographical characteristics (Paegle and Rasch, 1973; Paegle, 1978). Observations also showed that low level jets may also develop in response to synoptic or subsynoptic processes, particularly through a response to leeside cyclogenesis that is common to the Great Plains (Djuric and Damiani, 1980; Djuric and Ludwig, 1983; Naistat and Young, 1973; Newton, 1956; 1967; Reiter, 1969; Uccellini, 1980). Numerical simulations and a case study by Uccellini and Johnson (1979) suggested that the development of the LLJ is coupled to the upper tropospheric jet streak by a mass adjustment process within the exit region of the streak.

#### C. OBJECTIVE OF THIS STUDY

The objective of this study is to use a two-dimensional frontogenesis model similar to that of Williams et al. (1981) to study the quasi-steady state structure of the Mei-Yu front and the LLJ. The model contains a convective-adjustment type cumulus heating parameterization and a bulk aerodynamics formula for the boundary layer. To study the possibility of cumulus momentum transport or the diurnal oscillation processes, additional parameterizations would be

necessary. Since considerable uncertainties exist in both the cumulus momentum transport and the diurnal radiation parameterizations, it is desirable to carry out a modeling study excluding these processes to see if the LLJ may be developed. One particular motivation for doing this is the tropical nature of the Mei-Yu front. The intense convection, which is correlated with the occurrence of strong low level vorticity, points to a different possibility. The large latent heat release provides an energy source which may, in certain situations, be converted to the kinetic energy of the LLJ. This possibility is worth investigation especially in light of the recent symmetric instability studies, which show that slantwise convection may occur in a frontal region even if the symmetric instability condition is neutral or slightly stable.

Therefore, the following topics are pursued in this study:

- 1) Study of the structure and dynamics of a steady front, which is investigated by varying the vertical stability, moisture content, Coriolis parameter and boundary-layer fluxes in the model; and
- 2) Study of the relationship between the occurrence of the LLJ and the convective activity in a Mei-Yu front. In particular, the possible role of a secondary circulation equatorward of the front caused by convection will be explored.

In Chapter II, the basic formulation of the model is presented. In Chapter III, the results of the numerical experiments are described, but the main interpretation of the results with respect to the dynamics of the LLJ is discussed in Chapter IV. Chapter V gives the summary and conclusions.

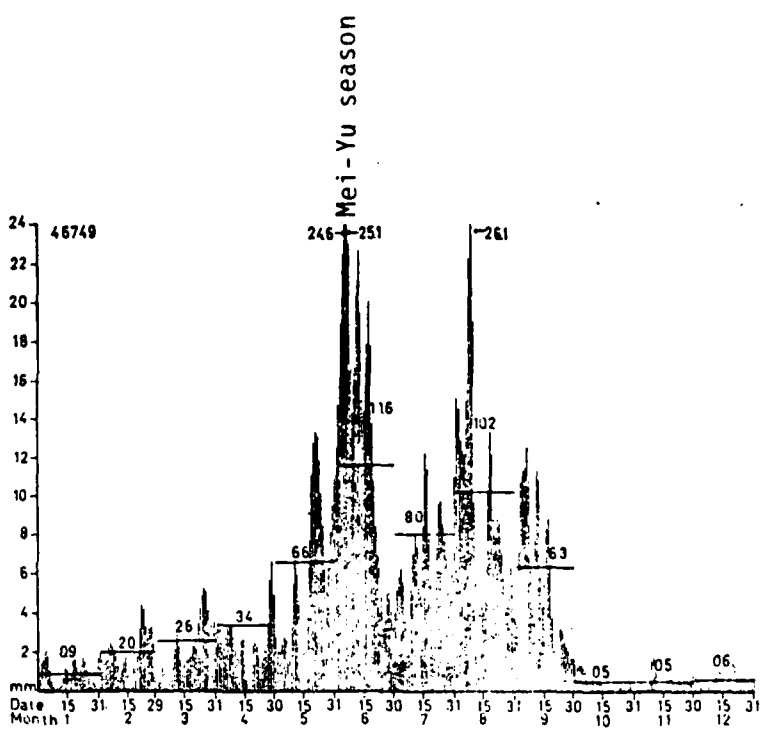


Fig. 1.1 Mean daily rainfall (y-axis, mm) for the period of 1951-1970 at Taichung, Taiwan, which is a typical station having a Mei-Yu rainfall maximum (Chen, 1977).

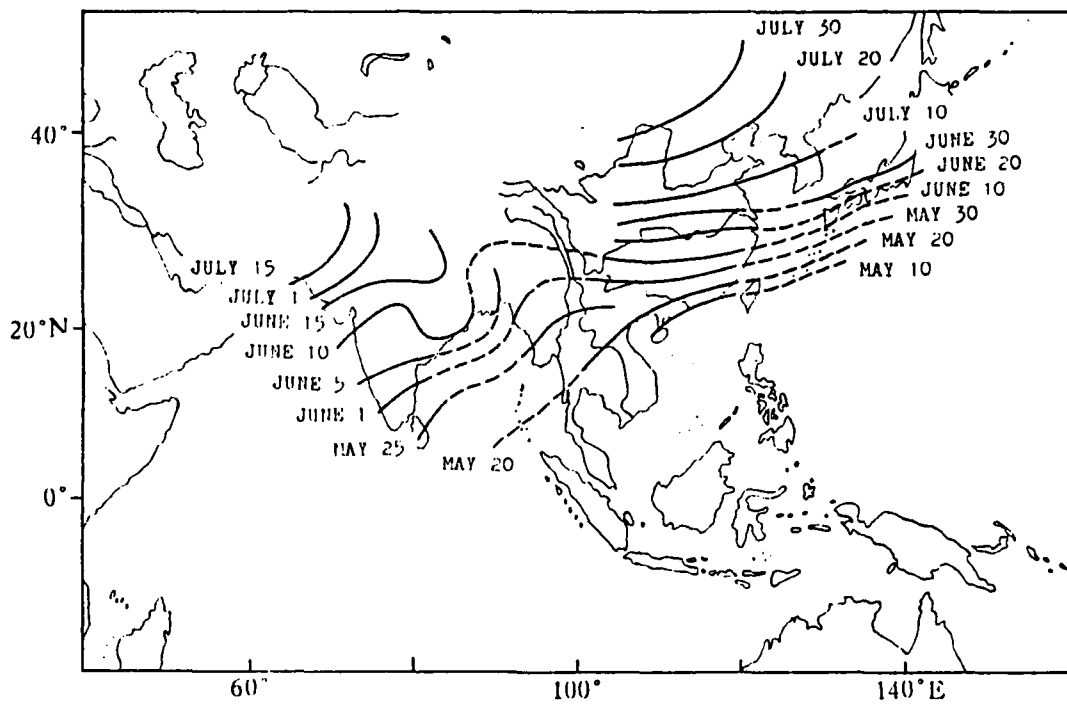


Fig. 1.2 Mean onset date of the summer monsoon and the onset date of Mei-Yu season in East Asia (Tao and Chen, 1986).

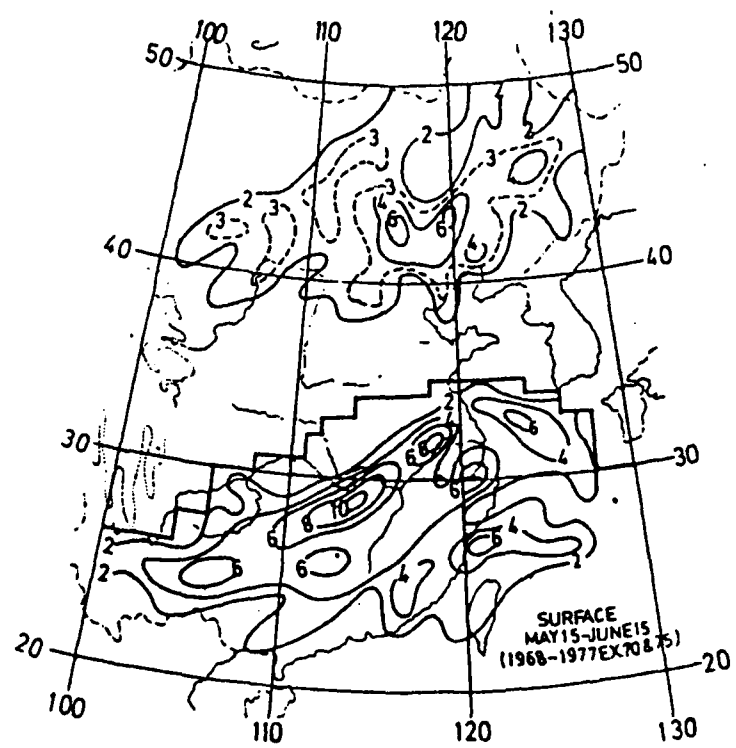


Fig. 1.3

Frequency of frontogenesis at  $1^{\circ}$  longitude by  $1^{\circ}$  latitude grid intervals during the Taiwan Mei-Yu period of May 15 to June 15, 1968-1977 (Chen and Chi, 1980).

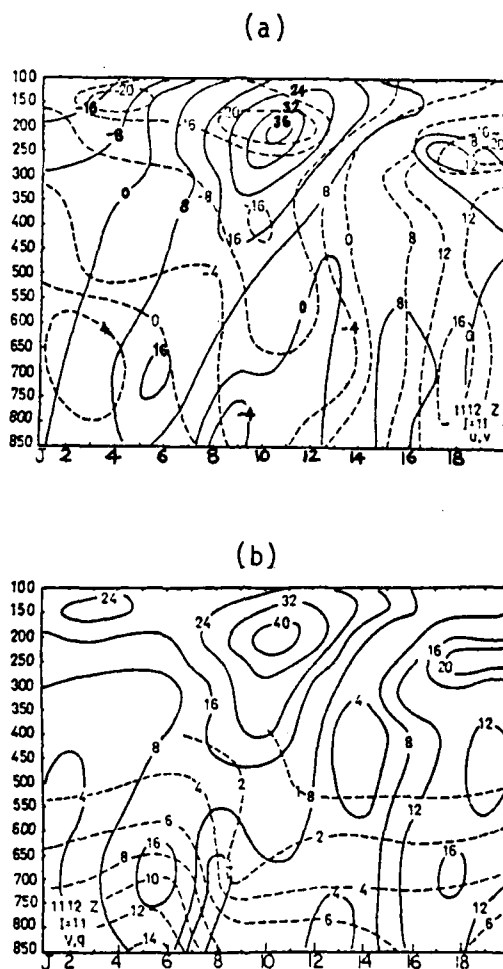


Fig. 1.4 Vertical cross section of (a) east-west wind ( $u$ ; solid) and north-south wind ( $v$ ; dash) components in  $m s^{-1}$ ; (b) total wind speed (solid) in  $m s^{-1}$  and mixing ratio (dash) in  $g kg^{-1}$  along  $120^{\circ}E$  at 1200 GMT 11 June 1975.  $J$  indices from left to right increase from south to north with a grid distance of 240 km. The Mei-Yu front at 850mb is near  $J=7$  (Chen, 1978).



Fig. 1.5 GMS-1 satellite IR picture at 0000 GMT 28 May 1981. a, b, and c indicate organized mesoscale convective system.

## II. NUMERICAL MODEL

This study uses a modified version of the model developed by Williams (1974) and Williams et al. (1981). The frontogenesis in the model is forced by a nondivergent basic wind field that contains stretching deformation and includes an Ekman layer structure. The model employs vertical and horizontal diffusions of potential temperature, moisture and velocity. The diffusion coefficients vary only with elevation. Pressure coordinates are used in the vertical and a tropopause is simulated. This should lead to a more accurate simulation of the upper regions where latent heating will be important. The time-dependent quantities in the model are functions of  $y$  (cross-front) and  $p$  and the model is integrated until a quasi-steady state is achieved. A planetary boundary layer is added with aerodynamic bulk formulae for the surface fluxes. A moist convective adjustment process is included to represent cumulus convection. A staggered grid is used in the horizontal because it gives a better treatment of the solutions that involve heating.

In Section A, the basic equations in pressure coordinates are developed including the appropriate moisture terms. The convective adjustment and latent heating are discussed in Section B. In Section C, the boundary layer treatment is described. The initial conditions and

tropopause simulation are in Section D. The details of the specification of model grids, grid arrangements and finite difference scheme are in Appendix A, B and C respectively.

#### A. BASIC EQUATIONS

The hydrostatic primitive equations in pressure coordinates may be written

$$\frac{\partial V}{\partial t} + \nabla \cdot (V V) + \frac{\partial}{\partial p} (\omega V) + \nabla \phi + \hat{f} k \times V = A_m \nabla^2 V + \frac{\partial}{\partial p} [ (K(p) \frac{\partial V}{\partial p})] , \quad (2.1.1)$$

$$\frac{\partial \theta}{\partial t} + \nabla \cdot (\theta V) + \frac{\partial}{\partial p} (\theta \omega) = A_\theta \nabla^2 \theta + \frac{\partial}{\partial p} [K(p) \frac{\partial \theta}{\partial p}] + \Omega_A + \Omega_M + H_C , \quad (2.1.2)$$

$$\frac{\partial q}{\partial t} + \nabla \cdot (q V) + \frac{\partial}{\partial p} (\omega q) = A_q \nabla^2 q + \frac{\partial}{\partial p} [K(p) \frac{\partial \theta}{\partial p}] + M_A - M_C , \quad (2.1.3)$$

$$\nabla \cdot V + \partial \omega / \partial p = 0 , \quad (2.1.4)$$

$$\partial \phi / \partial p = -r(p) \theta , \quad (2.1.5)$$

where:

$V$  = horizontal component of the velocity,

$\omega$  =  $dp/dt$ ,

$p$  = pressure,

$\phi$  =  $gZ$  = geopotential,

$\theta$  =  $T(p_0/p)^\kappa$  = potential temperature,

$T$  = temperature,

$R$  = gas constant,

$C_p$  = specific heat at a constant pressure,

$\kappa = R/C_p$ ,

$f = 2\Omega \sin \phi$  = Coriolis parameter,

$\Omega$  = rotation rate of earth,

$\phi$  = latitude,

$q$  = specific humidity,

$A_m$  = horizontal diffusion coefficient of momentum,

$A_\theta$  = horizontal diffusion coefficient of heat,

$A_q$  = horizontal diffusion coefficient of humidity,

$K(p)$  = vertical diffusion coefficient,

$Q_A$  = heating due to dry convective adjustment,

$Q_M$  = heating due to moist convective adjustment,

$H_C$  = large scale latent heating,

$M_A$  = specific humidity change due to moist convective adjustment,

$M_C$  = specific humidity change due to large-scale condensation,

$$r(p) = R p^{-1} \left(\frac{p}{p_0}\right)^K = C_p \frac{\partial}{\partial p} \left(\frac{p}{p_0}\right)^K.$$

The upper and lower boundary conditions are given by

$$\begin{aligned}\omega(x, y, p_t, t) &= \omega(x, y, p_0, t) = 0, \\ v(x, y, p_0, t) &= 0, \\ \frac{\partial v}{\partial p}(x, y, p_t, t) &= 0, \\ \frac{\partial \theta}{\partial p}(x, y, p_t, t) &= \frac{\partial \theta}{\partial p}(x, y, p_0, t) = 0.\end{aligned}\tag{2.1.6}$$

Here  $p_t$  and  $p_0$  represent the pressure at the top and bottom of the atmosphere, respectively, and these quantities are approximated as constants. The conditions (2.1.6) include the kinematic boundary condition at the top and bottom of the atmosphere, the zero slip condition at the surface, the zero stress condition at the top of the atmosphere, and the zero heat flux conditions at the top and bottom of the atmosphere, respectively.

The approximate steady-state solutions to (2.1.1)-(2.1.5) that satisfy the boundary conditions (2.1.6) are as follows:

$$\begin{aligned}\tilde{u} &= \Omega[x(1 - e^{-\xi} \cos \xi) + ye^{-\xi} \sin \xi], \\ \tilde{v} &= -\Omega[y(1 - e^{-\xi} \cos \xi) + xe^{-\xi} \sin \xi], \\ \omega &= 0, \\ \phi &= \Phi \equiv -D^2(x^2 + y^2)/2 - fDxy + F(p), \\ \theta &= G(p), \\ q &= H(p),\end{aligned}\tag{2.1.7}$$

where  $\xi = [f/2K(p_0)]^{1/2}(p_0 - p)$ . The deformation  $D$ , and the Coriolis parameter  $f$  are constant, and the functions  $F(p)$ ,  $G(p)$  and  $H(p)$  are arbitrary except that  $F$  and  $G$  must satisfy the hydrostatic equation (2.1.5). These solutions are only approximate within the Ekman layer because some small advection terms have been neglected.

The dependent variables are subdivided as follows:

$$\begin{aligned} U &= \tilde{u}(x, y, p) + u(y, P, t), \\ V &= \tilde{v}(x, y, p) + v(y, P, t), \\ \omega &= \omega(y, p, t), \quad \theta = \theta(y, p, t), \\ \phi &= \Phi(x, y) + \pi(y, p, t), \quad q = q(y, p, t), \end{aligned} \quad (2.1.8)$$

where all of the departures from the steady-state solutions are assumed to be independent of  $x$ . If we substitute the relations (2.1.8) into (2.1.1) - (2.1.5) and use  $\frac{\partial \tilde{u}}{\partial x} = -\frac{\partial \tilde{v}}{\partial y} = D(1 - e^{-\xi} \cos \xi)$ ,  $\frac{\partial \tilde{u}}{\partial y} = \frac{\partial \tilde{v}}{\partial x} = De^{-\xi} \sin \xi$ ,  $u, v$  satisfy the steady-state equations. The equations of the departure field from the steady-state solution become

$$\begin{aligned} \frac{\partial u}{\partial t} + \frac{\partial}{\partial y} (uv) + \frac{\partial}{\partial p} (\omega\omega) + u \frac{\partial \tilde{u}}{\partial x} + \tilde{v} \frac{\partial u}{\partial y} + v \frac{\partial \tilde{u}}{\partial y} + \omega \frac{\partial \tilde{u}}{\partial p} \\ = fv + A_m \frac{\partial^2 u}{\partial y^2} + \frac{\partial}{\partial p} (K \frac{\partial u}{\partial p}), \end{aligned} \quad (2.1.9)$$

$$\begin{aligned} \frac{\partial v}{\partial t} + \frac{\partial}{\partial y} (vv) + \frac{\partial}{\partial p} (\omega v) + \frac{\partial}{\partial y} (\tilde{v}v) + u \frac{\partial \tilde{v}}{\partial x} + \omega \frac{\partial \tilde{v}}{\partial p} \\ = -fu - \frac{\partial \pi}{\partial y} + A_m \frac{\partial^2 v}{\partial y^2} + \frac{\partial}{\partial p} (K \frac{\partial v}{\partial p}) \end{aligned} \quad (2.1.10)$$

$$\begin{aligned} \frac{\partial \theta}{\partial t} + \frac{\partial}{\partial y} (v\theta) + \frac{\partial}{\partial p} (\omega \theta) + \tilde{v} \frac{\partial \theta}{\partial y} = A_\theta \frac{\partial^2 \theta}{\partial y^2} + \frac{\partial}{\partial p} (K \frac{\partial \theta}{\partial p}) \\ + \Omega_A + \Omega_M + H_C, \end{aligned} \quad (2.1.11)$$

$$\begin{aligned} \frac{\partial q}{\partial t} + \frac{\partial}{\partial y} (vq) + \frac{\partial}{\partial p} (\omega q) + \tilde{v} \frac{\partial q}{\partial y} = A_q \frac{\partial^2 q}{\partial y^2} + \frac{\partial}{\partial p} (K \frac{\partial q}{\partial p}) \\ + M_A - M_C, \end{aligned} \quad (2.1.12)$$

$$\frac{\partial v}{\partial y} + \frac{\partial \omega}{\partial p} = 0, \quad (2.1.13)$$

$$\frac{\partial \pi}{\partial p} = -r(p)\theta \quad (2.1.14)$$

Using the relationship of (2.1.7), the (2.1.9) becomes

$$\begin{aligned} \frac{\partial u}{\partial t} + \frac{\partial}{\partial y} (uv) + \frac{\partial}{\partial p} (\omega u) + \Omega(1 - e^{-\xi} \cos \xi)u \\ - \Omega y(1 - e^{-\xi} \cos \xi) - xe^{-\xi} \sin \xi \frac{\partial u}{\partial y} + \Omega(e^{-\xi} \sin \xi)v \quad (2.1.15) \\ + \omega \Omega \frac{\partial}{\partial p} [x(1 - e^{-\xi} \cos \xi) + ye^{-\xi} \sin \xi] \\ = fv + A_m \frac{\partial^2 u}{\partial y^2} + \frac{\partial}{\partial p} (K \frac{\partial u}{\partial p}). \end{aligned}$$

It is to be noticed that the assumption that  $u$  is independent of  $x$  for all time is violated in (2.1.15) in the two terms where  $x$  appears. This indicates that the other quantities which were assumed independent of  $x$  are actually  $x$ -dependent, which would bring other terms into the equations. In this study, these added terms are neglected and (2.1.15) and the other equations are applied at  $x=0$ . If the initial  $u$ ,  $v$ ,  $\omega$ ,  $\theta$  and  $q$  fields are independent of  $x$ , the error from this approximation will grow slowly and it will be confined to the boundary layer since the  $x$ -dependent terms in (2.1.15) are zero outside the boundary layer. Since frontogenesis occurs very rapidly, it is expected that the development of  $x$ -variations in the dependent variables would only have a small effect on the resulting quasi-steady front. In any case, these effects could not be observed in the atmosphere, because atmospheric fronts always have some variation in the basic fields along the front which would be much more important.

When (2.1.15) is evaluated at  $x = 0$ , it becomes

$$\begin{aligned} \frac{\partial u}{\partial t} + \frac{\partial}{\partial y} (uv) + \frac{\partial}{\partial p} (\omega u) + \eta(1 - e^{-\xi} \cos \xi)u + \Gamma \frac{\partial u}{\partial y} \\ + \eta(e^{-\xi} \sin \xi)v - \omega V \eta \frac{\partial}{\partial p} (e^{-\xi} \sin \xi) = fv + A_m \frac{\partial^2 u}{\partial y^2} + \frac{\partial}{\partial p} (K \frac{\partial u}{\partial p}) \end{aligned}$$

(2.1.16)

where  $v_0 = -\bar{v}y$  and  $\Gamma = v_0(1 - e^{-\xi} \cos \xi)$ . To remove the vertical mean in (2.1.10), the vertical average is defined as

$$\langle \cdot \rangle = \frac{1}{p_0 - p_t} \int_{p_t}^{p_0} \cdot dp.$$

By vertically averaging (2.1.13) and using the boundary conditions (2.1.6), we obtain

$$\frac{\partial}{\partial y} \langle v \rangle = 0.$$

This equation states that the total disturbance  $y$  mass flux is independent of  $y$ . It can be expected that at a large distance from the frontal zone the disturbance mass flux will vanish. Thus, we get

$$\langle v \rangle = 0. \quad (2.1.17)$$

If we take the vertical average of (2.1.10) and use (2.1.6) and (2.1.7), we obtain

$$\begin{aligned} \frac{\partial}{\partial y} \langle vv \rangle + \frac{\partial}{\partial y} \langle \tilde{v}v \rangle + \langle u \frac{\partial \tilde{v}}{\partial x} \rangle + \langle \omega \frac{\partial \tilde{v}}{\partial p} \rangle \\ = - \frac{\partial \langle \pi \rangle}{\partial y} - f \langle u \rangle + \left[ \frac{K}{p_0} \frac{\partial v}{\partial p} \right]_{p_0} \quad (2.1.18) \end{aligned}$$

When this result is subtracted from (2.1.10), we have

$$\begin{aligned}
 & \frac{\partial v}{\partial t} + \frac{\partial}{\partial y} (vv - \langle vv \rangle) + \frac{\partial}{\partial p} (\omega v) + \frac{\partial}{\partial y} (\tilde{v}v - \langle \tilde{v}v \rangle) \\
 & + u \frac{\partial \tilde{v}}{\partial x} - \langle u \frac{\partial \tilde{v}}{\partial x} \rangle + \omega \frac{\partial \tilde{v}}{\partial p} - \langle \omega \frac{\partial \tilde{v}}{\partial p} \rangle \\
 & = - f(u - \langle v \rangle) - \frac{\partial}{\partial y} (\pi - \langle \pi \rangle) \\
 & + A_m \frac{\partial^2 v}{\partial y^2} + \frac{\partial}{\partial p} (K \frac{\partial v}{\partial p}) - \left( \frac{K}{p_0} \frac{\partial v}{\partial p} \right)_{p_0} .
 \end{aligned}$$

Using (2.1.7) and evaluating at  $x = 0$ , we obtain

$$\begin{aligned}
 & \frac{\partial v}{\partial t} + \frac{\partial}{\partial y} (vv - \langle vv \rangle) + \frac{\partial}{\partial p} (\omega v) + \frac{\partial}{\partial y} (\Gamma v - \langle \Gamma v \rangle) \\
 & + D [ue^{-\xi} \sin \xi - \langle ue^{-\xi} \sin \xi \rangle - V_D \omega \frac{\partial}{\partial p} (e^{-\xi} \cos \xi) - \langle \omega \frac{\partial}{\partial p} (e^{-\xi} \cos \xi) \rangle] \\
 & = - \frac{\partial}{\partial y} (\pi - \langle \pi \rangle) - f(u - \langle v \rangle) + A_m \frac{\partial^2 v}{\partial y^2} \\
 & + \frac{\partial}{\partial p} (K \frac{\partial v}{\partial p}) - \left( \frac{K}{p_0} \frac{\partial v}{\partial p} \right)_{p_0} . \tag{2.1.19}
 \end{aligned}$$

Eq. (2.1.11) evaluated at  $x = 0$  may be written,

$$\begin{aligned}
 & \frac{\partial \theta}{\partial t} + \frac{\partial (v\theta)}{\partial y} + \frac{\partial}{\partial p} (\omega\theta) + \Gamma \frac{\partial \theta}{\partial y} \\
 & = A_\theta \frac{\partial^2 \theta}{\partial y^2} + \frac{\partial}{\partial p} [K(p) \frac{\partial \theta}{\partial p}] + Q_A + Q_M + H_C . \tag{2.1.20}
 \end{aligned}$$

Similarly, (2.1.12) becomes

$$\begin{aligned}\frac{\partial q}{\partial t} + \frac{\partial}{\partial y} (vq) + \frac{\partial}{\partial p} (\omega q) + \Gamma \frac{\partial q}{\partial y} \\ = A_q \frac{\partial^2 q}{\partial y^2} + \frac{\partial}{\partial p} [K(p) \frac{\partial q}{\partial p}] + M_A - M_C.\end{aligned}\quad (2.1.21)$$

Integrating the hydrostatic equation (2.1.14) with respect to  $p$  and removing the vertical mean, we obtain

$$\pi - \langle \pi \rangle = \int_{p_t}^p r(p) \theta dp - \langle \int_{p_t}^p r(p) \theta dp \rangle. \quad (2.1.22)$$

With (2.1.13), (2.1.16) and (2.1.19)-(2.1.22) form a complete set of equations which can be solved by a marching process.

#### B. CONVECTIVE ADJUSTMENT PROCESSES AND LATENT HEATING

This section describes the dry and moist convective adjustment processes and the latent heat release that are used in the model. The dry convective adjustment process is activated in any layer where  $\partial \theta / \partial p > 0$ . In such a layer,  $\theta$  is set equal to the average value within the layer. Then the layers above and below are tested for instability and modified if necessary. This process is represented by  $Q_A$  in (2.1.20).

When the relative humidity exceeds 100%, that is  $q > q_s$  [ $q_s(T, p)$  is the saturation mixing ratio], latent heat

of condensation will be released. To adjust the relative humidity to 100%,  $T$  and  $q$  must be changed to satisfy

$$q + \delta q = q_s(T + \delta T, p), \quad (2.2.1)$$

$$C_p \delta T = -L \delta q, \quad (2.2.2)$$

where  $L$  is the latent heat of condensation, and  $\delta q$  and  $\delta T$  are the changes in  $q$  and  $T$  during the process. A good approximation to the function  $q_s(T, p)$  is given by

$$q_s = \frac{0.38}{p} \exp\left[\frac{L}{R_v} \left(\frac{1}{273^\circ K} - \frac{1}{T}\right)\right], \quad (2.2.3)$$

where  $R_v$  is the gas constant for water vapor.

The equations (2.2.1) and (2.2.2) require that the final state of the air be exactly saturated and that excess moisture be condensed isobarically, which releases the latent heat to the air.

Equations (2.2.1) and (2.2.2) can be expressed in iterative form as

$$\delta q = q_s (1 - r) + \left(\frac{\partial q_s}{\partial T}\right)_p \delta T, \quad q = r q_s \quad (2.2.4)$$

and

$$C_p \delta T = -L \delta q. \quad (2.2.5)$$

Eliminating  $\delta T$  from (2.2.3) and (2.2.4) gives

$$\delta q = \frac{q_s(1 - r)}{1 + \frac{L}{c_p} \left( \frac{\partial q_s}{\partial T} \right)_p} . \quad (2.2.6)$$

At constant pressure, the Clausius-Clapeyron equation can be expressed as

$$\left( \frac{\partial q_s}{\partial T} \right)_p = \frac{L}{R_v} \frac{q_s}{T^2} . \quad (2.2.7)$$

Substituting (2.2.6) into (2.2.7) gives

$$\delta q = \frac{q_s(1 - r)}{1 + \frac{L^2 q_s}{c_p R_v T^2}} . \quad (2.2.8)$$

$\delta q$  may now be calculated from (2.2.8) as can the corresponding value of  $\delta T$  from (2.2.4). The first estimates of the adjusted temperature and mixing ratio are,

$$T' = T + \delta T \quad \text{and} \quad q' = q + \delta q . \quad (2.2.9)$$

These values are in turn used to obtain improved approximations. Iterations are continued until the values of  $T'$  and  $q'$  at each level match with sufficient accuracy a value of 100% relative humidity. The changes are then applied to the potential temperature and mixing ratio fields of the model, which accounts for the term  $H_c$  of (2.1.20) and  $M_c$  of (2.1.21).

The convective latent heating is parameterized by a convective adjustment scheme. The scheme yields similar results in describing the large-scale effect of latent heating as an explicit scheme which included prediction equations for water vapor, cloud water and rain water (Hsie and Anthes, 1984).

In areas where convection is occurring, it is necessary to determine whether the atmosphere is convectively unstable to moist processes. A layer will be conditionally unstable if  $\partial\theta_e/\partial p > 0$ , where  $\theta_e$  is the equivalent potential temperature, which is given by

$$\theta_e = \theta \exp\left(\frac{Lq_s}{C_p T}\right). \quad (2.2.10)$$

As with the dry convective adjustment,  $\theta_e$  is set equal to the average value in the unstable layer. This gives a value for  $\theta_e$  at each level and  $\delta T$  and  $\delta q$  can then be determined from the following calculations.

The heat release,  $Q_M$ , as a result of moist convective adjustment is included through knowledge of the change of equivalent potential temperature during the adjustment. Taking the natural logarithm of (2.2.10) gives

$$\ln \theta_e = \ln \theta + \frac{Lq_s}{C_p T} . \quad (2.2.11)$$

A constant pressure surface may be assumed since the model uses pressure coordinates. Differentiating both sides of (2.2.11) and recalling the definition of potential temperature gives

$$\frac{\delta\theta_e}{\theta_e} = \frac{\delta T}{T} + \frac{\delta q_s L}{c_p T} - \frac{L q_s \delta T}{T^2} . \quad (2.2.12)$$

Solving (2.2.6) for  $dq_s$ , substituting into equation (2.2.11) and solving for  $dT$  leads to

$$\delta T = \frac{\delta\theta_e}{\theta_e \frac{1}{T} \left[ 1 + \frac{q_s L^2}{R_v c_p T^2} - \frac{L q_s}{c_p T} \right]} \quad (2.2.13)$$

where  $\delta\theta_e$  is the change in  $\theta_e$  needed to adjust the gradient  $\partial\theta_e/\partial p$  to be equal to zero.

Since the atmosphere remains saturated throughout the process of moist convective adjustment, the Clausius-Clapeyron equation is used again to obtain the corresponding  $\delta q$  or actual  $\delta q_s$ . Changes are again applied to the potential temperature and mixing ratio fields of the model which accounts for the terms  $Q_M$  of equation (2.1.20) and  $M_C$  of equation (2.1.21). The convective adjustment with a saturated atmosphere is a rather crude parameterization of the cumulus effects. However, the relative humidity can indeed become very high in intense Mei-Yu cases (Chen and Tsay, 1978). Furthermore, the strong control by large-scale

frontogenesis forcing makes the results less sensitive to the details of the cumulus parameterization.

### C. BOUNDARY LAYER PARAMETERIZATION

The surface fluxes are parameterized by the bulk-aerodynamic formula and the surface fluxes of heat and momentum are assumed to influence directly only the lowest model layer. The magnitude of the surface stress is proportional to the square of the wind speed and the surface sensible heat flux is proportional to the product of the wind speed and the vertical gradient of temperature between the ground and the middle of the lowest model layer. This formulation is best suited to models with coarse vertical resolution, since the depth of the lowest layer should correspond to a typical PBL depth.

In this study, the vertical sub-grid scale mixing terms in Eqs.(2.2.16) are applied to the lowest layer of the model. The term may be written as

$$\frac{\partial}{\partial p} (K(p) \frac{\partial u}{\partial p}) = \frac{\partial}{\partial p} [F_u(p)] \quad (2.3.1)$$

At the top of the boundary layer, we assume

$$F_u(p) = F_u(z) = K(z) \frac{\partial u}{\partial z} . \quad (2.3.2)$$

$K(z)$  is defined as

$$K(z) = C_D |u|$$

where  $C_D$  is the drag coefficient and  $|u| = \sqrt{u^2 + v^2}$ .

Applying (2.3.2) to the lowest two layers,  $p_0$  and  $p_1$ , of the model, we get

$$\begin{aligned} F_u &= -\rho g C_D |u| (u_1 - u_0) / (p_1 - p_0) \\ &= -\rho g C_D |u| u_1 / \Delta p \end{aligned}$$

since  $u_0 = 0$  from the lower boundary condition and  $\Delta p = p_1 - p_0$ .

Therefore, the  $u$  momentum flux at the surface becomes

$$F_u = -10^{-3} \left( \frac{\rho g C_D |u|}{\Delta p} \right) u_1, \quad (2.3.3)$$

where  $10^{-3}$  is a unit conversion factor which converts the unit of pressure to cb. Similarly, the  $v$  momentum flux is

$$F_v = -10^{-3} \left( \frac{\rho g C_D |u|}{\Delta p} \right) v_1. \quad (2.3.4)$$

In this study, the PBL depth,  $h$ , is estimated as

$$h = \frac{p_0 - p_1}{\rho g} = \frac{100 - 91.9}{1.25 \times 9.81} \times 10^3 = 660 \text{ m.}$$

The sensible heat and moisture fluxes are

$$F_\theta = -10^{-3} \left( \frac{\rho g C_D |u|}{\Delta p} \right) (\theta_1 - \theta_0) \quad (2.3.5)$$

$$F_q = -10^{-3} \left( \frac{\rho g C_D |u|}{\Delta p} \right) (q_1 - q_0), \quad (2.3.6)$$

where  $\theta_0$  and  $q_0$  are the specified surface values.

The latent heat flux is defined as

$$F_L = \frac{L F_q}{C_p} , \quad (2.3.7)$$

where  $L = 2.5 \times 10^6$  Joule/kg,  $C_p = 1003$  Joule/( $^{\circ}$ K/kg).

#### D. INITIAL CONDITIONS

The initial potential temperature is given by

$$\theta(y, p, 0) = \theta_1(p) - a \left( \frac{2}{\pi} \right) \arctan(\sinh \alpha y) , \quad (2.4.1)$$

where  $\theta_1(p)$  is a prescribed vertical potential temperature profile and  $a$  is one-half the total horizontal potential temperature variation.  $\alpha$  is defined as and is evaluated  $f\pi/H \sqrt{\frac{R}{p_m} \left( \frac{p}{p_m} \right)^k \left( - \frac{\partial \theta}{\partial p} \right)_{p_m}}$  at some middle level  $p = p_m$ .

The thermal wind equation, which is derived using the hydrostatic equation and the definition of geostrophic wind, may be written as

$$\frac{\partial u}{\partial p} = \frac{1}{f} \frac{R}{p} \left( \frac{p}{p_0} \right)^k \frac{\partial \theta}{\partial y} . \quad (2.4.2)$$

Integrating (2.4.2) from  $p = p_m$  to  $p = p$

$$\int_{p_m}^p \frac{\partial u}{\partial p} dp = \frac{R}{f} \frac{\partial \theta}{\partial y} \int_{p_m}^p \frac{1}{p} \left( \frac{p}{p_0} \right)^k dp$$

and assuming  $u = 0$  at  $p = p_m$ , we obtain

$$u(y, p, 0) = \frac{C_p}{f} \frac{\partial \theta}{\partial y} \left[ \left( \frac{p}{p_0} \right)^k - \left( \frac{p_m}{p_0} \right)^k \right]. \quad (2.4.3)$$

Using (2.4.1),

$$\begin{aligned} \frac{\partial \theta}{\partial y} &= - \frac{2a}{\pi} \frac{\partial}{\partial y} [\arctan (\sinh \alpha y)] \\ &= - \frac{2a\alpha}{\pi} \operatorname{sech}(\alpha y). \end{aligned} \quad (2.4.4)$$

Substituting (2.4.4) into (2.4.3), the initial  $u$  component of the velocity may be written,

$$u(y, p, 0) = - \frac{2a\alpha C_p}{f\pi} \left[ \left( \frac{p}{p_0} \right)^k - \left( \frac{p_m}{p_0} \right)^k \right] \operatorname{sech}(\alpha y). \quad (2.4.5)$$

The  $v$  component of the velocity is set initially to zero, i.e.,

$$v(y, p, 0) = 0,$$

so that,  $\omega(y, p, 0) = 0$ .

The initial field of mixing ratio is calculated by determining the saturation vapor pressure  $e_s$  at each grid point from an integrated form of the Clausius-Clapeyron equation. According to Hess (1959),

$$e_s = 0.611 \exp \left( \frac{L}{R_v} \left( \frac{1}{T_0} - \frac{1}{T} \right) \right), \quad (2.4.6)$$

where  $T_0$  is a constant of integration. Knowing the saturation vapor pressure, the saturation mixing ratio is

obtained from the approximate relation (Haltiner and Martin, 1957).

$$q_s = \frac{0.622 e_s}{p} . \quad (2.4.7)$$

Knowing the potential temperature at  $t = 0$  from (2.4.1), it is possible to calculate  $q_s$  at each point using equations (2.4.6) and (2.4.7). Defining  $q$  to be a given fraction of  $q_s$  allows the testing of atmospheres with different initial relative humidities.

The initial conditions described in previous sections will be constrained by a simulated tropopause that is centered at about 300 mb level. The simulation is accomplished by using a reference temperature,  $T_{ref}$ , at about the midpoint of the horizontal scale and calculating temperatures such that a tropopause with the expected variation in height is determined and a zero vertical temperature gradient is achieved in the lower stratosphere. A reference temperature,  $T_{ref}$ , is computed using (2.4.1)

$$T_{ref} = 215 + a \left( \frac{2}{\pi} \right) \arctan (\sinh \alpha y) \left( \frac{p_0 - p_{ref}}{p_0} \right)^k . \quad (2.4.8)$$

When the temperature in each column reaches this reference temperature, it is held constant at that value, as expected in the lower stratosphere. The temperature is then converted to potential temperature.

### III. NUMERICAL EXPERIMENTS AND RESULTS

In this chapter two groups of numerical experiments are carried out to simulate the midlatitude and subtropical situations, respectively. For each group, the Coriolis parameter and initial temperature sounding are fixed, but the amount of the initial relative humidity and surface fluxes of momentum, mixing ratio and sensible heat are varied. The purpose here is to describe the structure differences due to the difference in latitude, relative humidity and surface fluxes. The discussion of the results, which focuses on the development of the low level jet, is given in Chapter IV.

We will first give the parameter ranges used in the experiments (in Section A), and then describe the numerical results of the midlatitude (Section B) and subtropical (Section C) cases, respectively. As mentioned in the Introduction, the main purpose for all numerical experiments is to obtain a quasi-steady solution. However, it is also of interest to follow the time evolution of the frontogenesis process to see how the quasi-steady states are developed. Therefore, in each group the evolution for a "typical case" is shown. It turns out that these evolutions provide useful insights about the different nature of the effect of cumulus convection in the midlatitude and subtropical cases.

#### A. EXPERIMENT CASES AND PARAMETERS

The following values are used for the constants in this study:

$$\begin{aligned} g &= 9.81 \text{ m s}^{-2} \\ c_p &= 1003 \text{ joule/kg/}^{\circ}\text{K} \\ R &= 287 \text{ joules/kg/}^{\circ}\text{K} \\ \kappa &= R/c_p \\ R_v &= 461 \text{ joules/kg/}^{\circ}\text{K} \\ L &= 2.5 \times 10^6 \text{ joules/kg} \\ \frac{\partial \theta_I}{\partial z} &= 5^{\circ}\text{K/km} \\ \left(\frac{\partial \theta_I}{\partial p}\right)_{p_m} &= -0.53448^{\circ}\text{K/cb} \\ p_0 &= 100 \text{ cb} \\ p_m &= 55 \text{ cb} \\ A_m &= A_q = A_\theta = 3 \times 10^4 \text{ m}^2/\text{s} \\ K_m &= K_q = K_\theta = 0.0007 \text{ cb}^2/\text{s} \\ \Delta t &= 270 \text{ sec} \\ \Delta y &= 60 \text{ km} \\ \gamma &= 2760 \text{ km} \end{aligned}$$

Each experiment is designated by a three-letter case name as follows:

LRF

where L defines the latitude environment.

1. L = M refers to a midlatitude environment, with the following parameter settings:

- a.  $f = 1.06 \times 10^{-4} \text{ s}^{-1}$  (corresponds to  $46^\circ\text{N}$ );
- b. initial vertical potential temperature distribution given by a typical midlatitude sounding (Fig. 3.1);
- c. initial meridional temperature variation is given by  $a = 8^\circ\text{K}$ ; and
- d. large-scale deformation fields given by  $D = 1 \times 10^{-5} \text{ s}^{-1}$ .

2. L = S refers to a subtropical environment, with the following parameter settings:

- a.  $f = 0.558 \times 10^{-4} \text{ s}^{-1}$  (corresponds to  $22.5^\circ\text{N}$ );
- b. initial vertical potential temperature distribution given by a typical subtropical sounding (Fig. 3.1);
- c. initial meridional temperature variation is given by  $a = 4^\circ\text{K}$ ; and
- d. large-scale deformation fields given by  $D = 0.5 \times 10^{-5} \text{ s}^{-1}$ .

3. R defines the relative humidity:

- a. R = 6 means R.H.=60%; and
- b. R = 9 means R.H.=90%.

The observed low-level relative humidity in the vicinity of a Mei-Yu front varies between 60% - 90% (Chen and Tsay, 1978). When the Mei-Yu front is north of the Yantze River (a midlatitude situation) the minimum R.H. is about 60%. When it is located over Taiwan and southeastern coast of the Chinese mainland the maximum R.H. is near 90%.

4. F defines the surface fluxes:

- a. F = 0 means there is no surface fluxes of heat, moisture, and momentum; and
- b. F = 1 means surface fluxes of heat, moisture and momentum are included.

Typically, the fluxes are large when a subtropical portion of the front is over a warm sea surface. When the front is moved over land in the midlatitude cases, the fluxes are normally weaker with the exception of momentum fluxes. For self-consistency, the fluxes of all quantities will either be included or excluded in the numerical experiments. For all cases, the initial zonal wind is calculated from the potential temperature distribution using the thermal wind, and the initial v component of the velocity is set to zero.

## B. MIDLATITUDE SIMULATIONS

### 1. Typical Midlatitude Case (M60)

The midlatitude case of M60 with an initial R.H.=60% and no surface fluxes describes the development of the front in detail. The potential temperature and mixing ratio at  $t=0$  are shown in Fig. 3.2a, and the zonal velocity at  $t=0$  is shown in Fig. 3.2b.

Fig. 3.3 depicts the development of the potential temperature and mixing ratio fields. The horizontal gradient of both fields increases steadily through the first two to three days as a frontal structure develops near  $42^{\circ}$ - $43^{\circ}$ . The maximum surface temperature gradient nearly triples (from the  $2^{\circ}$ K/degree latitude to about  $6^{\circ}$ K/degree latitude), while the maximum surface mixing ratio gradient increases nearly ten-fold (from about  $0.5$  g/kg/degree latitude to about  $5$  g/kg/degree latitude). This midlatitude mixing ratio gradient is about twice as strong as that observed in a subtropical Mei-Yu front by Chen (1978) as shown in Fig. 1.4b, and the average mixing ratio is lower (8 g/kg versus 11 g/kg). The axis of maximum mixing ratio exhibits a conspicuous poleward vertical tilt from  $41^{\circ}$  at the surface to  $48^{\circ}$  at 8 km. This poleward vertical tilt with a slope of approximately 1.1:100 agrees well with the typical midlatitude fronts (Byers, 1974). The tilt is slightly stronger than that observed in the subtropical Mei-Yu front (slope 1.3:100) as shown in Fig. 1.4b. The

development of the frontal thermal structure, including the concentration of the isentropes in the lowest 2 km and the poleward tilt of the frontal zone from the surface to the upper troposphere, is clearly indicated in Fig. 3.4. In addition, a secondary maximum occurs in the upper troposphere (6 - 8 km or 600 - 400 mb) near 50°, and a reversed tilt and reversed gradient is present in the lower stratosphere. This stratospheric structure is a result of the imposed condition of a tropopause and is consistent with previous results obtained by Williams et al. (1981).

The vertical velocity field (Fig. 3.5) quickly develops and becomes organized, with a concentrated upward motion of  $> -4.0 \times 10^{-4}$  cb/sec occurring at day 2 in the lower troposphere near 43°. A poleward vertical tilt of the area of upward motion develops and becomes more obvious with time. After day 4, a quasi-steady state clearly delineates both the upright maximum rising motion centered at 43° to 44° in the lower-middle troposphere and the vertical tilt, which is well represented by the  $\omega=0$  line poleward of the maximum rising motion.

A very small area with a secondary maximum in vertical velocity appears at day 2 near the surface ahead of the front (41°). This represents the effect of the forcing by the Ekman layer structure of the mean flow, as was discussed by Williams et al. (1981). Because this area is very close to the surface, it does not cause condensation

and latent heat release even in the highly moist cases discussed below.

The initial zonal wind (Fig. 3.2b) is in geostrophic balance with the temperature field, with an upper tropospheric westerly maximum of ~55 m/s and a surface easterly maximum of -25 m/s. The pattern is almost symmetric with respect to 46° latitude. As the integration proceeds (Fig. 3.6), asymmetries develop and a strong shear begins to appear at day 1.0 below 6 km. The shear quickly reaches a steady state with a frontal structure which tilts from 42° at the surface towards 45° at 4 km. This is in the same vicinity as the  $\omega = 0$  line and the frontal zone that is defined by the potential temperature and mixing ratio gradients. At the latitude of the surface front, a local westerly maximum develops near  $z=4$  km. By day 2 (Fig. 3.6b), this narrow westerly regime penetrates downward and appears to be an intrusion into the lower tropospheric easterlies. It remains in the 3-4 km layer through day 4. Although the magnitude of westerly wind in this narrow zone is small, the poleward meridional shear is large, which results in a vorticity in this region that is comparable to the values near the upper tropospheric westerly jet. The development of this narrow westerly regime is a result of the intensifying meridional temperature gradient which is forced by the frontogenesis process in the lower troposphere. Development of this zonal velocity field is

also dramatically illustrated by the evolution of the relative vorticity (Fig. 3.7). The initial flow pattern develops rapidly into a quasi-steady state frontal structure after about two days. Maximum cyclonic vorticity in the lower troposphere is concentrated on the warm side of the front. To illustrate the vertical structure of the horizontal wind shear with that of the horizontal temperature gradient,  $\partial\theta/\partial y = -2^\circ\text{K}/100\text{ km}$  for day 4 is plotted in the vorticity figure. A coherent vertical tilt of the frontal structure is obvious.

## 2. Other Midlatitude Cases

The effects of varying the initial relative humidity (M90), and the inclusion of surface momentum, heat and moisture fluxes (M61 and M91) are illustrated by the resulting structure at day 4 (Figs. 3.8-3.12). In addition, the precipitation and heating rates are also shown in Figs. 3.13 and 3.14, respectively.

### a. Effect of Moisture

#### (1) No Surface Flux Cases (M60 vs. M90)

It is clear that the initial R.H.=90% case (Fig. 3.8b) has higher mixing ratios in general and a warmer upper troposphere between  $40^\circ$ - $50^\circ$  (best represented by comparing the  $\theta=350^\circ\text{K}$  line). The higher temperature is a result of a larger latent heat release in the frontal region due to the increased moisture content, as can be seen by comparing the precipitation rates (Fig. 3.13). The

meridional potential temperature gradient in the surface front for the R.H.=90% case is also stronger (Figs. 3.9a versus 3.9b). The frontal zones as defined by the region  $\partial\theta/\partial y < -0.02^\circ\text{K km}^{-1}$  are quite similar in width and vertical tilt. Above the surface front position ( $\sim 42^\circ$ ), the mixing ratio in the R.H.=90% case (Fig. 3.8b) also shows a significant small scale structure with a wavelength near 2 y in the 2-7 km layer. This structure is much less evident in the R.H.=60% case (Fig. 3.8a). This small scale structure is near the region of maximum rising motion above the surface front position. The stronger vertical velocity for the R.H.=90% case (maximum rising motion  $> 6 \times 10^{-4} \text{ cb/s}$  versus  $4 \times 10^{-4} \text{ cb/s}$  for the R.H.=60% case) is consistent with the stronger cumulus convection. This convection arises because of the existence of conditional instability which is due to the prescribed 90% relative humidity. The cumulus convection activity appears to cause the small-scale variations in the mixing ratio field.

In addition to a larger maximum, the vertical velocity of the R.H.=90% (Fig. 3.10b) case also displays a more complex structure, with two concentrated regions of rising motion. The primary region near  $42^\circ\text{-}43^\circ$  extends throughout most of the depth of the troposphere from about 1 km to 11 km. The secondary region occurs in the middle-upper troposphere (5-11 km) just poleward of the primary region at about  $44^\circ$ . In addition, a third,

relatively weak, maximum upward motion occurs farther poleward near  $47^{\circ}$ . This structure is referred to as a multi-band, slanted rising motion in later discussions. This multi-band structure in the vertical velocity may be compared to some of the observed multi-band structure of cloud and precipitation associated with cold fronts during the period of CYCLES (CYCLonic Extratropical Storms) Project (Parsons and Hobbs, 1983).

As may be expected, the stronger warm core and stronger convection of the R.H.=90% case is related to a larger latent heat release. In Fig. 3.14, the heating distribution generally, resembles the rising motion field (Fig. 3.10). This is consistent with a near balance between adiabatic cooling and diabatic heating. The R.H.=90% case (Fig. 3.14b) has a maximum heating rate of  $> 6^{\circ}\text{K/day}$ , which is much higher than the  $1^{\circ}\text{K/day}$  rate of the R.H.=60% case (Fig. 3.14a). This six-fold increase in heating is consistent with the increase in precipitation rate shown in Fig. 3.13. The greater production of kinetic energy implied by the stronger rising motion of warm air gives rise to a more intense horizontal circulation (Figs. 3.11b versus 3.11a). The upper tropospheric westerly jet (Fig. 3.11b) reaches a maximum of  $> 50 \text{ m/s}$  (versus the  $> 35 \text{ m/s}$  for the R.H.=60% case) near  $52^{\circ}$ , which is two degrees poleward of the jet core of the R.H.=60% case. A small region of weak easterlies that develops equatorward of the westerly jet is

not observed in the R.H.=60% case. It is to be recalled here that these are perturbation wind fields; the basic flow is westerly throughout the upper troposphere. The distribution of the perturbation zonal wind is consistent with an anticyclonic circulation above the warm core that is due to heating. The existence of this easterly regime limits the middle-upper tropospheric westerlies to poleward of the surface front position, and makes the middle tropospheric westerly regime appear as a narrow jet-like structure that penetrates downward to below  $z=3$  km. The resultant low level westerly regime is sharper and more extensive than that of the R.H.=60% case.

On the other hand, the strength of the surface easterlies of the M60 and M90 cases is very similar. This is probably because most of the impact of a higher relative humidity is in deep cumulus convection, with the resultant increased latent heat release occurring mainly in the upper and middle troposphere, as shown in Fig. 3.14.

The maximum cyclonic vorticity is concentrated within the frontal zone in both the upper and the lower troposphere for both cases (Fig. 3.12a versus Fig. 3.12b). The stronger horizontal circulation in the upper troposphere for the R.H.=90% case is also evident in the vorticity field.

## (2) Surface Flux Cases (M61 versus M91)

When surface fluxes of momentum, moisture and heat are present, the differences between the more moist (R.H.=90%) and the drier (R.H.=60%) cases are basically similar to those between the no-flux cases. The R.H.=90% case has a warmer upper tropospheric core, as represented by the decrease of height of the  $\theta = 350^{\circ}\text{K}$  line, and again has the small-scale variation in mixing ratio in the rising motion region over the surface front location (Fig. 3.8d versus Fig. 3.8c). The meridional potential temperature gradient is stronger for case M91 than for case M61 (Fig. 3.9d versus Fig. 3.9c). The maximum upward motion, precipitation and heating rate are much larger for M91 than for M61 (Figs. 3.10, 3.13 and 3.14). Stronger wind circulations (Fig. 3.11d versus Fig. 3.11c) are shown in the R.H.=90% case. The circulation includes a more intense westerly regime of  $> 50 \text{ m s}^{-1}$  in the upper troposphere, the development of a narrow easterly regime equatorward of it, and a deeper downward extension of the upper westerlies into the low-level easterly jet. The differences in the magnitudes of vorticity (Fig. 3.12d versus Fig. 3.12c) are similar to other fields with much stronger cyclonic vorticity within frontal zone for the R.H.=90% case.

It is to be noted that the small-scale variations in all fields for the case with high mixing ratio and surface fluxes (Fig. 3.8d-3.12d) exist near surface to

the north of front. As can be seen in Fig. 3.15, this is the cold air region where the sensible and latent heat fluxes are large and apparently cause a shallow layer of conditional instability.

On the other hand, there is one noticeable difference between the comparisons of the with-flux cases and those of the no-flux cases. The multi-band vertical velocity structure in the no-flux (R.H.=90%) case (Fig. 3.10b) is not as conspicuous in the with-flux (R.H.=90%) case (Fig. 3.10d). However, a weak secondary maximum region does appear in the latter near 7 km at 46°, which indicates a double-maximum structure and a poleward tilt in the vertical structure. The physical implication of this slantwise structure in the upward motion field will be discussed later in Chapter 4.

#### b. Effect of Surface Fluxes

##### (1) R.H.=60% Cases (M60 vs. M61)

The inclusion of surface fluxes (Figs. 3.8a and 3.8c) does not lead to any discernible differences in potential temperature and mixing ratio distributions, except the mixing ratio isolines at the surface have been spread towards cold air when surface fluxes are included. Comparison between Figs. 3.9a and 3.9c shows that the surface meridional potential temperature gradient for the case with fluxes substantially weakens, although the general pattern delineating the frontal zone remains the same.

These reductions in the potential temperature and mixing ratio gradients at the surface are due to the distribution of the surface fluxes given by the bulk formula, which provides larger heat and moisture fluxes poleward of the surface front in the cooler and drier region (Fig. 3.15).

The inclusion of surface fluxes causes a slight increase in the vertical velocity (Fig. 3.10a and 3.10c). This is expected since more latent heat release occurs with the increased supply of heat and moisture from below, as shown in the comparison between Fig. 3.14c and Fig. 3.14a. Since the resultant upper tropospheric temperature is not higher (Figs. 3.8a and 3.8c), the additional latent heat release in the area of rising motion is compensated almost entirely by the increased adiabatic cooling associated with the stronger upward motion.

Increased conversion of available potential energy, as implied by the in-phase relationship between the vertical velocity and potential temperature fields, leads to a stronger upper tropospheric jet (40 m/s versus 35 m/s in the no-flux case) (Figs. 3.11a and 3.11c). On the other hand, a decrease of the surface easterlies from 40 m/s to 30 m/s occurs due primarily to the dissipation by the momentum flux transfer. The maximum easterly jet core is raised to a level slightly above the surface, and the strength and extent of the narrow lower tropospheric

westerly region appear to be slightly reduced for no-flux case.

Near the surface, the cyclonic vorticity decreases in the with-flux cases (Figs. 3.12a and 3.12c). This indicates that the weakening of the easterly maximum and thermal gradient of the front at the surface does lead to a corresponding reduction in the horizontal wind shear in the lower troposphere.

#### (2) R.H.=90% Cases (M90 vs. M91)

Similar results due to inclusion of the surface fluxes are obtained in the comparison between the with-flux and no-flux cases for R.H.=90% as in the R.H.=60% cases:

- 1) The difference in the distribution of potential temperature and mixing ratio is not discernible, except near the surface to the north of front (Figs. 3.8b and 3.8d);
- 2) At the surface, the inclusion of moisture and heat fluxes weakens the meridional gradients of mixing ratio (Figs. 3.8b and 3.8d) and potential temperature in the frontal zone (Figs. 3.9b and 3.9d) because of the stronger fluxes in the cooler and drier regions;
- 3) The surface momentum transfer leads to a weakened

surface easterly maximum (Figs. 3.11b and 3.11d), with the easterly jet core occurring slightly above the surface;

- 4) The inclusion of surface fluxes causes a stronger and more concentrated vertical velocity (Fig. 3.10) and heating rate (Fig. 3.14) in the frontal zone, so that the upper tropospheric westerly wind, the westerly regime in the middle and lower troposphere above the surface front are stronger, and the meridional wind shear in the lower troposphere is weaker (Figs. 3.11b and 3.11d and 3.12b and 3.12d); and
- 5) For R.H.=90%, the multi-band structure in vertical velocity (Figs. 3.10b and 3.10d), for the with-flux case is less conspicuous than that for the no-flux case, as was noted earlier.

### C. SUBTROPICAL SIMULATIONS

#### 1. Typical Subtropical Cases (S90)

To examine the time evolution of subtropical experiments, the case of S90 (initial R.H.=90% and no surface fluxes) is chosen as the "typical subtropical case". The initial potential temperature and mixing ratio are depicted in Fig. 3.16a and the zonal velocity is shown in Fig. 3.16b. The choice of the typical subtropical case is motivated by an intention to represent the major differences

between the mean midlatitude atmosphere and the mean subtropical atmosphere during the Mei-Yu season. The mean subtropical Mei-Yu environment is conditionally unstable with a R.H. around 85%. Furthermore, during intense convection periods when a LLJ is usually observed, the R.H. is around 90% or higher (Chen and Tsay, 1978). While these intense episodes are local and transient, and therefore cannot be properly studied by the present two-dimensional model, they are the only periods when the LLJ is clearly defined. Therefore, the somewhat higher value of R.H.=90% is chosen so that its results may also shed light to the situations when an intense LLJ is developed. In this view the "typical subtropical case" may also be considered to represent the "typical intense LLJ case."

As in the typical midlatitude case, the large-scale deformation forcing causes an accumulation of the potential temperature and moisture isolines to result in a frontal structure. However, the approach towards a quasi-steady state is slower. Furthermore, all fields develop significant small-scale variations on the equator side of the front. (For example, see the potential temperature and mixing ratio fields shown in Figs. 3.17a,b). These variations, which are similar to those in the strong convection cases of midlatitude experiments, are apparently a consequence of intense cumulus convection in the model resulting from the very moist and unstable atmosphere.

It should be noted that once the initial vertical  $\theta_e$  profile is set from the temperature sounding and relative humidity, it will remain fixed in time at lateral boundaries. Since a conditionally unstable profile occurs in the lower latitude regions (because of the initial potential temperature and mixing ratio distribution), the instability will persist on the equatorward boundary regardless of convective adjustment in the interior. This slower development into a quasi-steady state is probably due to two factors: the weaker large-scale deformation forcing ( $D=0.5 \times 10^{-5} \text{ s}^{-1}$ ) prescribed for the subtropical cases and the presence of strong conditional instability which implies more prominent cumulus convective activity.

The small-scale features also dominate the vertical velocity field such that the frontal structure is obscured by high frequency oscillations. To remove these small-scale oscillations, all the subtropical experiments fields are subjected to a daily average over 32 outputs at 45 minute intervals. Two other alternatives were considered: to increase the control of large-scale forcing, or to decrease the initial relative humidity. However, both approaches will reduce the contrasts between the midlatitude and the subtropical cases especially those cases with clearly defined LLJ, which is one of the main objectives of this study. Therefore, it was decided that the differences between the midlatitude and subtropical conditions should be

kept as large as possible to identify the underlying dynamics of the development of the LLJ. Intermediate cases with R.H.=70% and 80% will also be run to ascertain the physical significance of the intensively convective R.H.=90% cases.

The daily averages of the potential temperature and mixing ratio, and the meridional potential temperature gradient for days 2-5 are shown in Figs. 3.18 and 3.19, respectively. Here each "day" represents the average of the previous 24 hours (i.e., day 5 is the average between 96-120 h). In these diagrams, the small-scale features have been filtered out, and the development of the frontal structure is clearly evident. The surface mixing ratio gradient and range agree reasonably well with Chen's (1978) observations (Fig. 1.4b).

The meridional potential temperature gradient also evolves into a frontal structure near the surface around  $16^{\circ}$  after 4 days (Fig. 3.19). The tilt of the frontal zone is similar to the midlatitude case (Fig. 3.4), but the well-defined frontal zone is confined to the lower troposphere. Chen and Chang's (1980) comparison between different segments of an elongated Mei-Yu front that extends from the subtropical southern China to the midlatitude central Japan. They observed that the subtropical segment of the front has less vertical tilt and is shallower than the midlatitude segment. These differences were attributed to the stronger

convection in the subtropics. It will be shown later that in the subtropical with-flux case (S91) the tilt is indeed less while the vertical extent remains shallow.

By day 2, the concentrated rising motion (Fig. 3.20) develops in the equatorial latitudes and then moves poleward towards the area of maximum deformation forcing. At day 3, the maximum rising motion is at  $16^\circ$  with a magnitude  $\sim 17 \times 10^{-4}$  cb/sec. After day 4, it shifts to  $18^\circ$  and the maximum decreases to  $4-5 \times 10^{-4}$  cb/sec. This is the process for the model to develop the Mei-Yu front from an initial zero-perturbation state. In the real atmosphere, the process is much slower, where the monsoon trough, which is developed over a seasonal time scale, is already in place when the front moves into the Mei-Yu position from the north. The development of a slanted structure in the lower ( $z=0-3$  km) and upper parts ( $5-10$  km) of the concentrated rising region is evident. The slanting is northward with height, in the same sense as the slope of the frontal surface. The multi-band structure is not clearly seen in the 24-h averaged vertical velocity field but is more clearly visible when instantaneous (not daily-averaged) vertical velocity fields are examined. An example is given in Fig. 3.21, which is the instantaneous vertical velocity at the time-step of day 4.5.

The evolution of the zonal wind is illustrated in Fig. 3.22. The gross structure of an upper tropospheric

westerly jet, poleward of a lower tropospheric easterly jet with a maximum at the surface, roughly resembles that of the typical midlatitude case (M60, Fig. 3.6). However, there are significant differences. The subtropical westerly jet core is lower (at 10 km), shallower and wider in the meridional direction. These features are different from what would be expected for the mean polar front jet and subtropical jet. Compared to Chen's (1978) observation of a subtropical Mei-Yu case (Fig. 1.4a), the jet core is lower. The reason for the lower jet core (at 10 km versus 12 km in Fig. 1.4a) is apparently the fixed tropopause which is imposed by the mean sounding at 10 km. In an intense Mei-Yu period, the deep convection and the tropopause are a couple of kilometers higher, where the jet maximum is also located. On the other hand, the meridional extent of the simulated westerly regime and that observed are comparable. A significant easterly regime occupies the entire tropical upper troposphere and caps a westerly regime in the tropical lower troposphere. In Fig. 1.4a, the observed zonal wind is also easterly in the upper level tropics, although the area is somewhat higher and more equatorward than the simulation. The imposed tropopause in the model is again the reason for this difference.

Within the tropical low-level westerly regime is a remarkably strong and narrow jet structure centered at  $z=3$  km at the latitude of maximum rising motion. This low level

jet first appears at day 2 with a magnitude  $\sim 5$  m/s. It develops to  $> 10$  m/s at day 5. In terms of the relative position with respect to the front, this low level jet is similar to the local lower-tropospheric westerly regime simulated in the midlatitude cases, but the intensity is much stronger. This intensity agrees reasonably well with the observed LLJ strength in Fig. 1.4b, especially when the addition of a mean westerly is considered.

The strong horizontal wind shear that develops around the frontal zone is shown in Fig. 3.23. Compared to Fig. 3.7, this subtropical case has a deep lower tropospheric shear zone that extends into the middle troposphere, and its magnitude poleward of the low level jet significantly exceeds that of the upper tropospheric maximum. The slope of the frontal shear zone is again larger (less vertical tilt) in the subtropical case than in the midlatitude case (Fig. 3.7), at least in the lower troposphere. In Fig. 3.23d, a region of strong negative relative vorticity exists above the surface front near 10 km, which indicates the possibility of inertial instability. This is the consequence of the intense convection and may not be physically realistic. It is not known whether this instability contributes to the small-scale variations.

To demonstrate that the five-day integration gives a reasonable quasi-steady state, the averages of each field

over the first five days of integration was used as the initial conditions for another integration of 120 h. The results of potential temperature and mixing ratio, meridional potential temperature gradient, vertical velocity and zonal wind for the (daily averaged) new day 5 are shown in Fig. 3.24a-d. These fields are similar to those of the original daily averaged at day 5 (Figs. 3.18, 3.19, 3.20 and 3.22). This result indicates that the daily averaged fields are stable in time, in spite of the presence of small-scale variations and possible inertial instability.

The subtropical frontal positions as indicated by the various fields are farther equatorward from the central axis of deformation forcing than that of the midlatitude cases. In the midlatitude case, the central axis of deformation is at  $46^{\circ}$  and the frontal structure near the surface develops at about  $42^{\circ}$ . In the subtropical case, the axis of deformation is at  $22.5^{\circ}$ , while the surface frontal zone is near  $16^{\circ}$ . This increased distance apparently reflects the effect of the smaller Coriolis parameter which leads to a relatively larger ageostrophic secondary circulation around the frontal zone. The advection by the lower branch of this enhanced secondary circulation tends to move the surface front farther equatorward. In addition, the effect of a possible secondary circulation south of the front, that is induced by the strong convection, may also

contribute to the more equatorward position of the surface front.

## 2. Other Subtropical Cases

As in the midlatitude experiments, the effects of varying the initial relative humidity and surface fluxes are studied by running three additional subtropical cases (S60, S61 and S91). The resultant structure at day 5, averaged over the preceding 24-h period, for all four subtropical cases are shown in Figs. 3.25-3.29. The precipitation and heating rates are shown in Figs. 3.30-3.31. In these cases, no significant small-scale variations are present, so the averaging is unnecessary. Nevertheless, it is done to make the analysis procedure of all subtropical cases consistent.

### a. Effects of Moisture

Panels a and b in Figs. 3.25-3.29 are for S60 (R.H.=60%, no-flux) and S90 (R.H.=90%, no-flux) cases, respectively. The R.H.=60% case (Fig. 3.25a) has a less intense moisture front throughout the lower troposphere. The poleward vertical tilt of the maximum mixing ratio gradient is about the same as in the R.H.=90% case (Fig. 3.25b). However, the curvature near the axis of the maximum mixing ratio does not appear as sharp as in the R.H.=90% case due to the drier air and weaker gradient. The short-wave feature in the middle troposphere over the surface front position is not as intense as in the R.H.=90% case, but it is still very notable, which indicates the

presence of significant cumulus convection. As may be expected, the R.H.=60% case has a lower temperature in the upper troposphere (Figs. 3.25a and 3.25b). The small-scale variations near the surface in the cold air (Fig. 3.25d-3.27d), as seen in midlatitude cases, evidence the shallow layer of conditional instability caused by surface heat fluxes. The conditional instability can be examined further by calculating the  $\theta_e$  field which will be shown later in Fig. 4.6 (midlatitude cases) and 4.7 (subtropical cases). The weaker meridional potential temperature gradient in the frontal zone can be seen by comparing Figs. 3.26a and 3.26b, both of which also show less small-scale features elsewhere in the domain. The vertical tilt of the frontal zone is somewhat larger and the frontal zone extends to a slightly lower height at the poleward boundary.

---

The vertical velocity of the R.H.=60% case (Fig. 3.27a) has a concentrated zone of rising motion in the lower and middle troposphere, but the magnitude is less than in the R.H.=90% case.

The zonal wind of the R.H.=60% case is much weaker than in the R.H.=90% case (Fig. 3.28a versus Fig. 3.28b). The upper tropospheric westerly jet maximum of < 25 m/s is only about 70% of the > 35 m/s magnitude of the R.H.=90% case. This is consistent with the expected difference in the energy conversion between the two cases, as the heating rate and the upward motion (which correlates

almost completely with the heating of the warm air is stronger for the R.H.=90% case. The former is also situated more equatorward. The low-level westerly jet structure still persists, but the magnitude is reduced by half. The upper tropospheric easterly regime almost disappears, and the surface easterly maximum is only reduced slightly (Fig. 3.28a and Fig. 3.28b). These features also appear in the comparison between Figs. 3.29a and b, which primarily indicates a significant reduction of upper tropospheric horizontal wind shear.

When fluxes are included, the comparison between the R.H.=60% (S61) and R.H.=90% cases (S91) [panels c and d in Figs. 3.25-3.31, respectively] yields similar results. In general, the meridional temperature and mixing ratio gradients and the zonal wind are stronger in the R.H.=90% case.

The subtropical R.H.=90% cases are included to study the intensely convective Mei-Yu situations when the LLJ is fully developed. However, the high initial moisture and the subtropical sounding make the atmosphere highly conditionally unstable. The resultant high frequency, small scale variations are removed by the 24 h averaging. Even though the averages remain stable for extended integrations, a question may still be asked as to whether the results are not distorted seriously by the small-scale variations. Therefore, two intermediate with-flux cases, R.H.=70% (S71)

and R.H.=80% (S81), are run to assess the physical significance of the S91 case. Fig. 3.33 compares the 24-h averaged zonal wind of all four subtropical, with-flux cases. Here it can be seen that the pattern of all four cases are similar. The midlatitude upper level westerlies, lower level easterlies, tropical upper easterlies are present in all cases, and the intensity of these features increases systematically as the initial R.H. increases from 60% to 90%. The LLJ is indicated by a very small area of 5 m/s in the S61 case (Fig. 3.33a), this area expands considerably with increasing humidity. When the R.H. reaches 90% (Fig. 3.33d), the jet maximum becomes  $> 10$  m/s. The similarity in the structure, and the consistent intensification of the circulation with increasing moisture, indicate that the subtropical R.H.=90% results can indeed be viewed as physically relevant to the strong LLJ situations.

#### b. Effects of Surface Fluxes

When surface momentum, heat and moisture fluxes are included (Fig. 3.32), these important contrasts continue to exist, as seen by comparing panels b and d in Figs. 3.25-3.31. Similar to the midlatitude experiments, the addition of surface heat, moisture and momentum fluxes leads to a higher upper tropospheric temperature. This is apparently due to the increased precipitation and the associated latent heat release (Figs. 3.30 and 3.31), which are to be expected from the increased sensible and latent heat supply (Fig.

3.32). A weaker potential temperature and mixing ratio gradient at the surface (Figs. 3.25 and 3.26) is due to the stronger surface fluxes of heat and moisture in the cooler and drier region (Figs. 3.32).

The vertical velocity of the with-flux case displays the stacked multi-band structure slanted upward and poleward in the surface frontal zone (Figs. 3.27b and d). Also, the magnitude of updraft is greater than in the no-flux case. This is consistent with the precipitation and heating rates (Figs. 3.30 and 3.31) and is due to the additional moisture supply from the lower boundary (Fig. 3.32).

Comparisons between Figs. 3.28a and 3.28c, and between Figs. 3.28b and 3.28d show the effects of surface fluxes on the horizontal circulation, which are basically similar to the results of the midlatitude experiments. When fluxes are included, the upper tropospheric zonal winds, including both the westerly jet and the less intense easterly jet, are enhanced. The lower tropospheric westerly jet near 3-4 km for the R.H.=90% case (Fig. 3.28d) also intensifies. Due to the momentum dissipation at the surface (Fig. 3.32), the surface easterlies weaken, and the jet core is shifted slightly upward (Figs. 3.29b and d).

The comparisons of the surface fluxes and no fluxes for the R.H.=60% cases (panels a and c of Figs. 3.25-3.29) basically illustrate similar results.

#### D. SUMMARY OF THE RESULTS

The results of the foregoing numerical experiments may be summarized as follows:

- 1) In the midlatitude case, the zonal velocity field is dominated by a westerly regime occupying almost the entire upper troposphere and an easterly regime occupying the lower troposphere. On the other hand, in the subtropical cases, the zonal flow equatorward of the front tends to reverse, with expansive easterlies in the upper troposphere and weak westerlies in the lower troposphere. A small regime of easterlies develops in the midlatitude upper troposphere only in the high-humidity cases.
- 2) At the latitude of the maximum rising motion, a narrow westerly wind regime occurs in the lower troposphere. In midlatitude cases, it appears as a small downward (and equatorward) penetration of the upper tropospheric westerlies. In the subtropical cases, it exists distinctly as a well-defined, westerly maximum similar to the low-level jet.
- 3) The poleward tilts of all fields except vertical velocities are more prominent in the midlatitude cases are either comparable or stronger than in the

subtropical cases. The frontal zone also extends higher in the midlatitude cases. These are in agreement with observations (e.g., Chen and Chang, 1980).

- 4) The inclusion of higher initial humidity values or of surface fluxes tends to give stronger vertical velocity and upper tropospheric zonal winds. This is a result of stronger cumulus convection and precipitation whose latent heat release provides more energy input to the upper troposphere. At lower levels, the easterlies weaken as a consequence of the momentum dissipation at the surface.
- 5) When the vertical velocity is intense, a multi-band structure often appears. It is characterized by more than one concentrated updraft region, stacked closely to each other along the poleward slanted frontal surface. The stronger updraft is situated equatorward and has a larger vertical extent.
- 6) The frontal zone develops equatorward of the dilation axis of the large-scale deformation forcing. In the midlatitude cases, the frontal zone is closer to this axis (about  $4^{\circ}$  latitude separation at the surface), while in the subtropical cases the separation is greater (about  $5-6^{\circ}$ ) at the surface. This is apparently a result of the smaller  $f$  and, therefore, a relatively larger ageostrophic wind which advects the surface front farther equatorward. In addition, the effects of the

convection-induced secondary circulation may also contribute to the more equatorward position of the surface front.

In the ensuing section these numerical results will be discussed in relationship to the development of the low-level westerly jet.

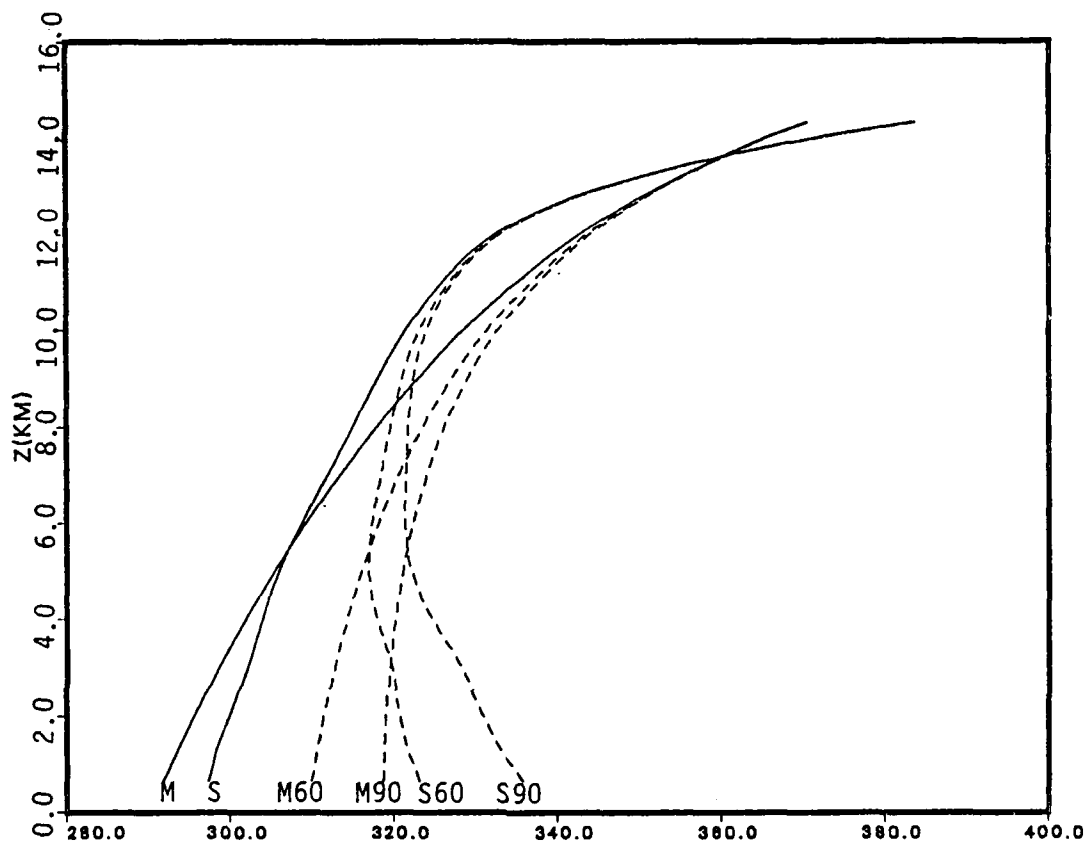


Fig. 3.1 Initial potential temperature (solid),  $\theta$  ( $^{\circ}$ K), and equivalent potential temperature (dash),  $\theta_e$  ( $^{\circ}$ K), soundings at the center of the model domain for midlatitude cases - M60 and M90 and subtropical cases - S60 and S90. (see text).

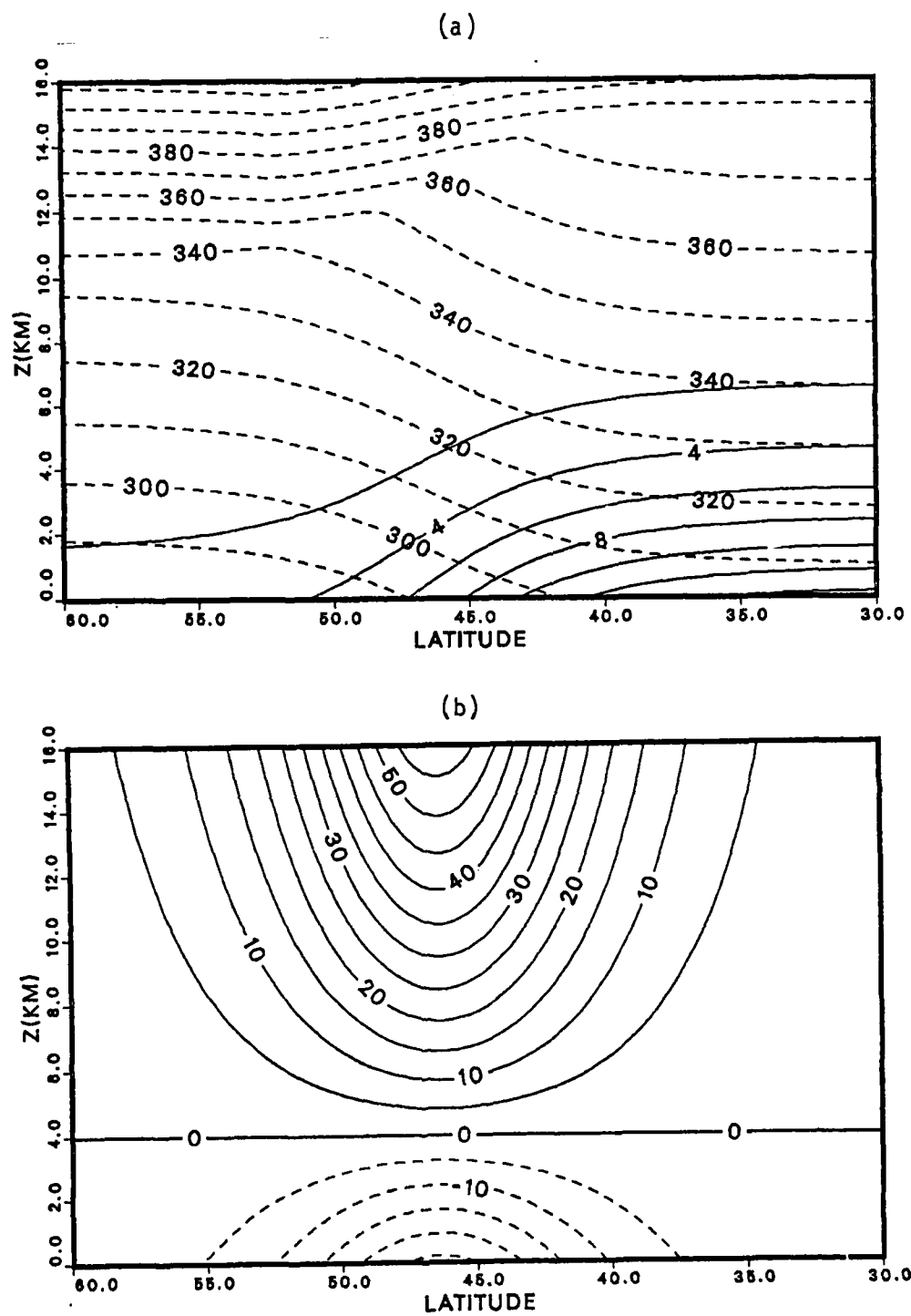


Fig. 3.2 Cross section of (a) mixing ratio (solid),  $q(\text{g kg}^{-1})$ , and potential temperature (dash),  $\theta(\text{°K})$ , (b) westerly (solid) and easterly (dash) zonal wind,  $U(\text{m s}^{-1})$  for typical midlatitude case, M60, at day 0.

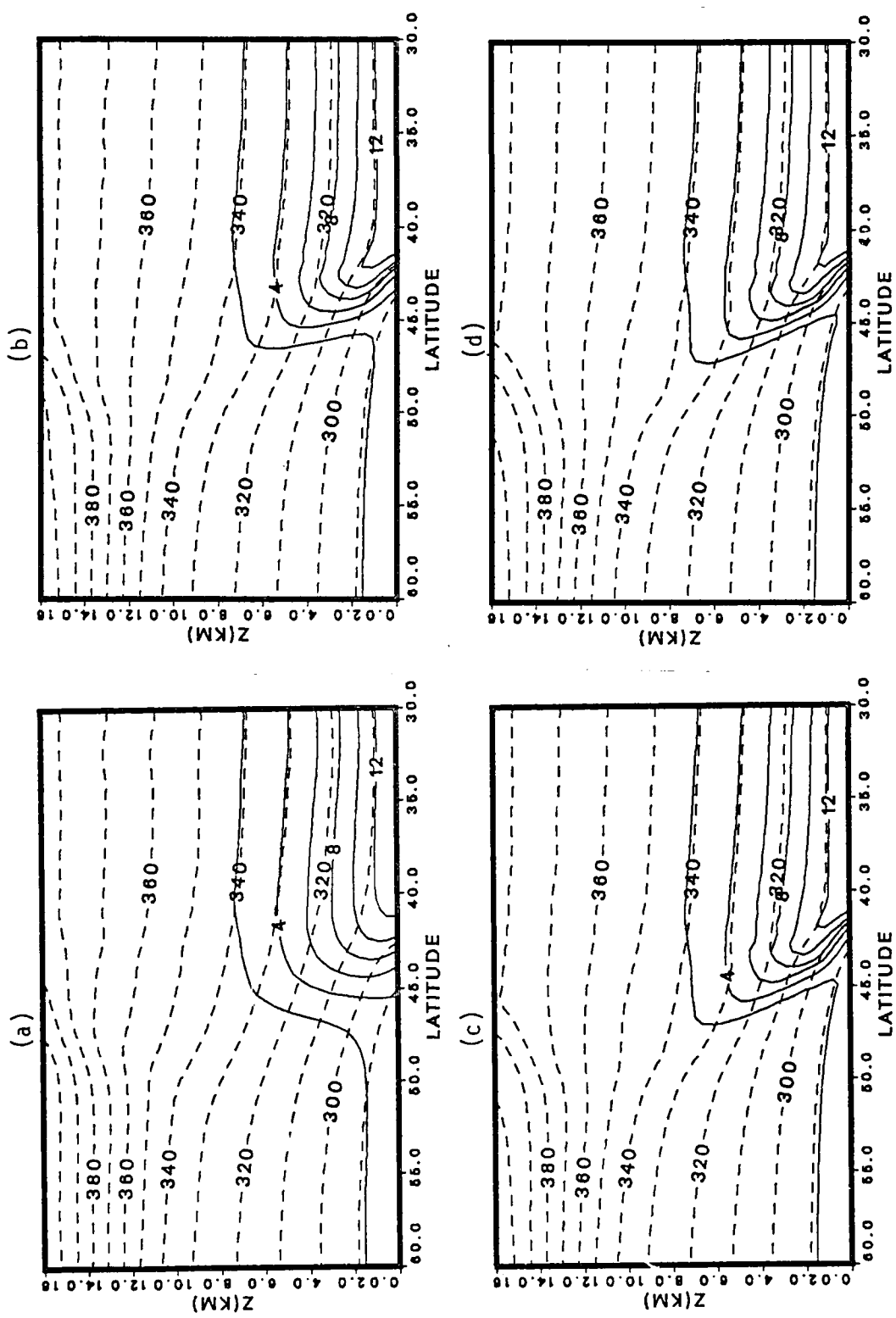


Fig. 3.3 Cross section of mixing ratio (solid),  $q(\text{g kg}^{-1})$ , and potential temperature (dash),  $\theta (\text{°K})$ , for typical midlatitude case M60, at (a) day 1.0, (b) day 2.0, (c) day 3.0, (d) day 4.0.

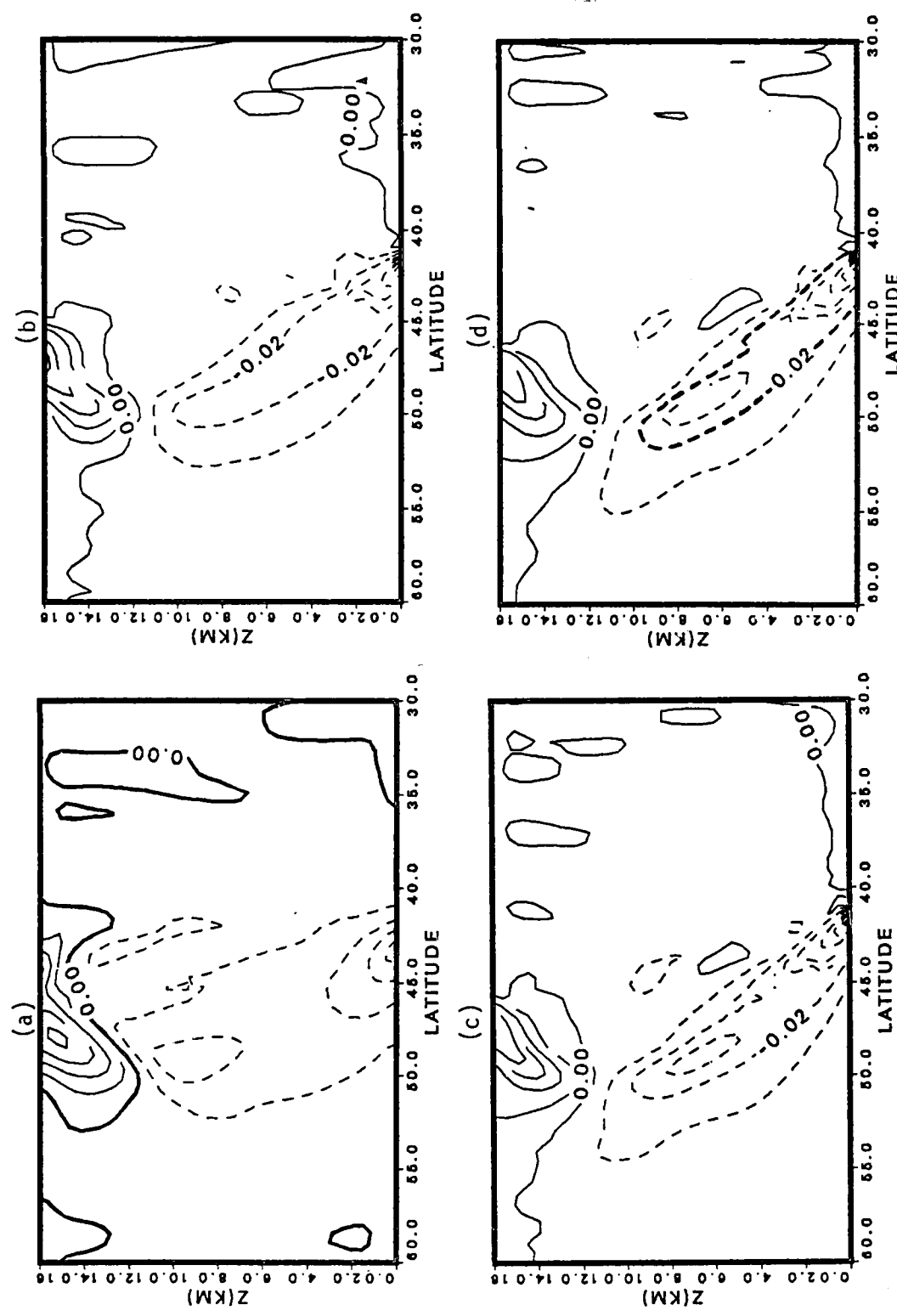


Fig. 3.4 As in Fig. 3.3, except for horizontal potential temperature gradient,  $\partial\theta/\partial y$  ( $^{\circ}\text{K km}^{-1}$ ). Heavy dash lines at day 4, ( $-0.02 ^{\circ}\text{K km}^{-1}$ ) indicate frontal zone.

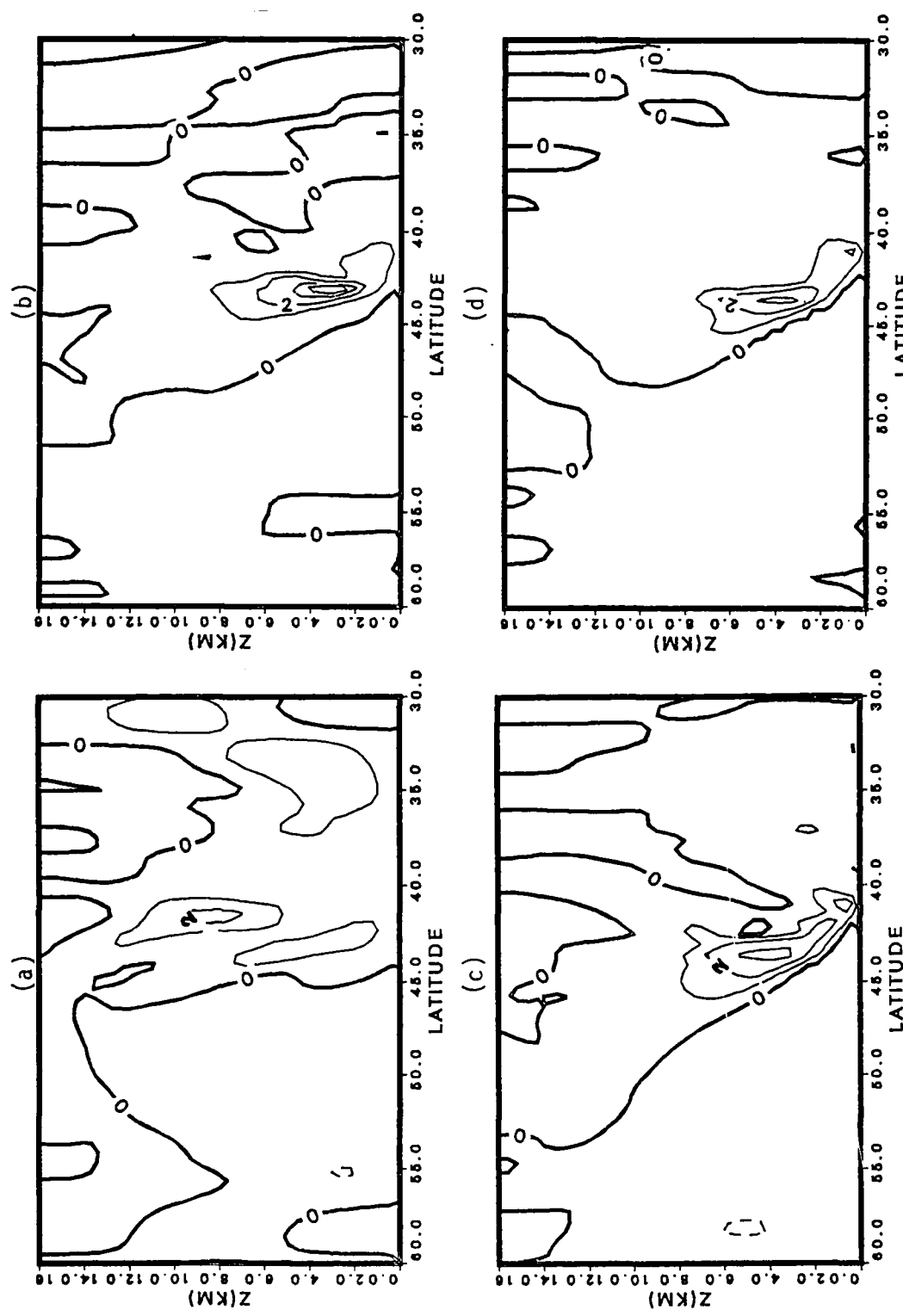


Fig. 3.5 As in Fig. 3.3, except for vertical pressure velocity,  $-\omega$  ( $10^{-4}$   $\text{cb s}^{-1}$ ).

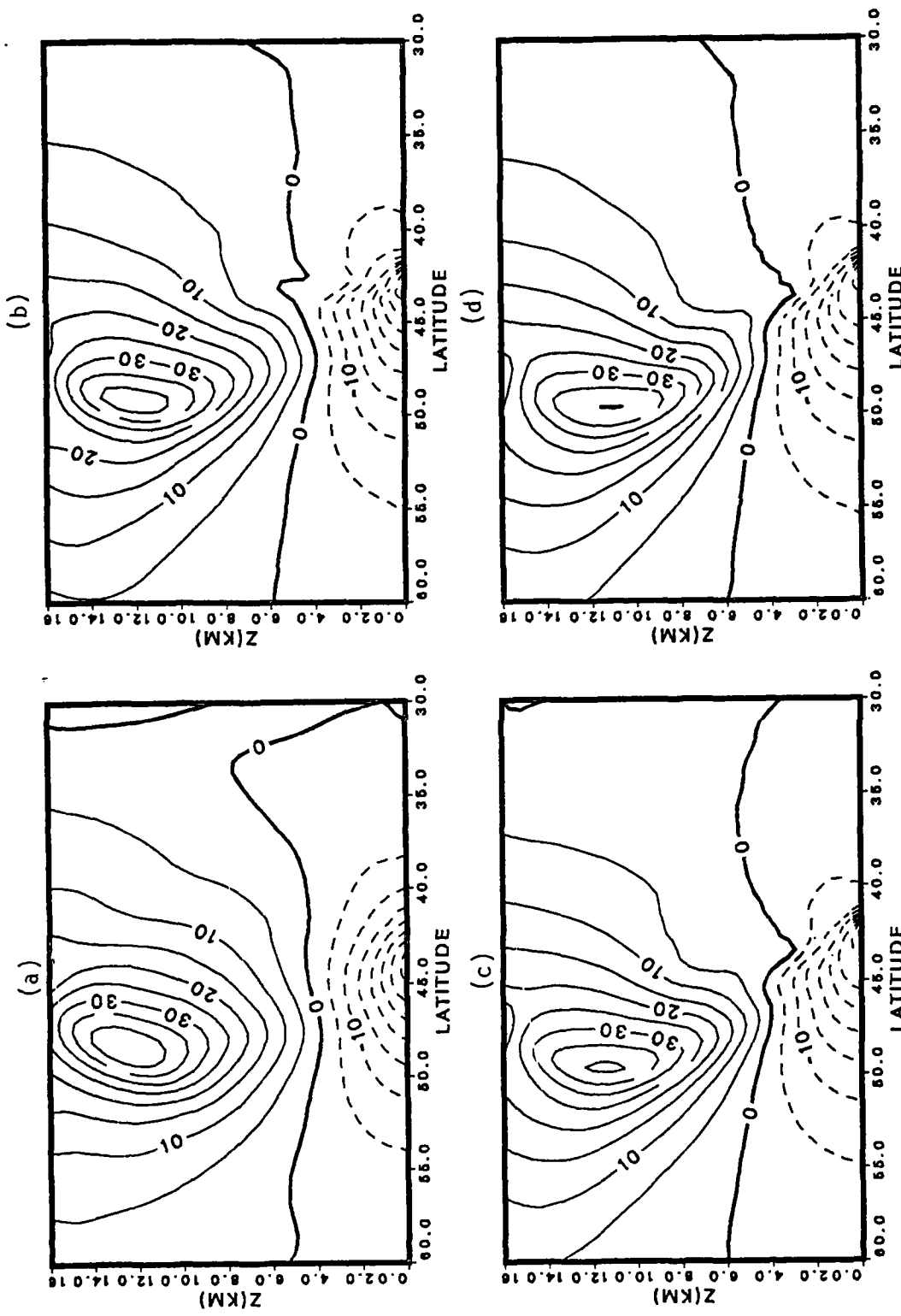


Fig. 3.6 As in Fig. 3.3, except for zonal wind speed,  $U$  ( $\text{m s}^{-1}$ ).

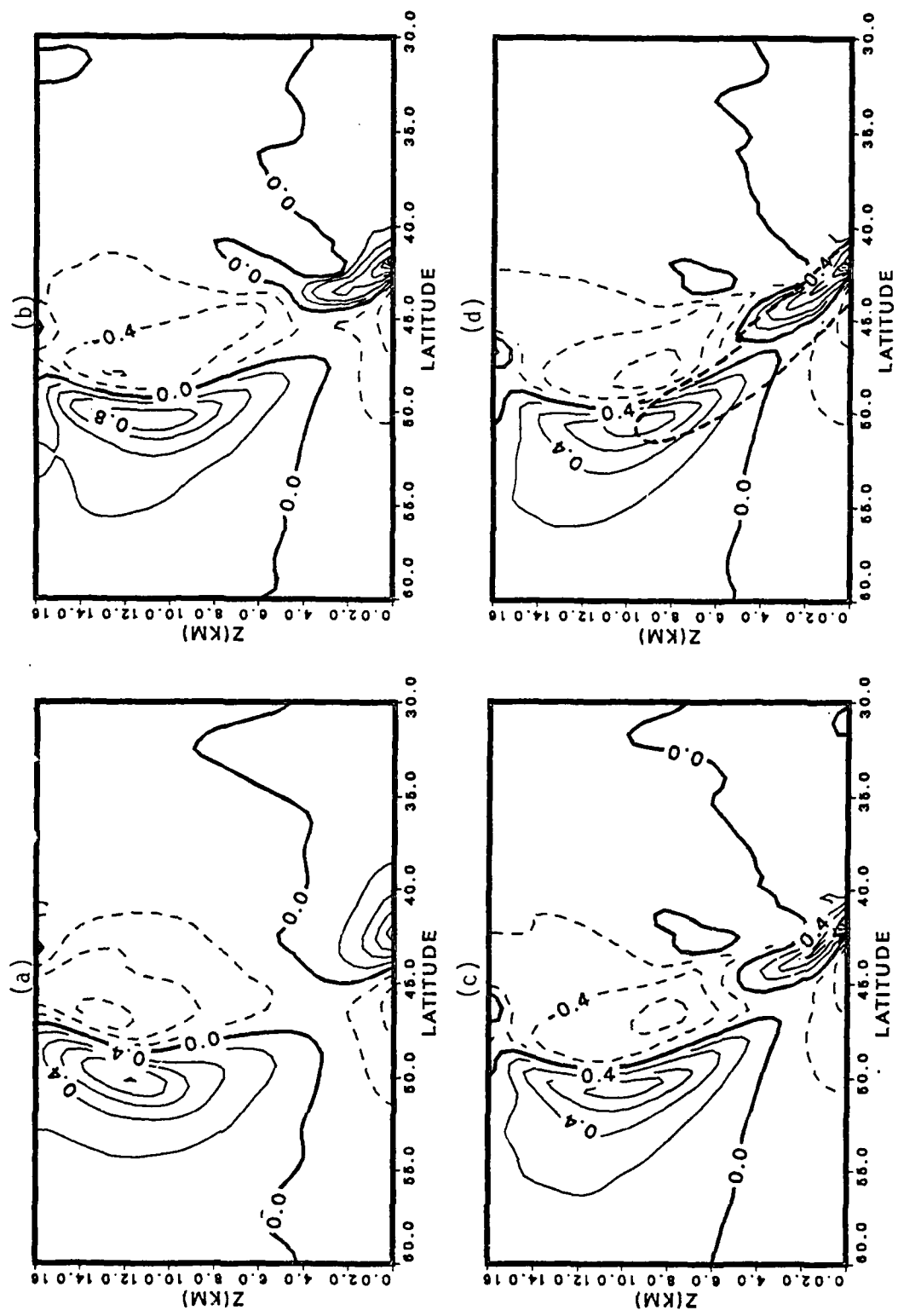


Fig. 3.7 As in Fig. 3.3, except for vorticity,  $\zeta$  ( $10^{-4}$   $s^{-1}$ ). Heavy dash lines indicate frontal zone.

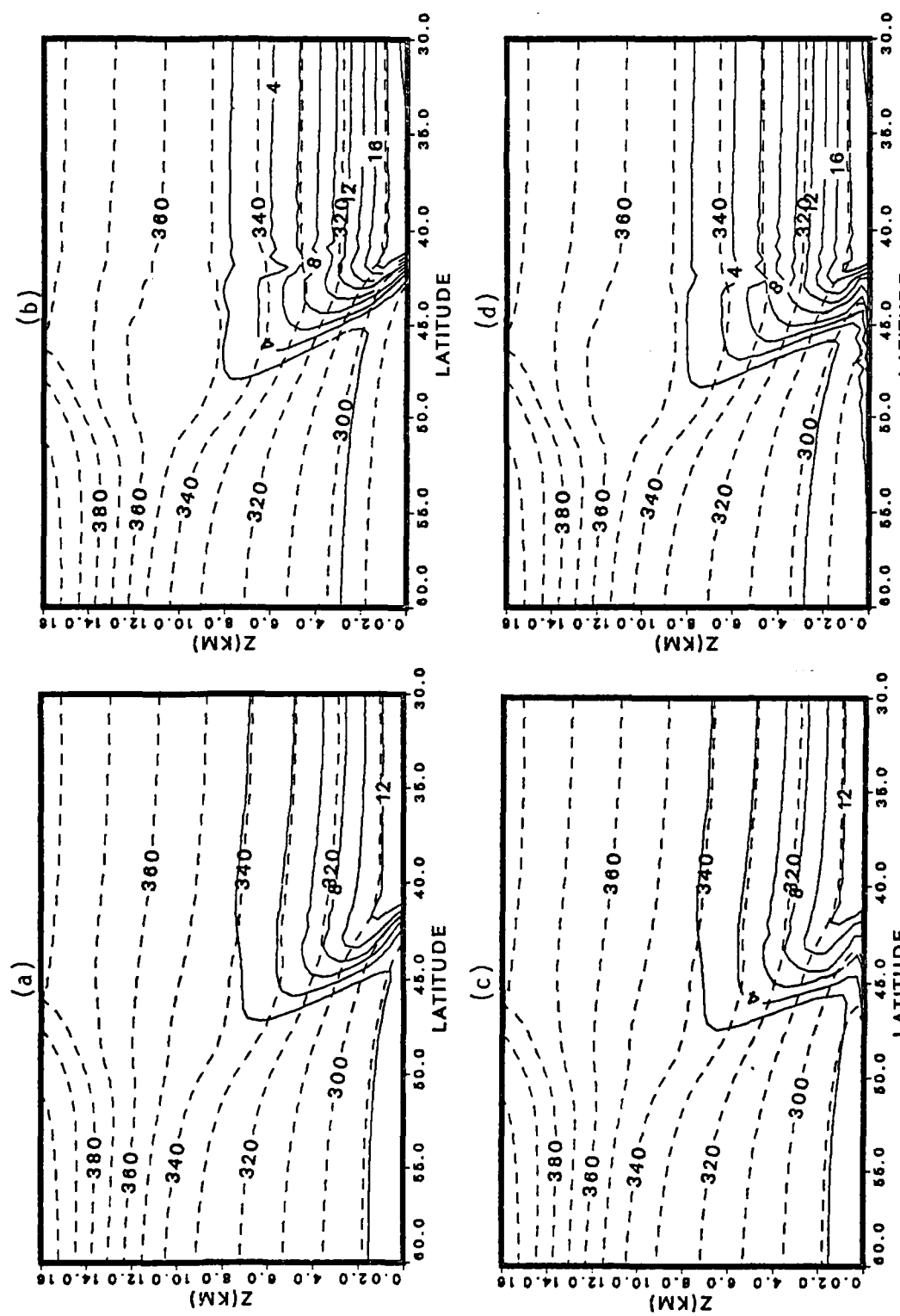


Fig. 3.8 Cross section of mixing ratio (solid),  $q(\text{g kg}^{-1})$ , and potential temperature (dash),  $\theta (\text{°K})$ , for different midlatitude cases at day 4, (a) M60, (b) M90, (c) M61 and (d) M91 (see text).

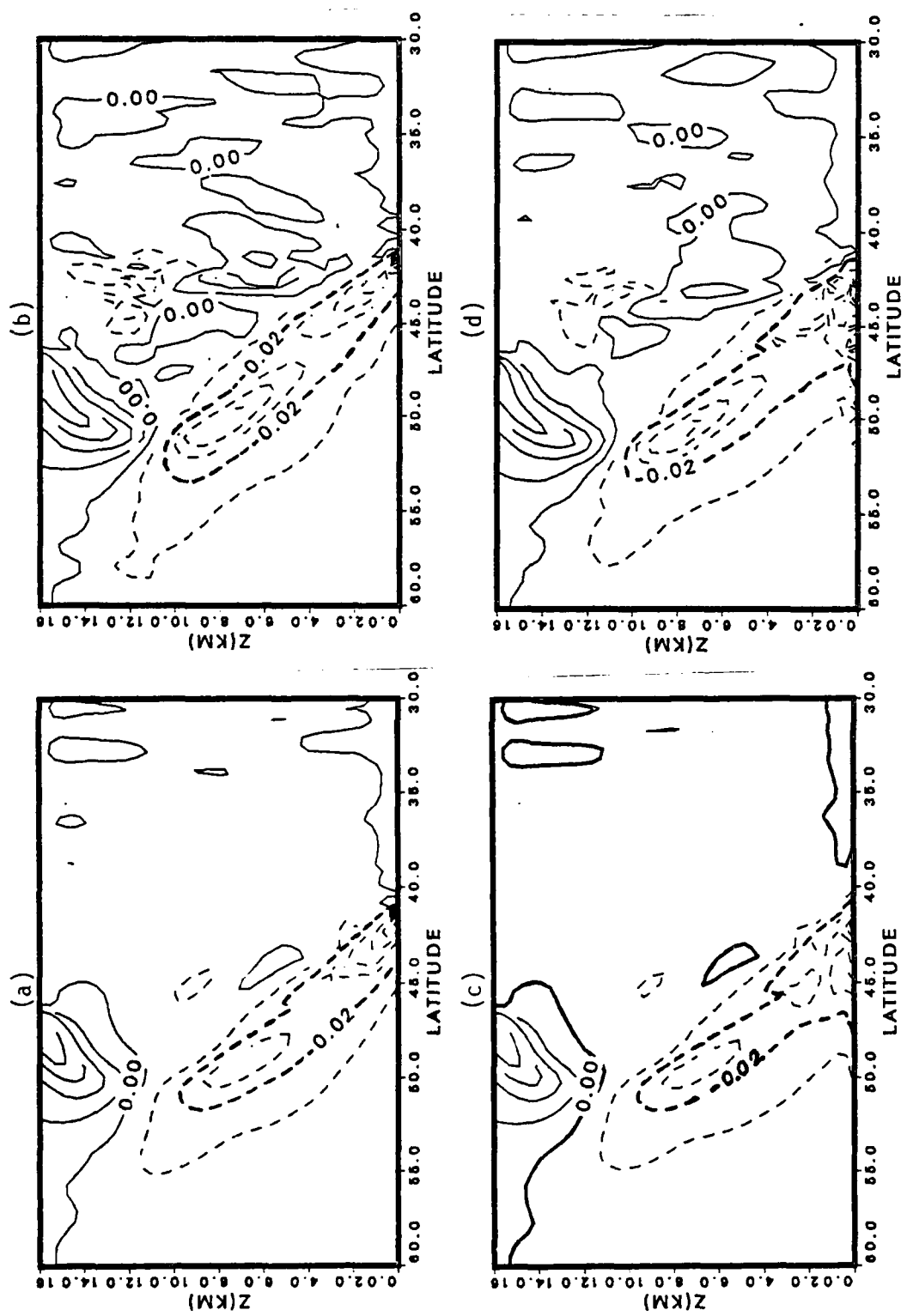


Fig. 3.9 As in Fig. 3.8, except for horizontal potential temperature gradient,  $\partial\theta/\partial y$  ( $^{\circ}\text{K km}^{-1}$ ). Heavy dash lines indicate frontal zone.

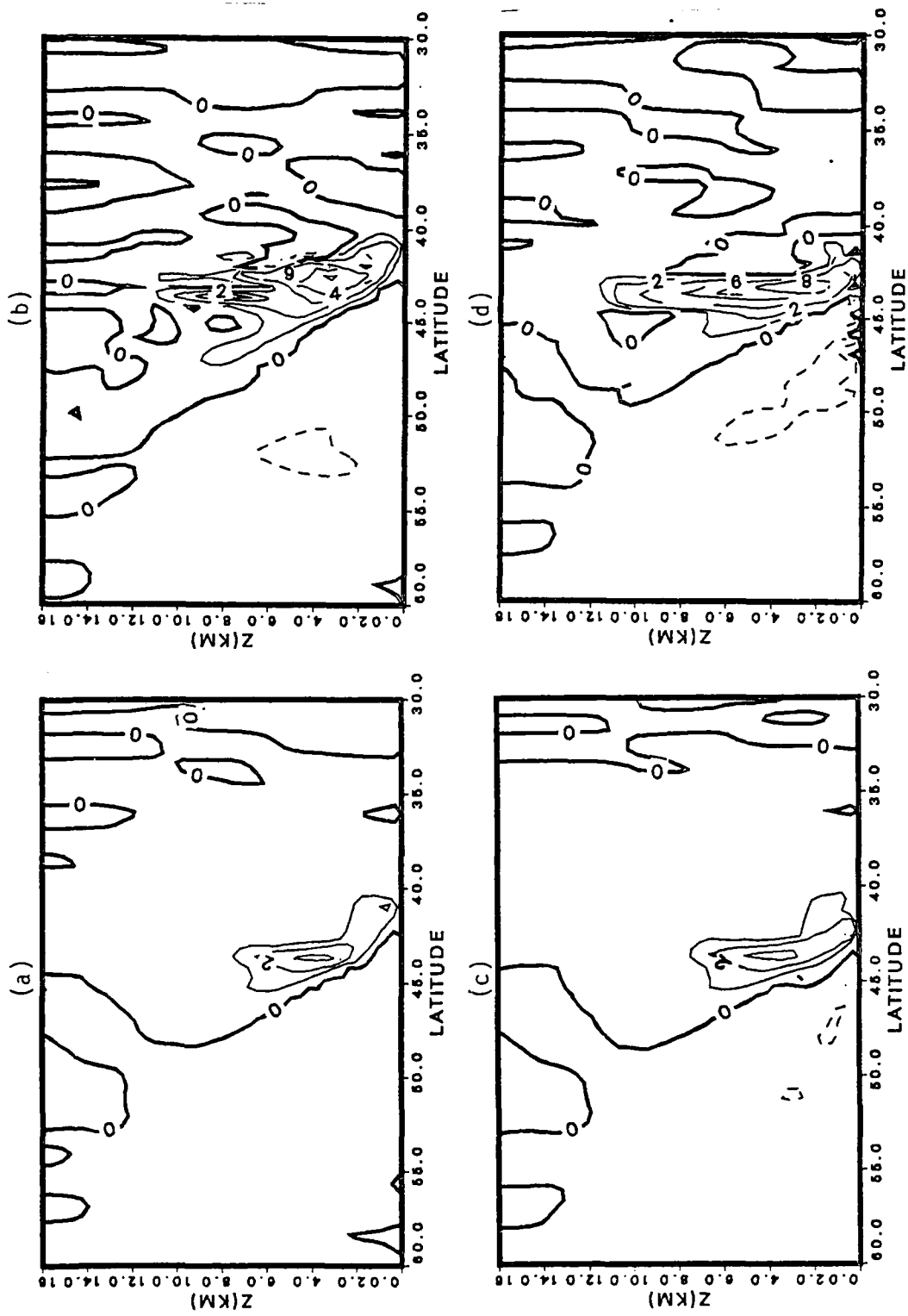


Fig. 3.10 As in Fig. 3.8, except for vertical pressure velocity,  $-\omega(10^{-4} \text{ cb s}^{-1})$ .

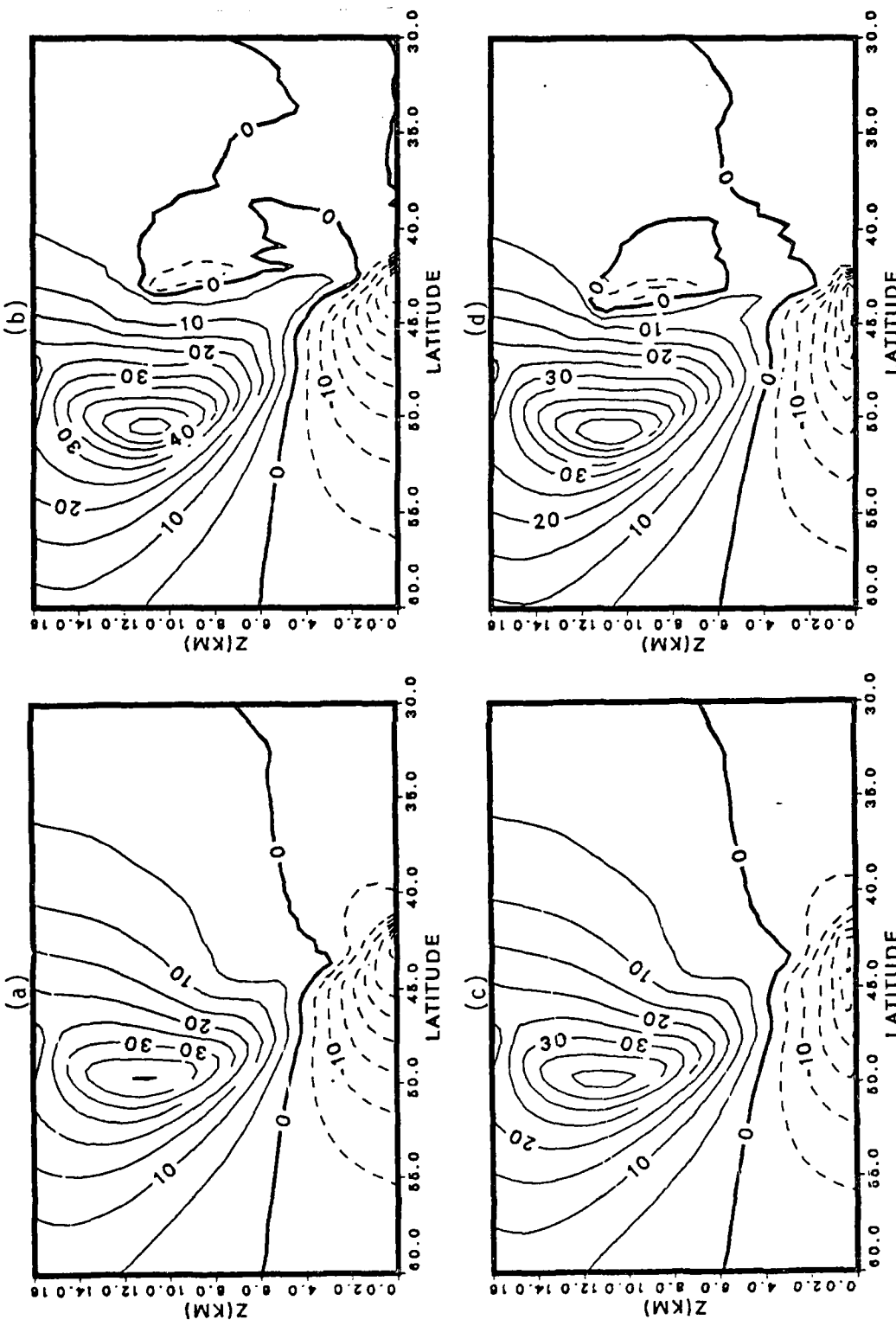


Fig. 3.11 As in Fig. 3.8, except for zonal wind speed,  $U(\text{m s}^{-1})$ .

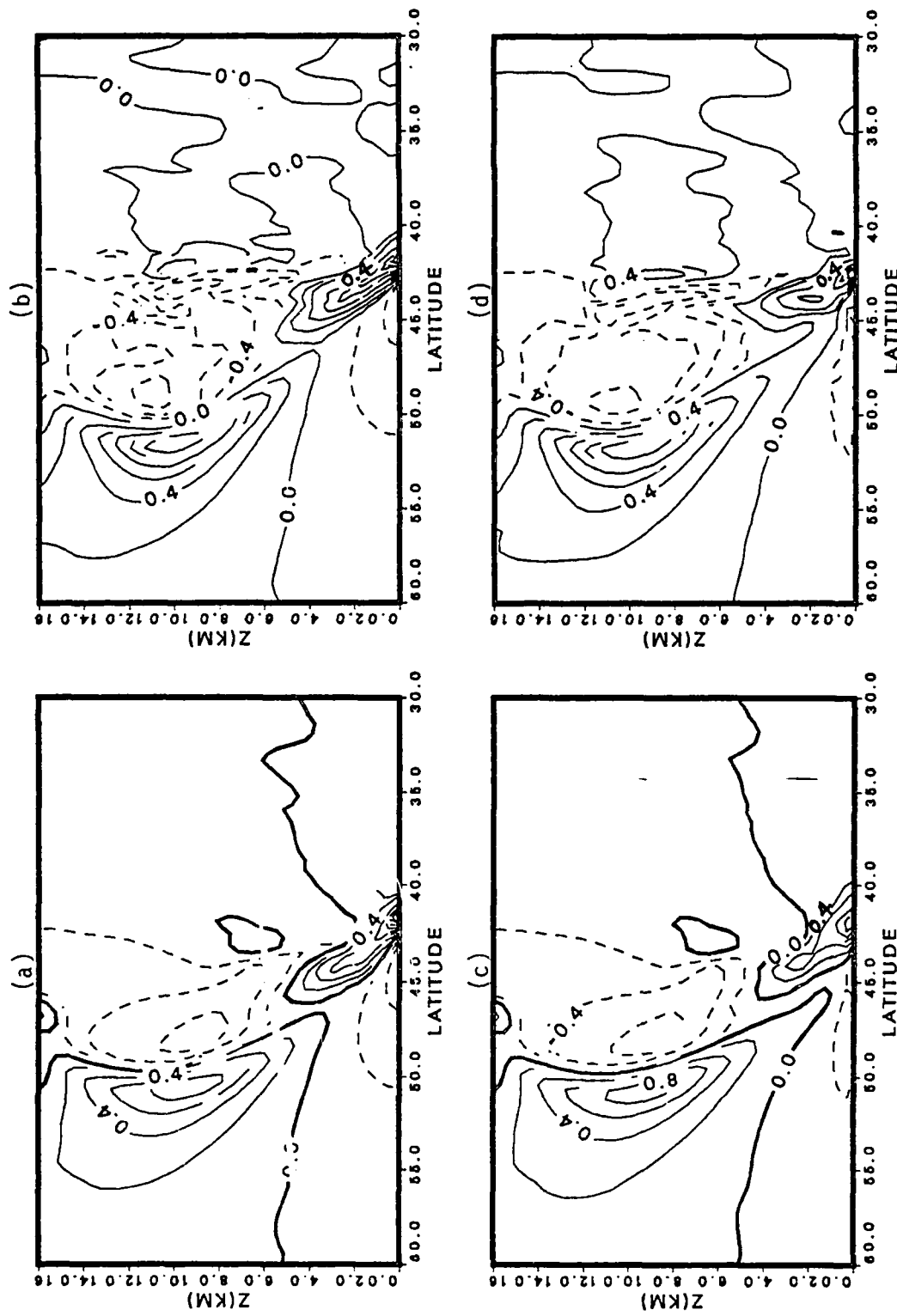


Fig. 3.12 As in Fig. 3.8, except for vorticity,  $\zeta$  ( $10^{-4} \text{ s}^{-1}$ ).

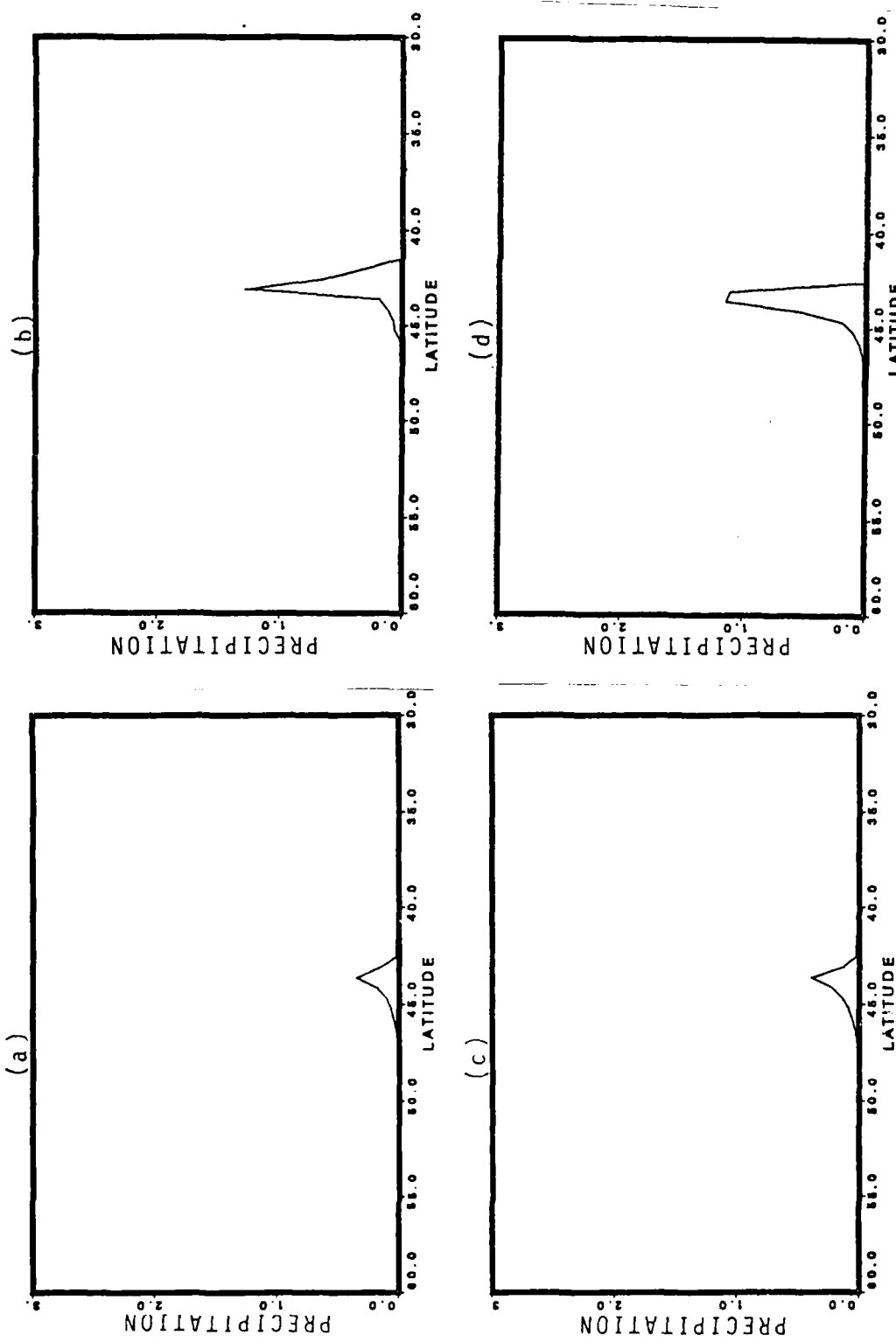


Fig. 3.13 Precipitation rate for midlatitude cases in units of cm day<sup>-1</sup>, (a) M60, (b) M90 (c) M61 and (d) M91.

AD-A175 267

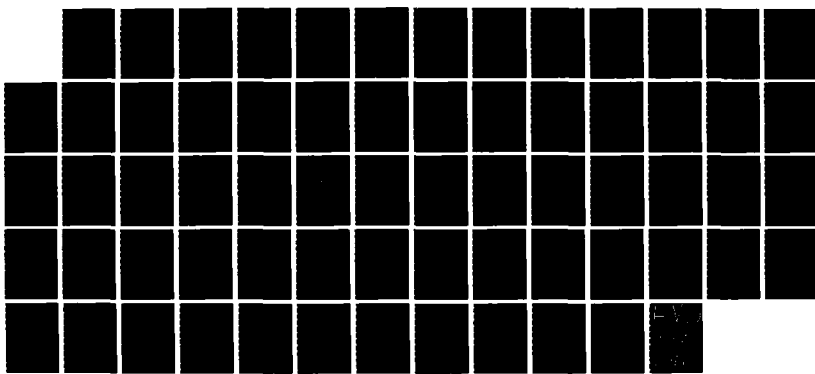
A NUMERICAL SIMULATION OF THE MEI-YU FRONT AND THE  
ASSOCIATED LOW-LEVEL JET(U) NAVAL POSTGRADUATE SCHOOL  
MONTEREY CA L C CHOU SEP 86

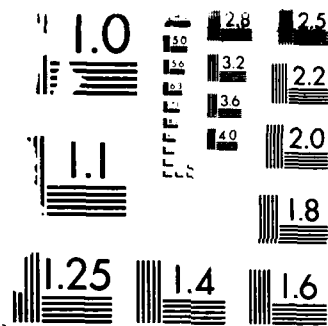
2/2

UNCLASSIFIED

F/G 4/2

NL





1000 dpi RESOLUTION TEST CHART

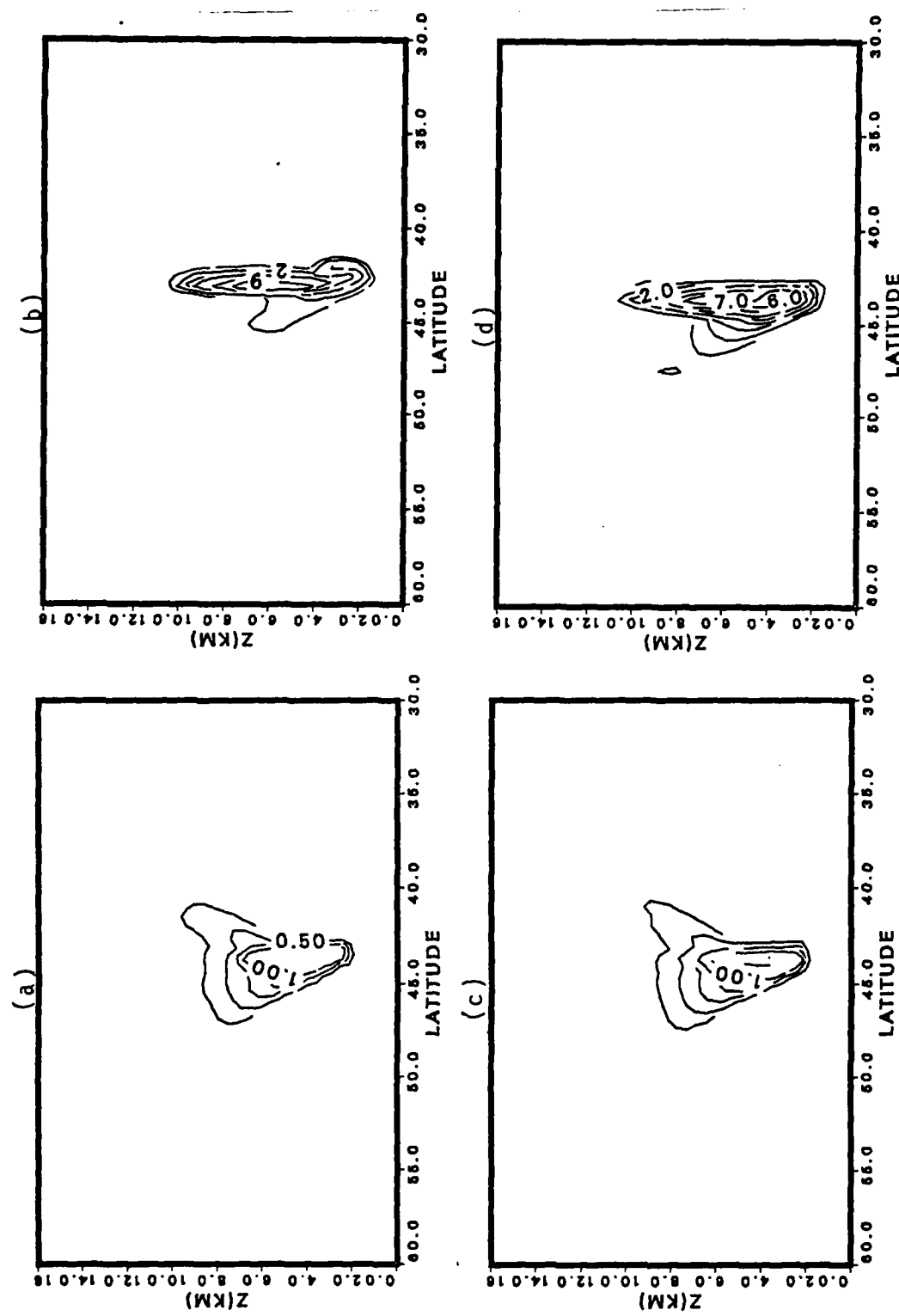


Fig. 3.14 Cross-section of total heating rate for midlatitude cases in units of  $^{\circ}\text{K Day}^{-1}$ , (a) M60, (b) M61 and (c) M90 (d) M91.

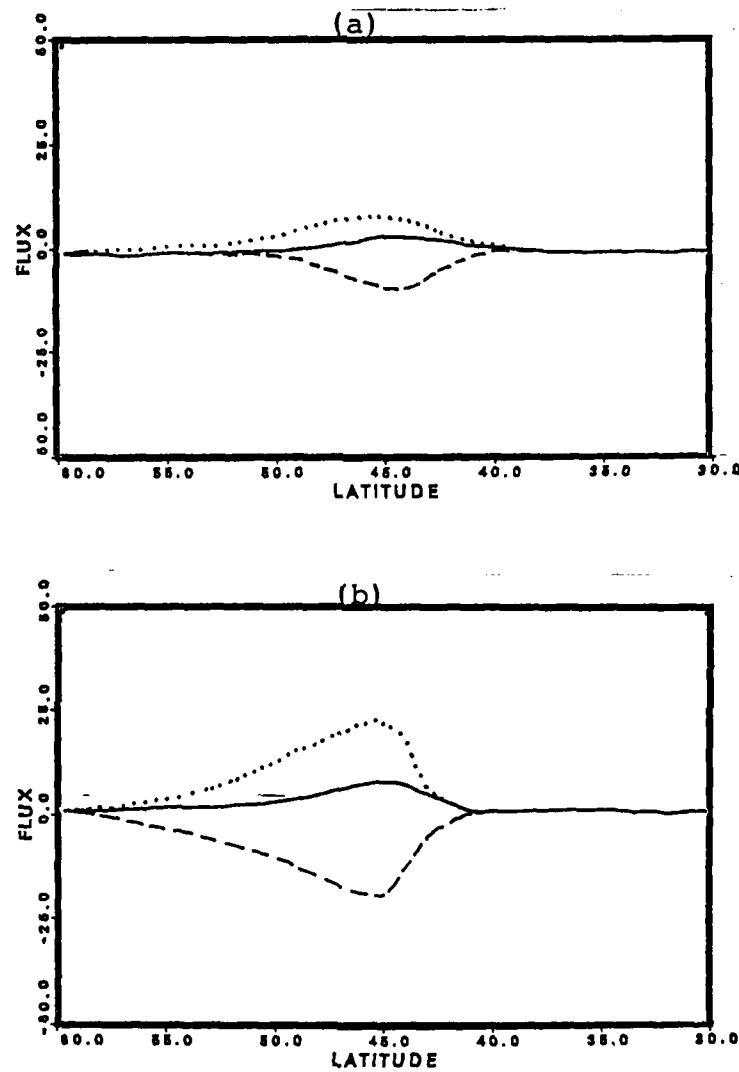


Fig. 3.15 Surface fluxes of momentum (dash;  $-10^{-4} \text{ m cb s}^{-2}$ ), sensible heat (solid;  $-10^{-4} \text{ }^{\circ}\text{K cb s}^{-1}$ ) and latent heat (dot;  $-10^{-4} \text{ }^{\circ}\text{K cb s}^{-1}$ ). (a) M61 and (b) M91.

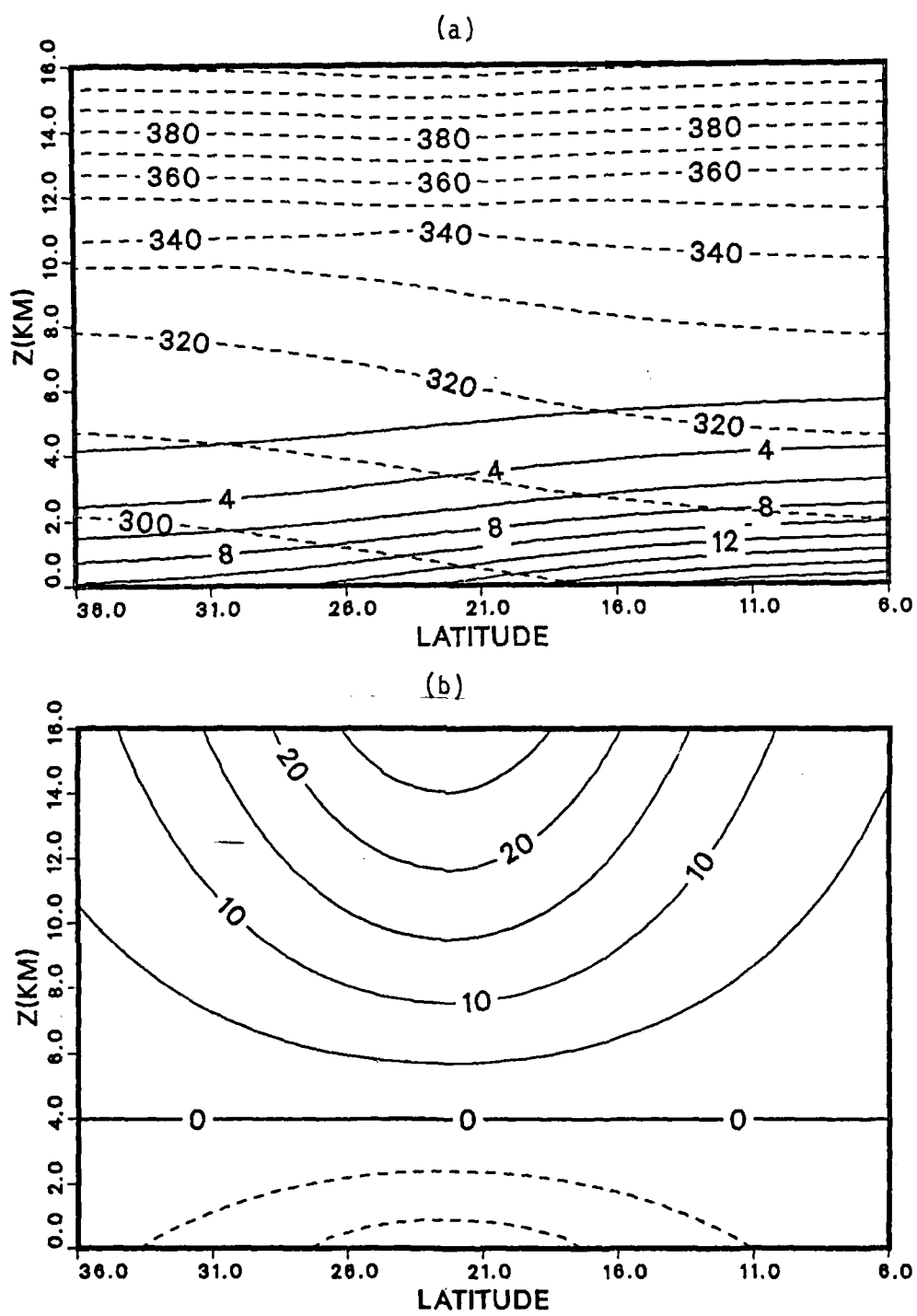


Fig. 3.16 As in Fig. 3.2, except for typical subtropical case, S90.

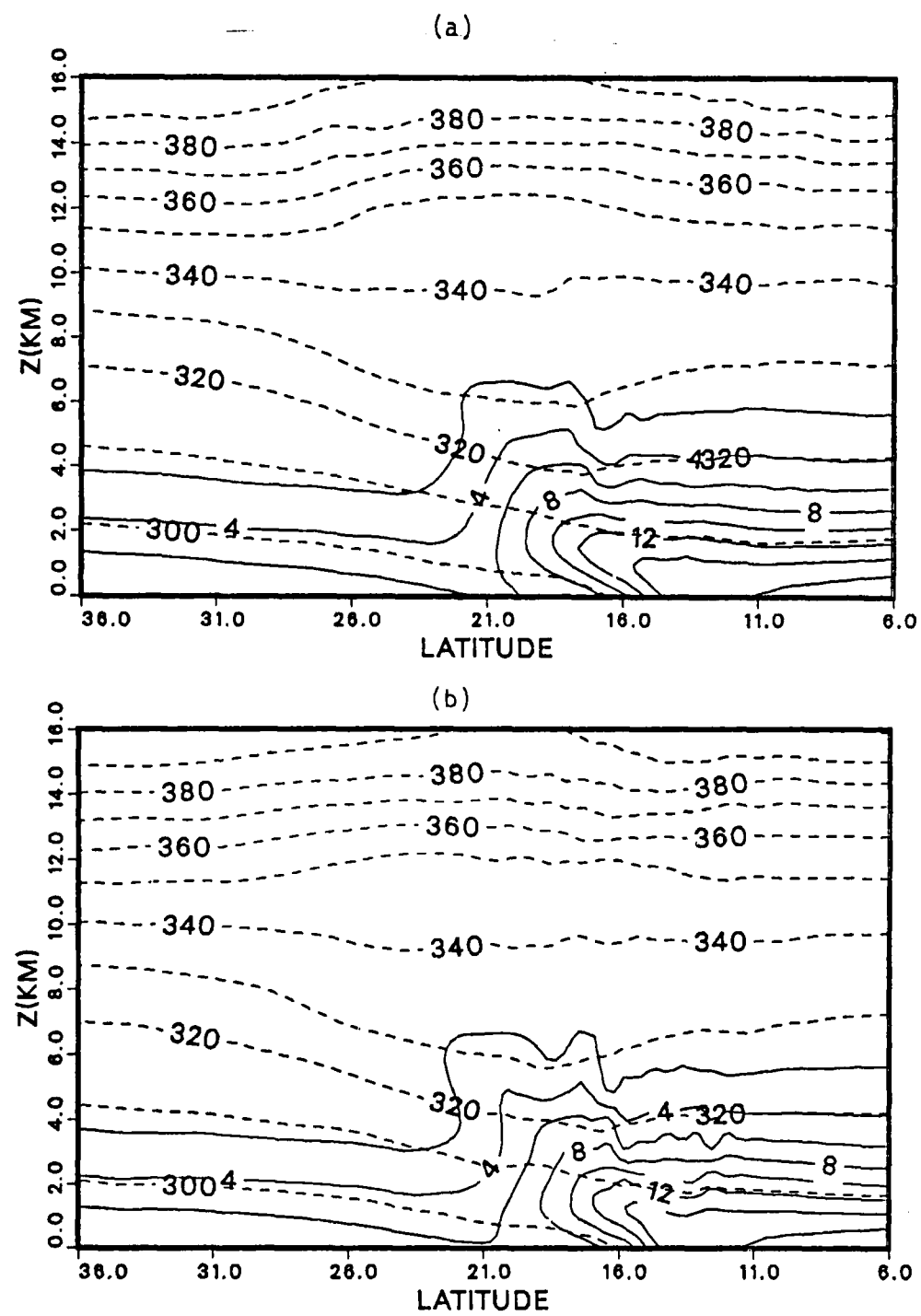


Fig. 3.17 As in Fig. 3.3, except for typical subtropical case, S90,  
 (a) day 4; (b) day 5.

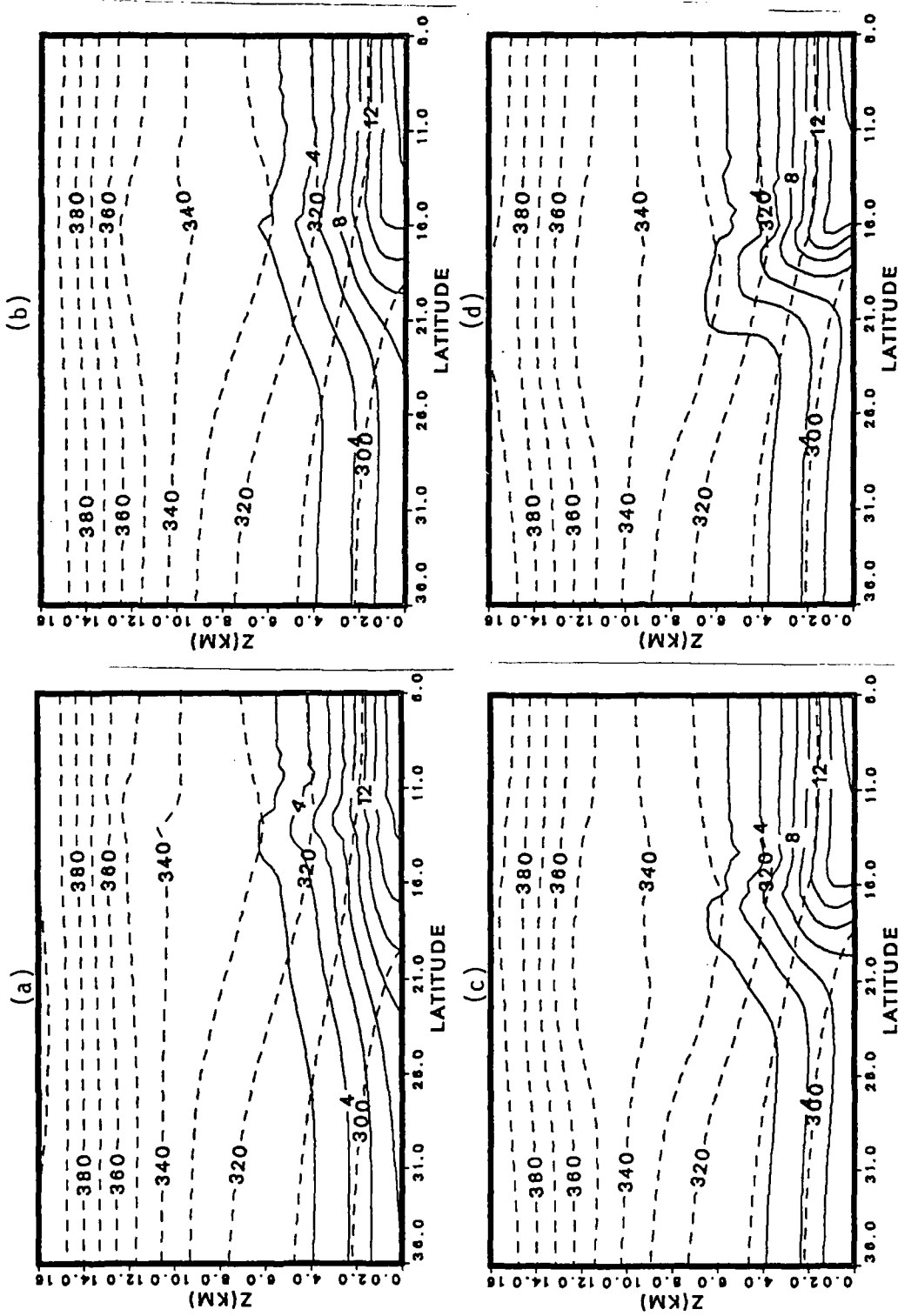


Fig. 3.18 Cross section of 24-hour averaged mixing ratio (solid),  $q(\text{g kg}^{-1})$ , and potential temperature (dash-dot),  $\theta(\text{°K})$ , for (a) day 2.0, (b) day 3.0, (c) day 4.0, and (d) day 5.0.

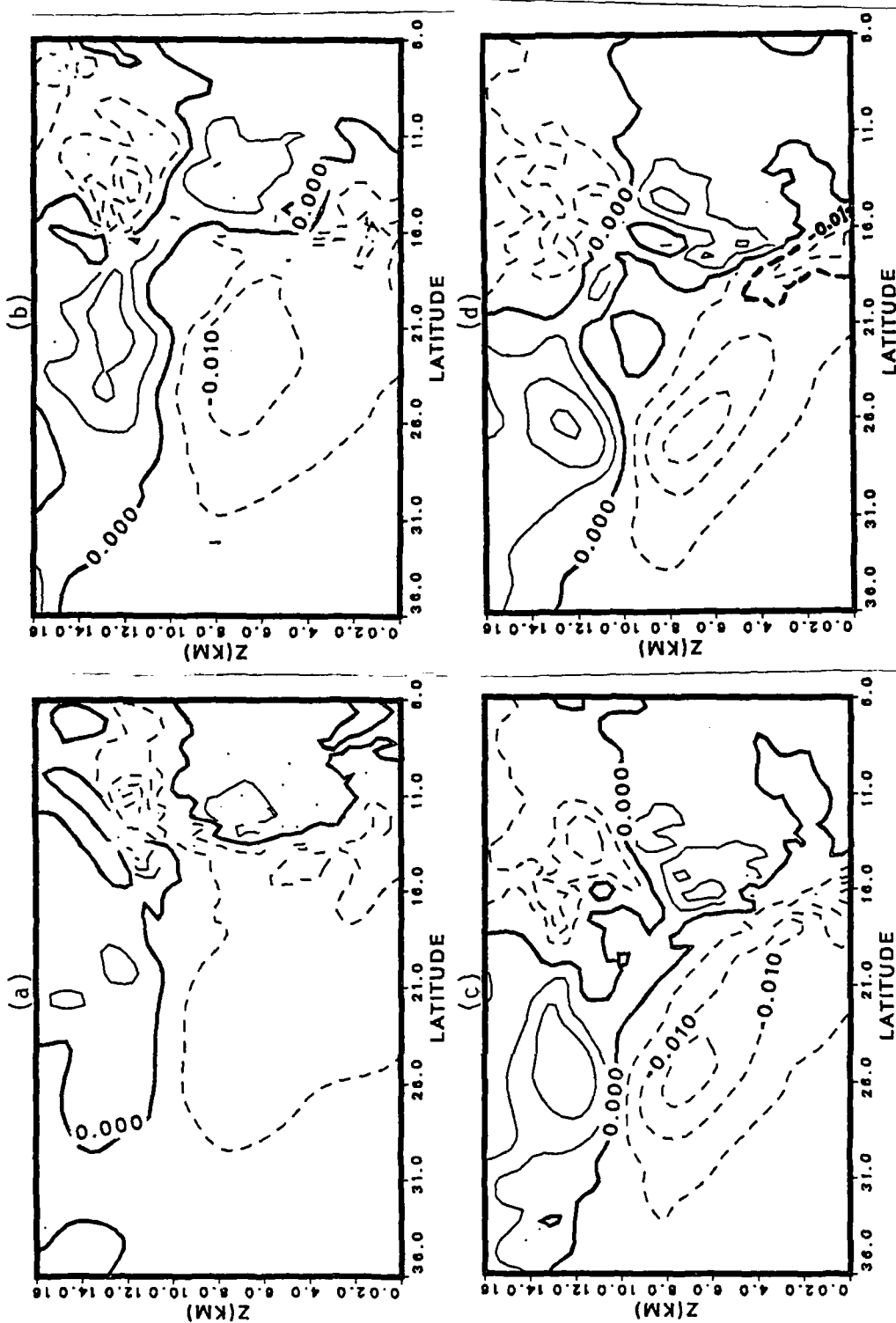


Fig. 3.19 As in Fig. 3.15, except for horizontal potential temperature,  $\partial \theta / \partial y (\text{°K km}^{-1})$ . Heavy dash line at day 5.0, ( $-0.01 \text{°K km}^{-1}$ ) indicate frontal zone.

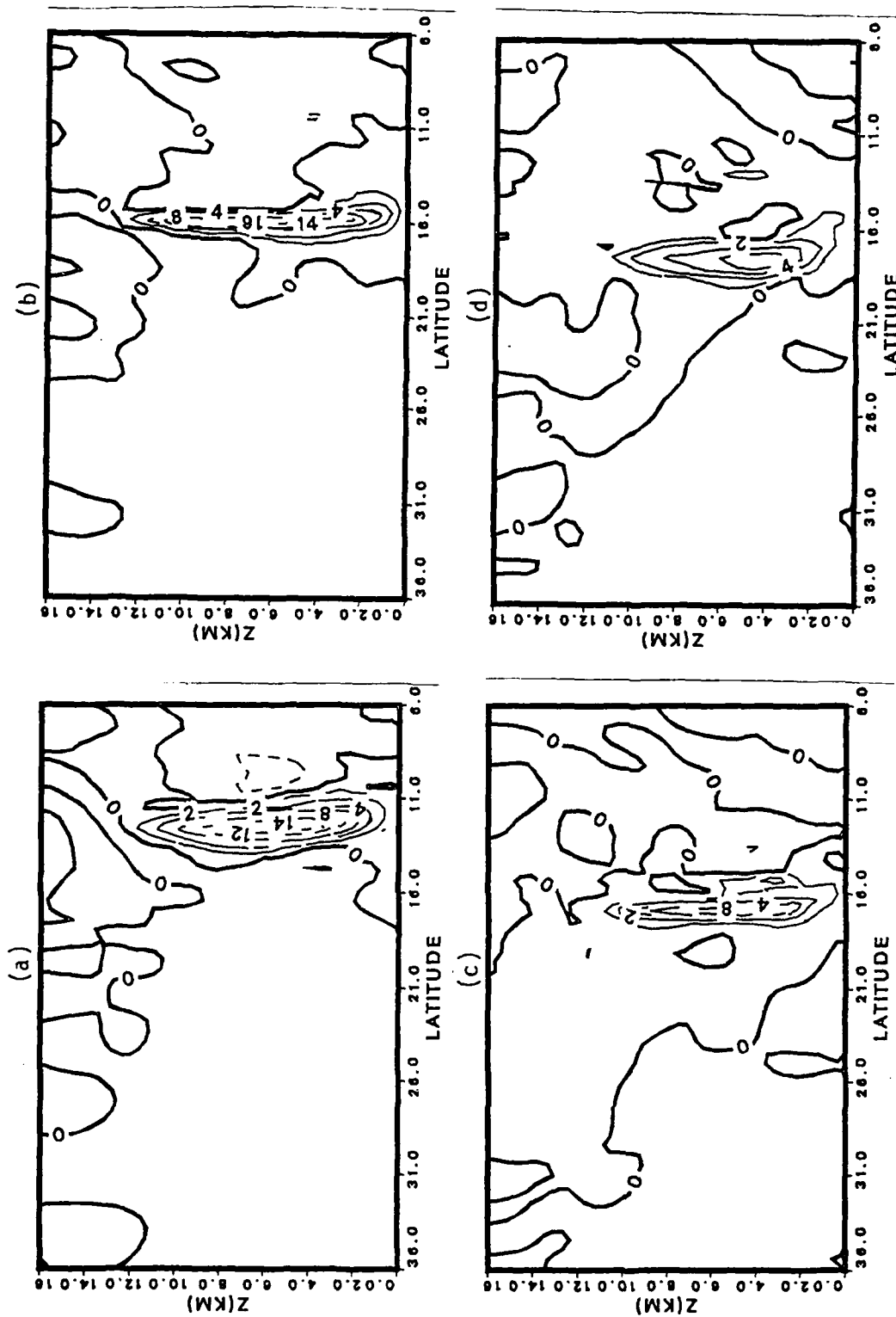


Fig. 3.20 As in Fig. 3.15, except for vertical pressure velocity,  $-\omega$  ( $10^{-4}$   $\text{cm s}^{-1}$ ).

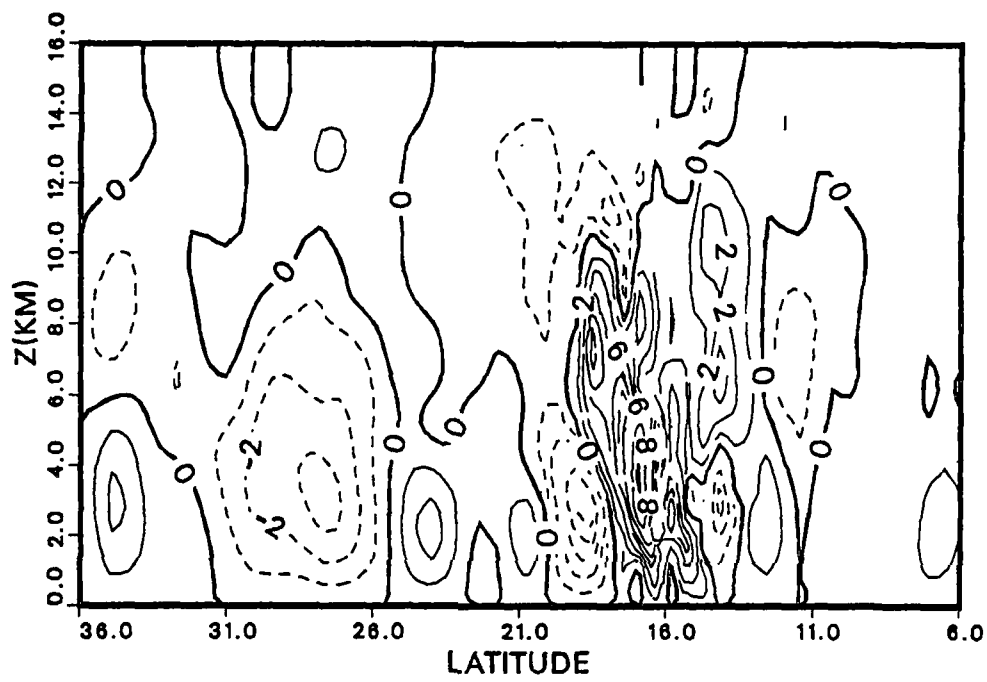


Fig. 3.21 Cross section of vertical pressure velocity,  $-\omega (10^{-4} \text{ cb s}^{-1})$ , at day 4.5 for case S90.

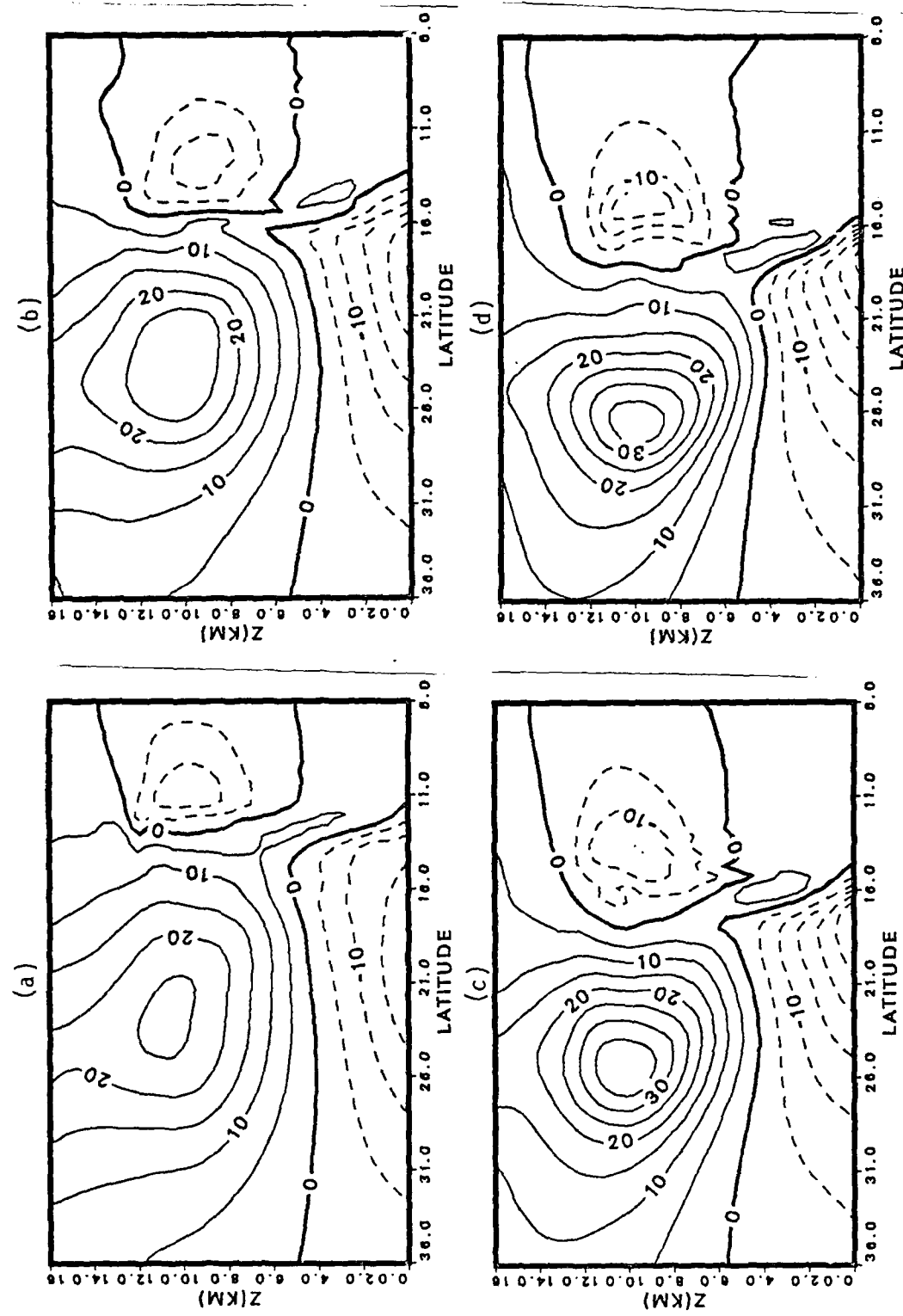


Fig. 3.22 As in Fig. 3.15, except for zonal wind speed,  $U(\text{m s}^{-1})$ .

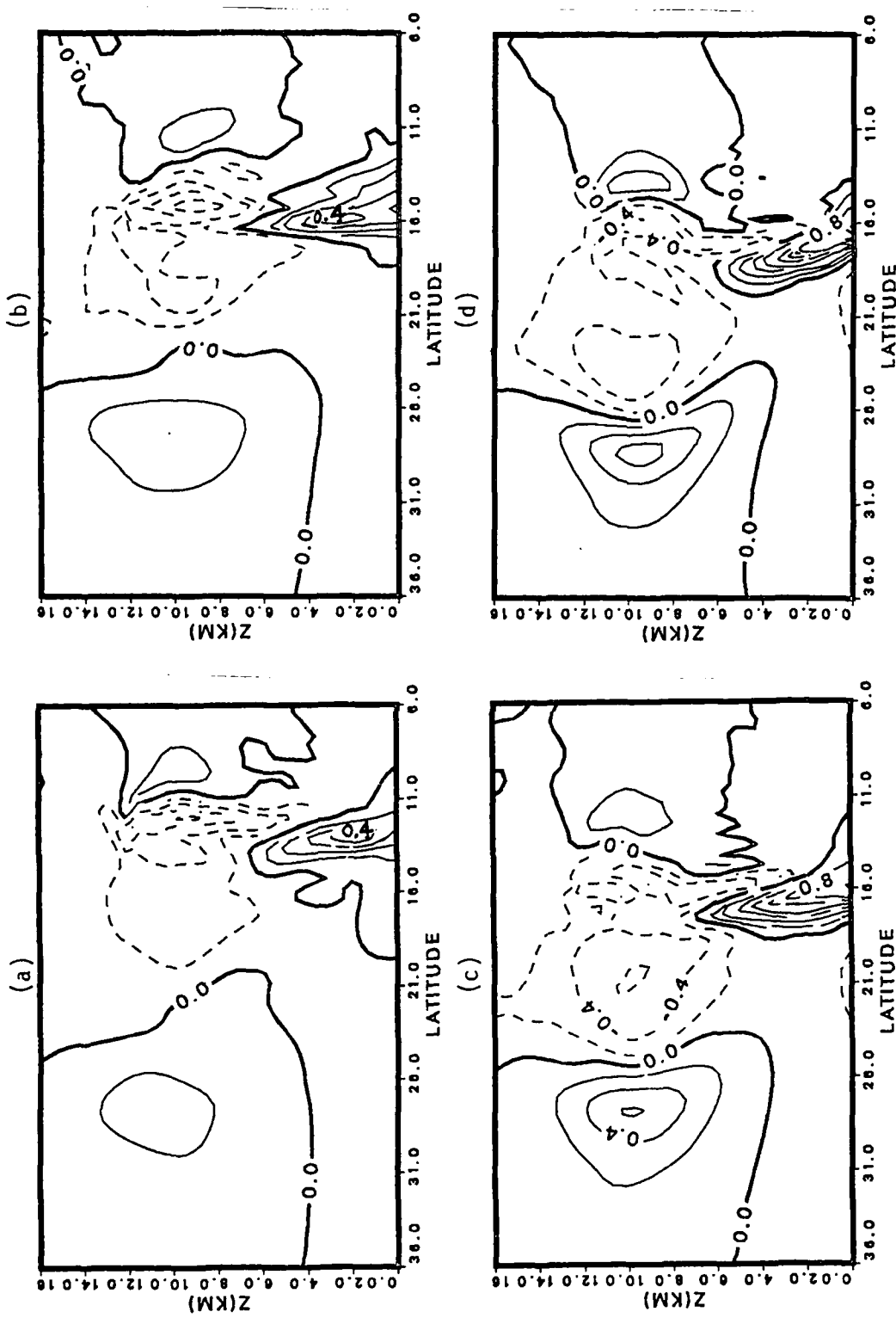


Fig. 3.23 As in Fig. 3.15, except for vorticity,  $\xi (10^{-4} \text{ s}^{-1})$ .

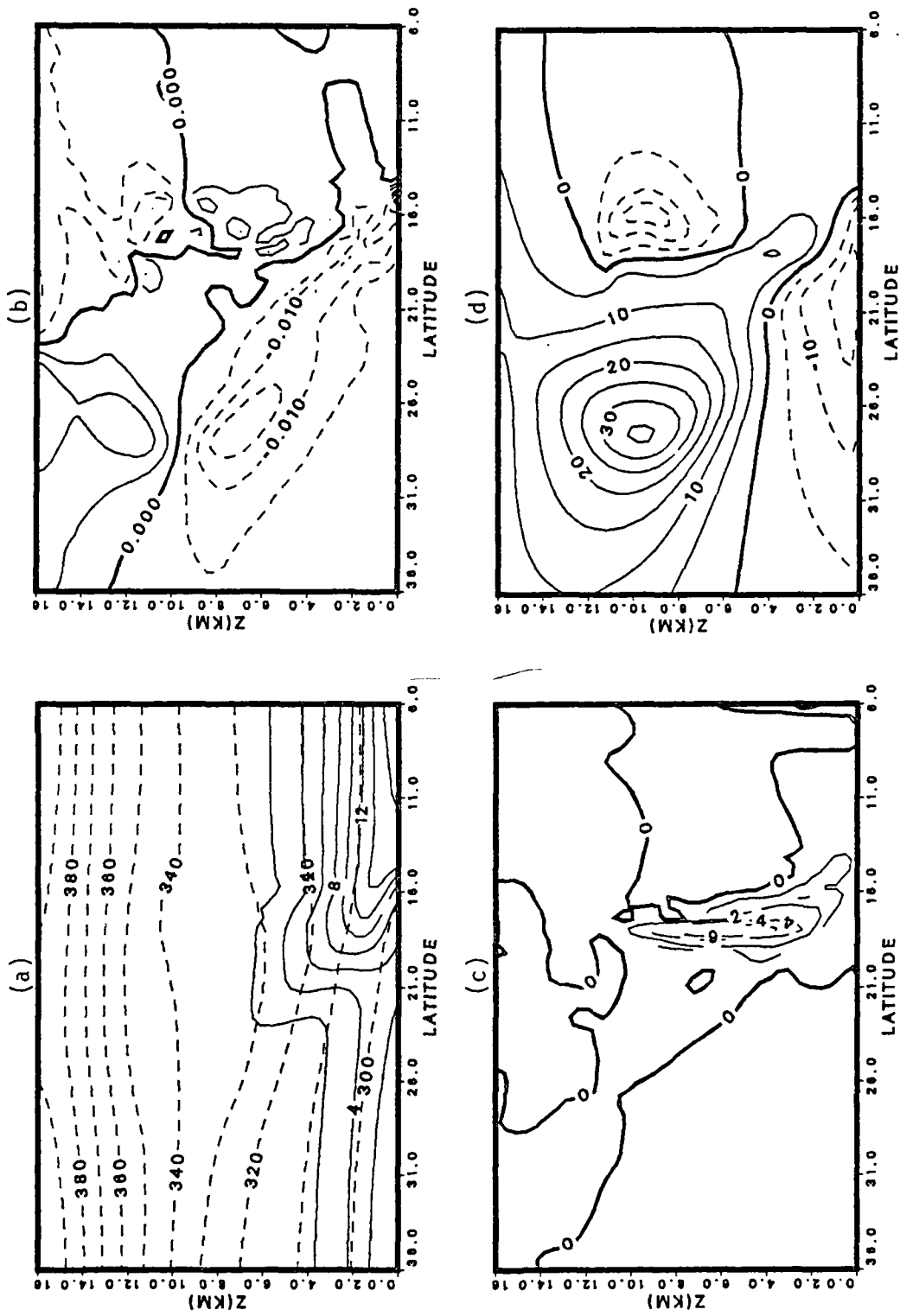


Fig. 3.24 Cross section of 24-hour averaged (a) mixing ratio (solid),  $q(\text{g kg}^{-1})$ , and potential temperature (dash),  $\theta(\text{K})$ , (b) horizontal potential temperature gradient,  $\partial\theta/\partial y(\text{K km}^{-1})$ , (c) vertical pressure velocity,  $-\omega(10^{-4} \text{ cb s}^{-1})$ , and (d) zonal wind speed,  $U(\text{m s}^{-1})$  at day 5.0 for the typical subtropical case, S90, integrated for 5 days from the 5-day averaged fields as initial conditions.

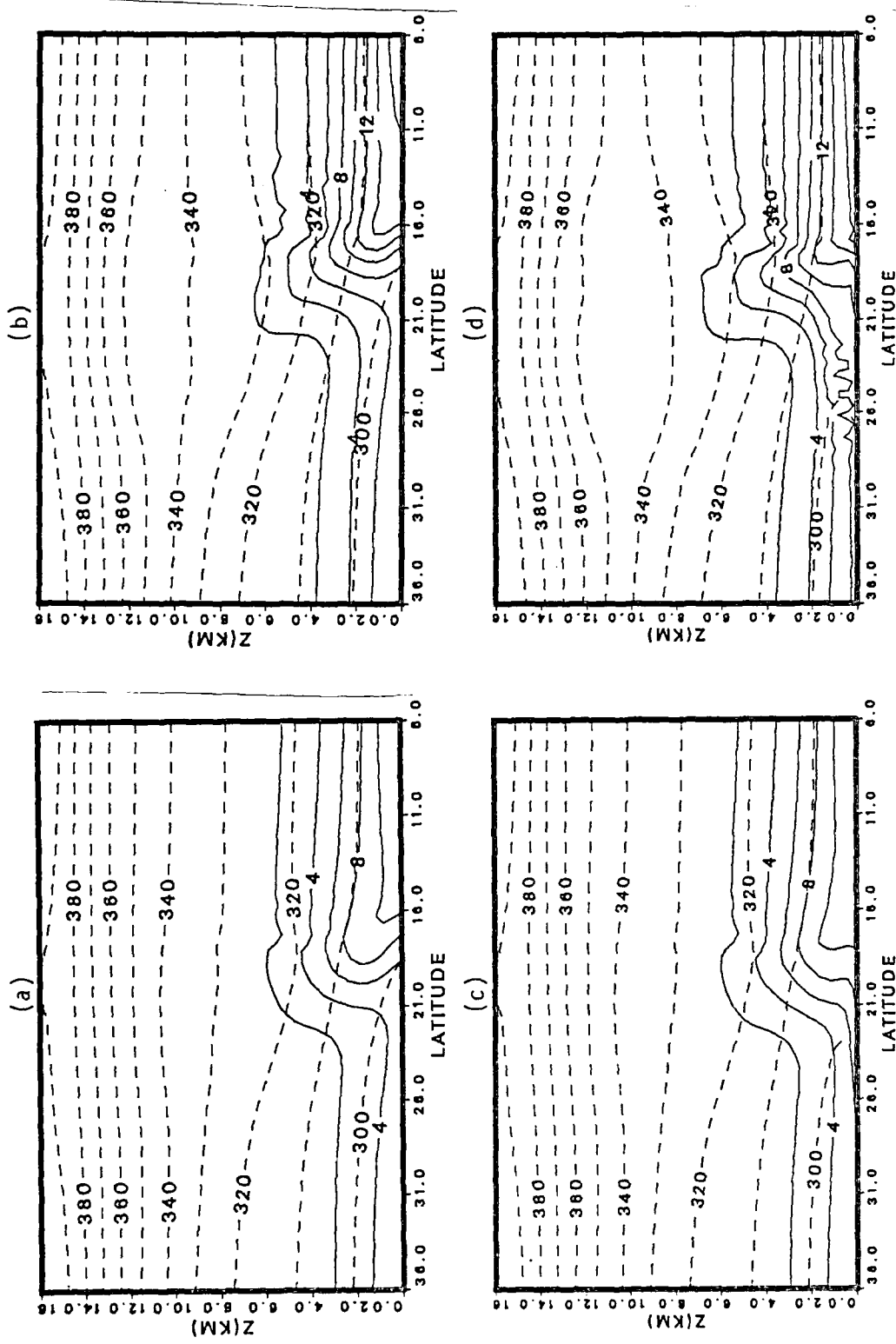


Fig. 3.25 Cross section of 24-hour averaged mixing ratio (solid),  $q(g\text{ kg}^{-1})$ , and potential temperature (dash),  $\theta(\text{K})$ , for different subtropical cases (a) S60, (b) S90, (c) S61 and (d) S91.

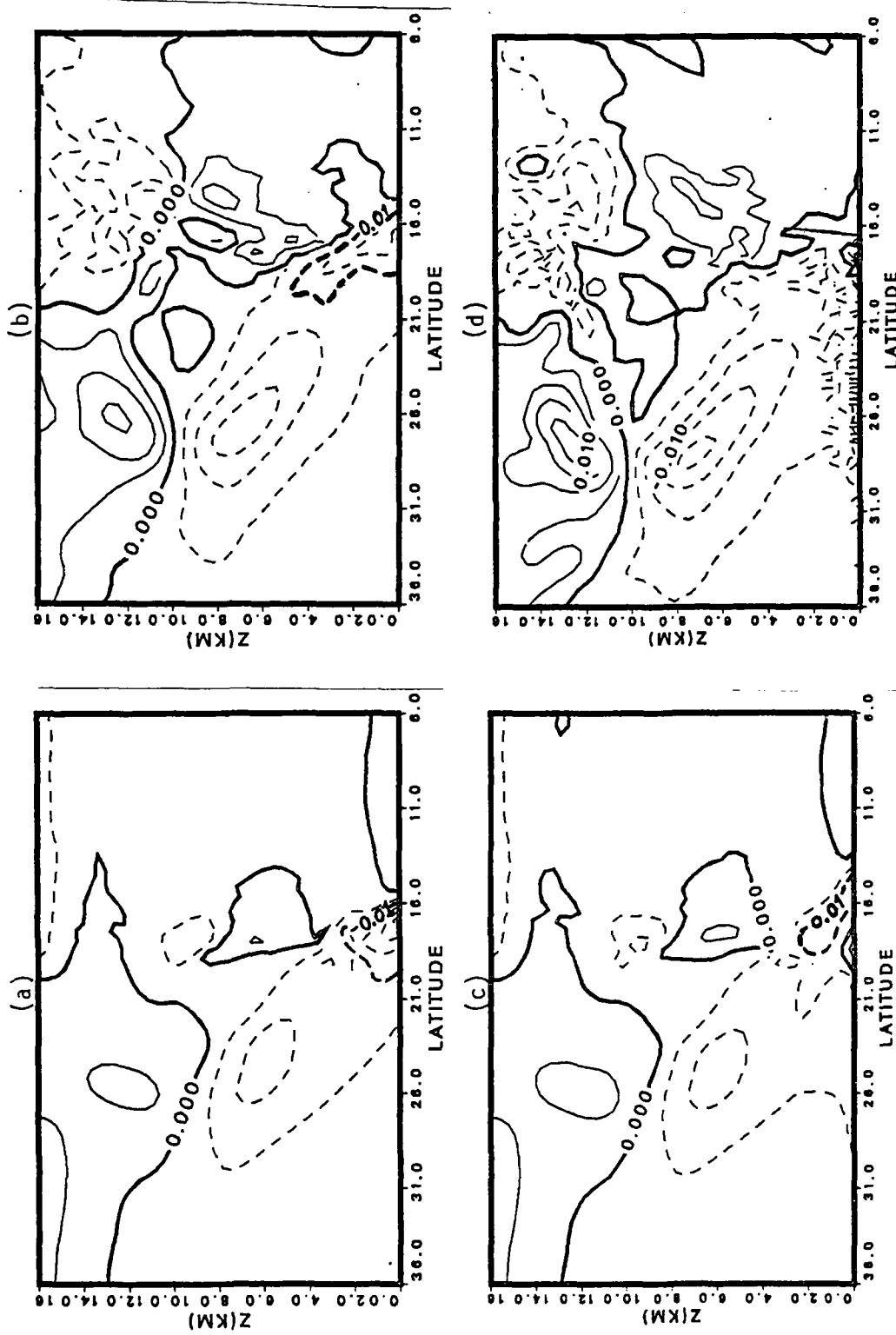


Fig. 3.26 As in Fig. 3.22, except for horizontal potential temperature gradient,  $\frac{\partial \theta}{\partial y}$  ( $^{\circ}\text{K km}^{-1}$ ). Heavy dash lines ( $-0.01^{\circ}\text{K km}^{-1}$ ) indicate frontal zone.

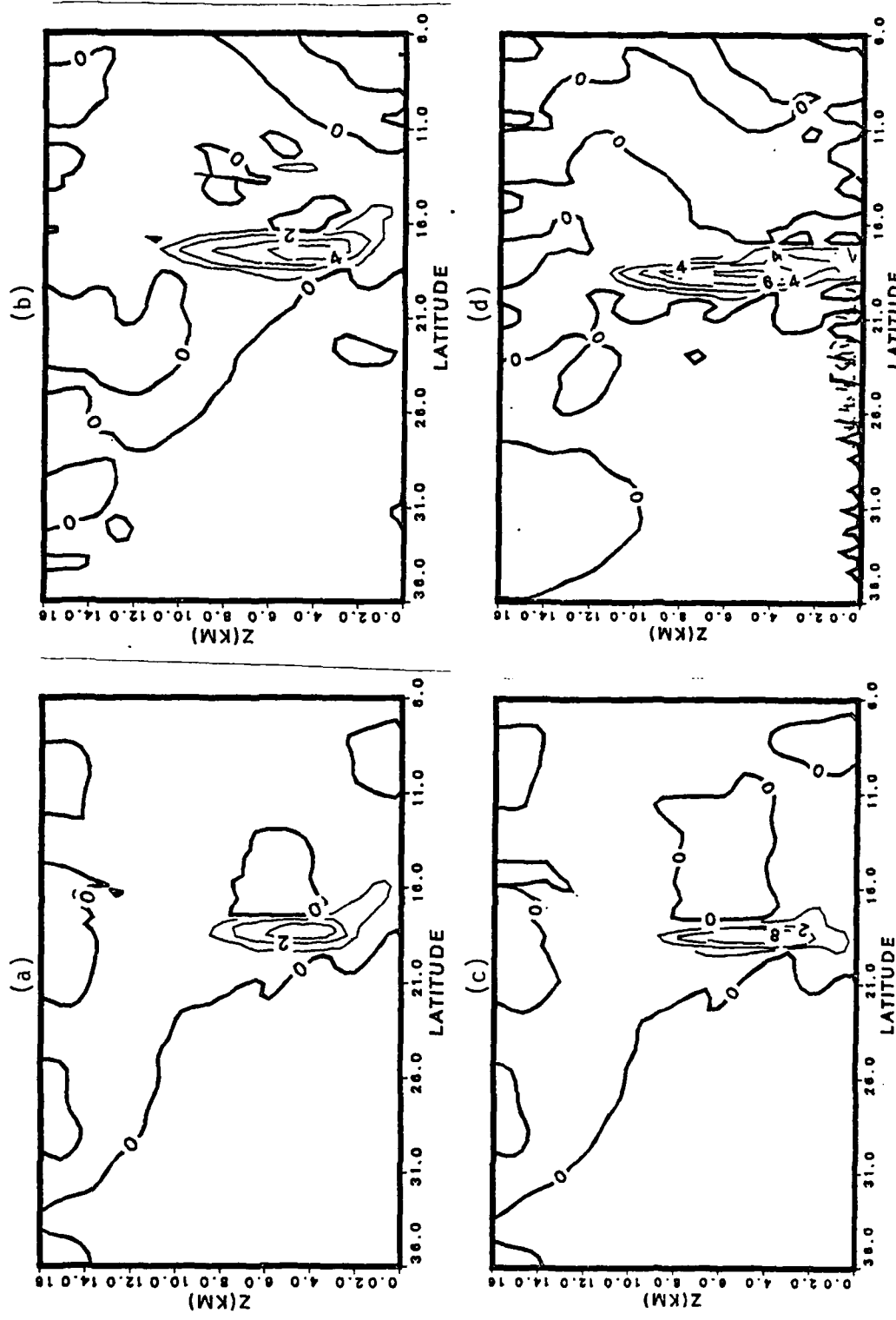


Fig. 3.27 As in Fig. 3.22, except for vertical pressure velocity,  $-\omega(10^{-4} \text{ cb s}^{-1})$ .

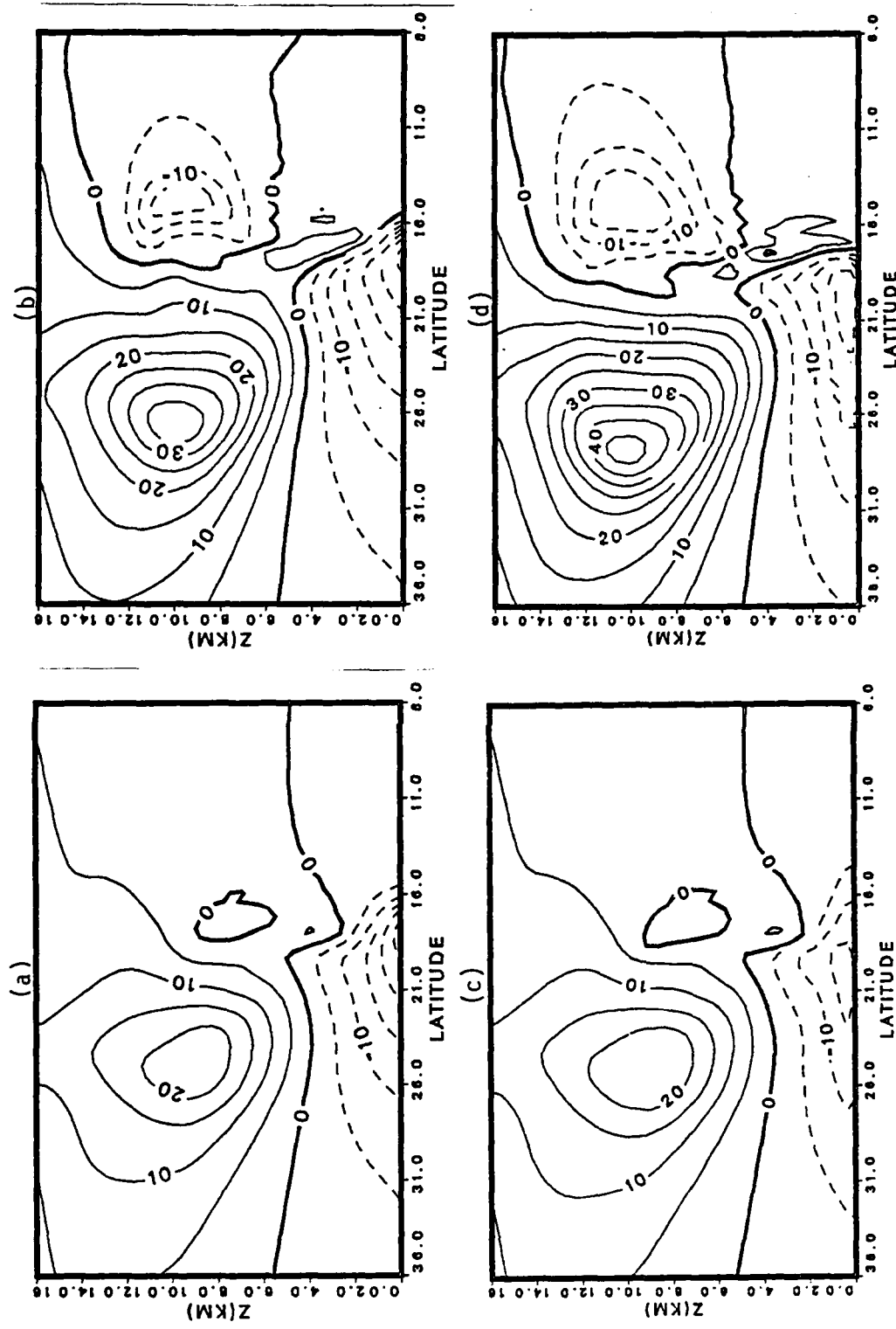


Fig. 3.28 As in Fig. 3.22, except for zonal wind speed,  $U(\text{m s}^{-1})$ .

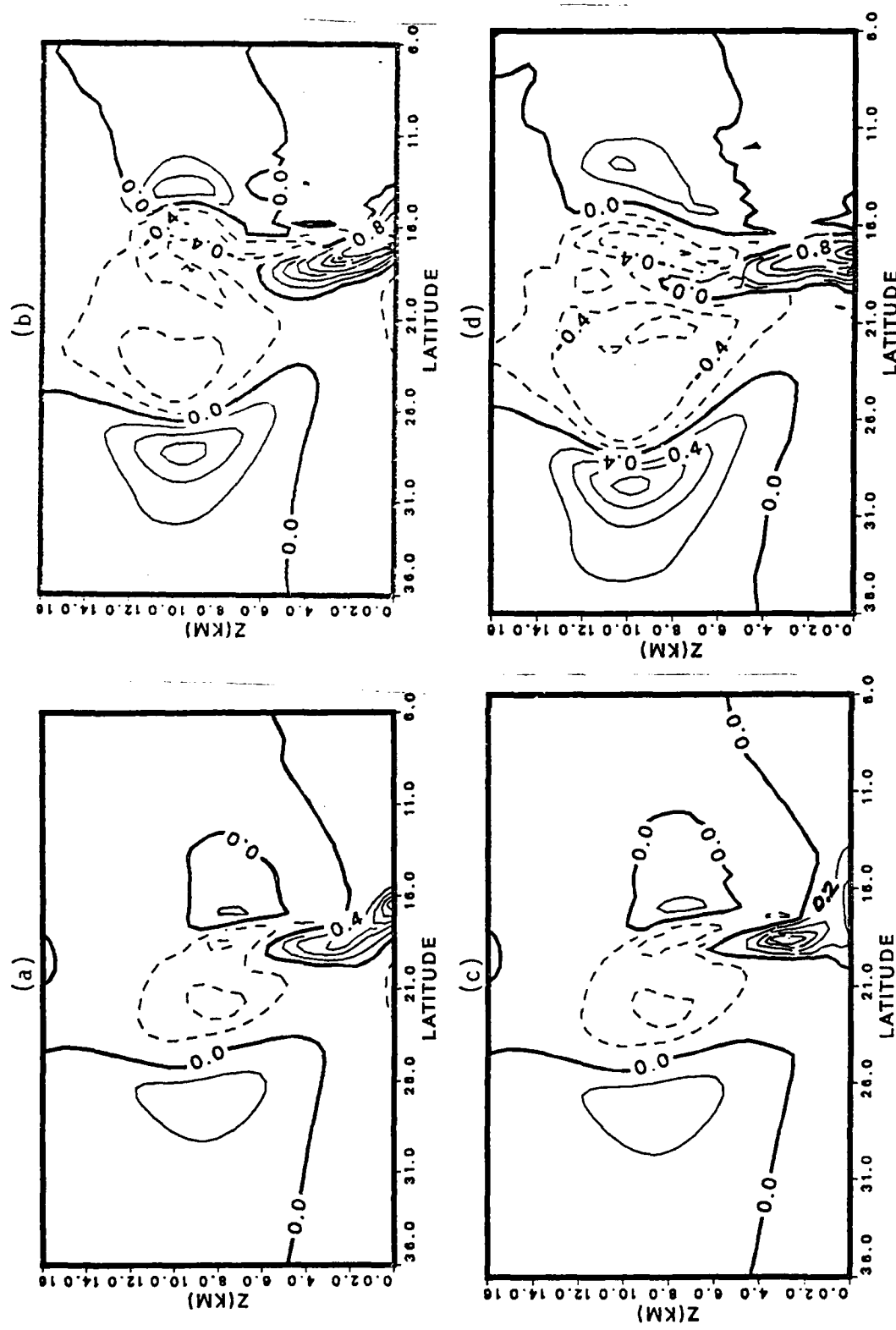


Fig. 3.29 As in Fig. 3.22, except for vorticity,  $\zeta(10^{-4} \text{ s}^{-1})$ .

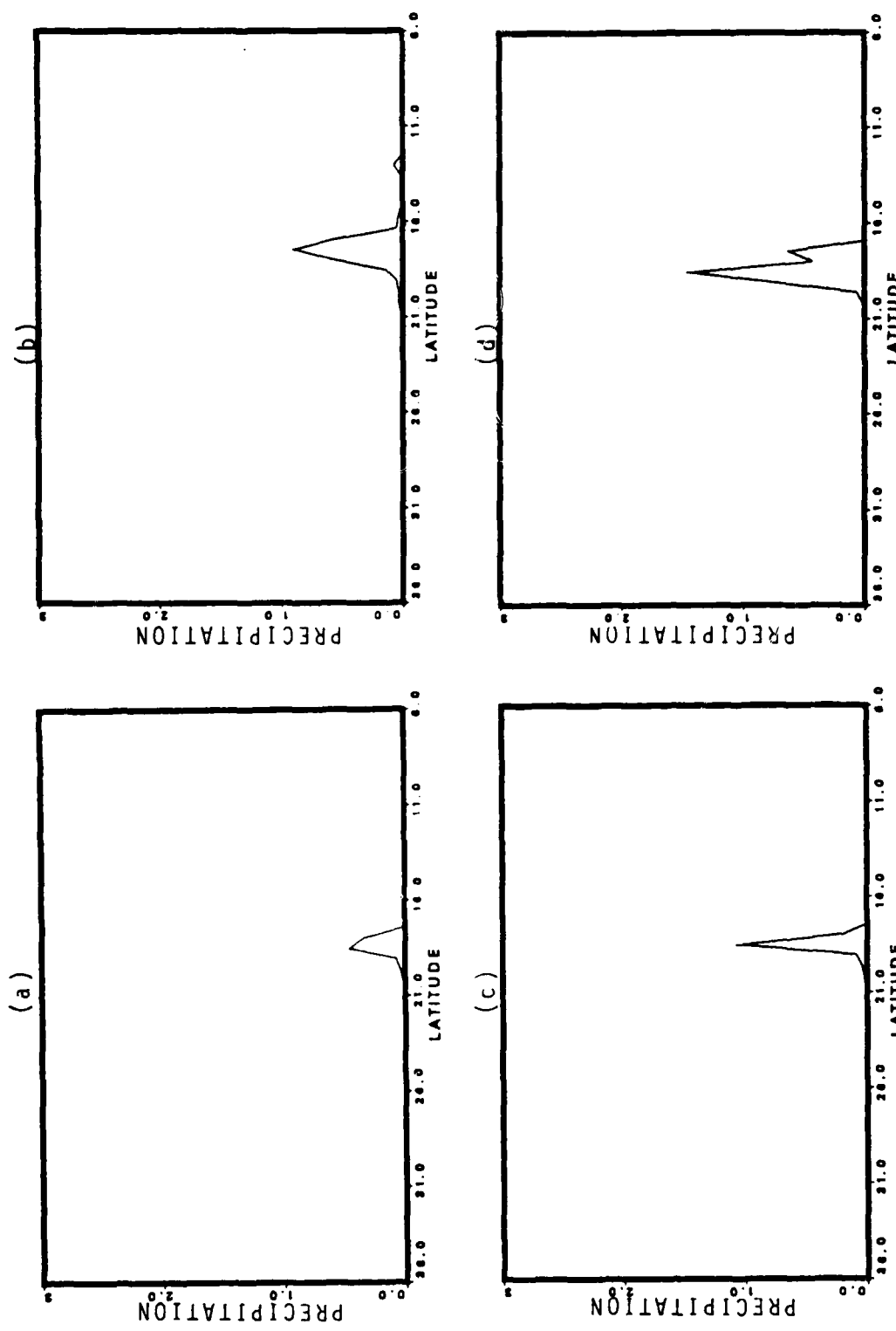


Fig. 3.30 Precipitation rate for subtropical cases in units of cm day<sup>-1</sup>, (a) S60, (b) S61, (c) S90 and (d) S91.

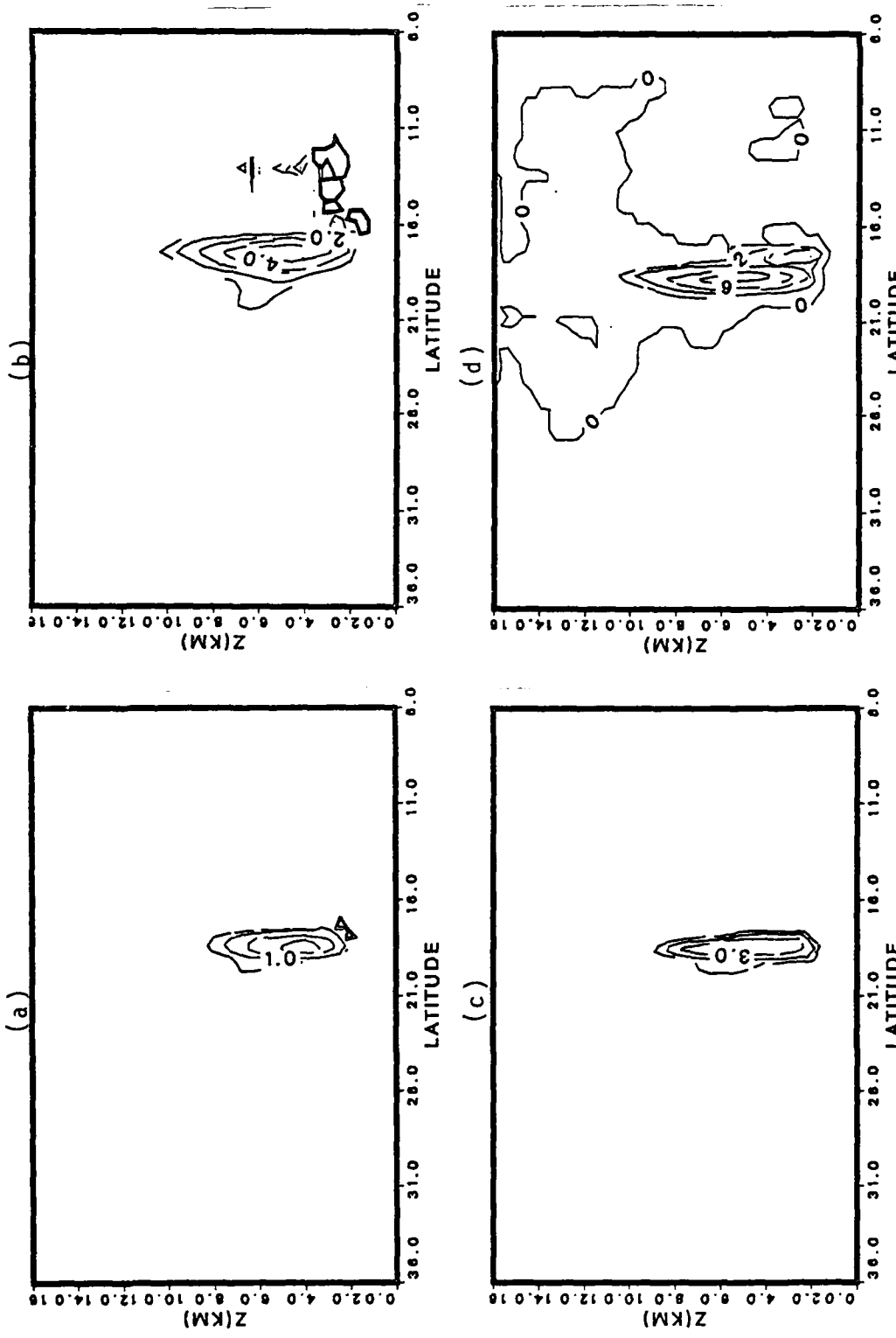


Fig. 3.31 Cross-section of total heating rate for subtropical cases in units of degree day<sup>-1</sup>, (a) S60, (b) S90 (c) S61 and (d) S91.

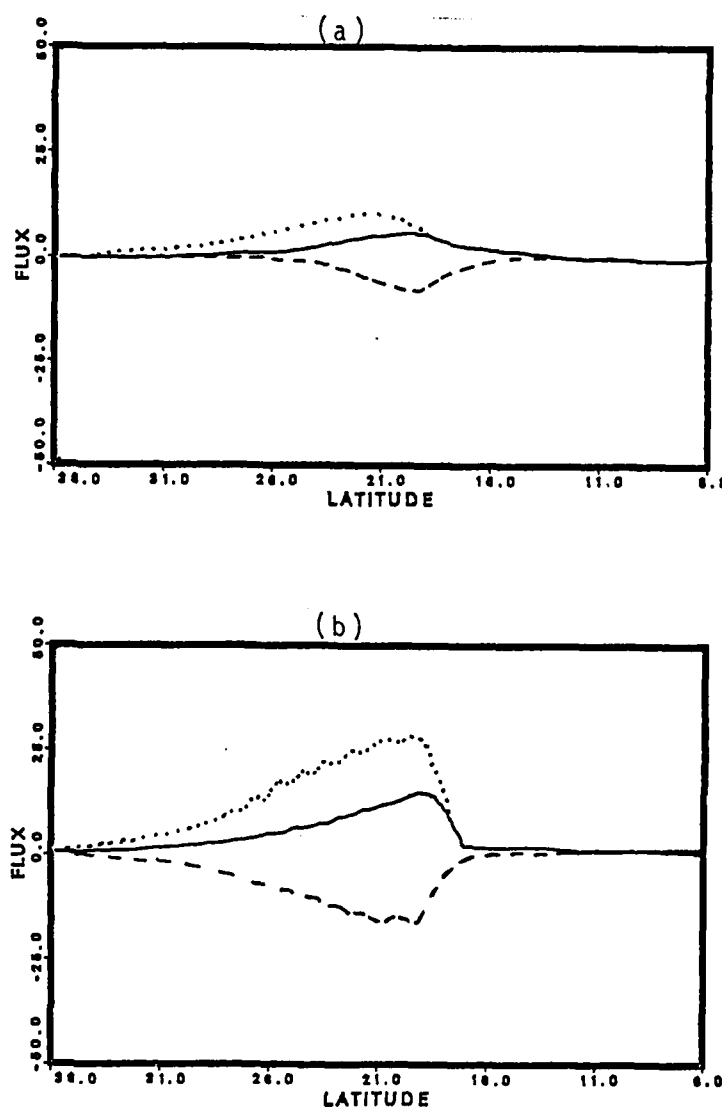


Fig. 3.32 Surface fluxes of momentum (dash;  $-10^{-4}$  m cb s $^{-2}$ ), sensible heat (solid;  $-10^{-4}$  °K cb s $^{-1}$ ) and latent heat (dot;  $-10^{-4}$  °K cb s $^{-1}$ ). (a) S61 and (b) S91.

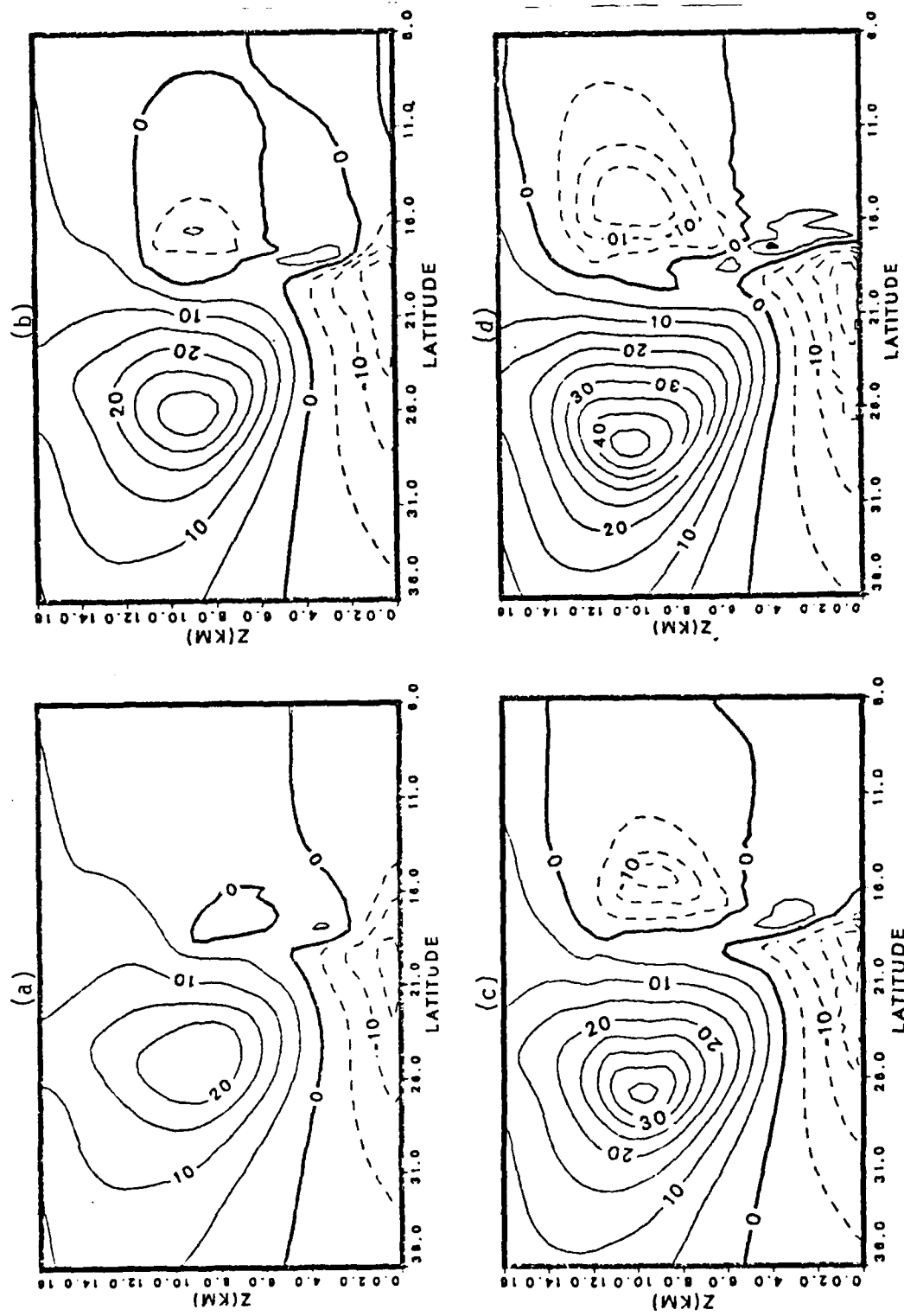


Fig. 3.33 Cross-section of 24-hour averaged zonal wind speed,  $U(m s^{-1})$ , for different subtropical cases (a) S61, (b) S71, (c) S81 and (d) S91.

#### IV. MECHANISM FOR THE LOW LEVEL JET (LLJ)

The previous section shows that a low-level westerly regime tends to develop in the frontal zone due to the intensifying meridional temperature gradient in the lowest few kilometers. In many of the subtropical cases this low-level westerly regime actually develops into a low-level jet whose height of 2-4 km is in good agreement with the levels (800-600 mb) of the observed low-level jet (Chen, 1977; 1978). The jet maximum of 10-15 m/s in these subtropical cases is also in reasonable agreement with observations.

In the Introduction, it was pointed out that there are several theories for the development of the low-level jet (LLJ). Since effects of terrain (Holton, 1967; Wexler, 1961) and diurnal cycles (Blackadar, 1957) are not included in the model, the related boundary-layer theories cannot be treated in this study. Neither can the theory of the downward transport of momentum by cumulus convection (Masomoto and Ninomiya, 1969; Ninomiya, 1971), because the convective adjustment used in the present model does not include the parameterization of cumulus momentum transport.

The theory proposed by Uccellini and Johnson (1979) in the study of midlatitude severe storms over the U. S. is based on a wind-mass adjustment, whereby the secondary

circulation forced by an upper level jet streak causes a vertical coupling, which leads to the development of a LLJ. In this mechanism, the LLJ will develop beneath the upper level jet streak such that the two jets will be aligned vertically and the axes will be perpendicular to each other. Although the model-produced low-level westerly maximum often appears (especially in the midlatitude cases) as a downward extension of the upper tropospheric westerly jet, the upper level jet is always situated much too poleward of the LLJ core for wind-mass adjustment mechanism to be effective.

In the present study, the LLJ in the subtropical experiments is much better defined than in the midlatitude experiments. Furthermore, in all cases when the vertical motion is enhanced due to increased relative humidity (therefore also enhanced conditional instability) and/or surface fluxes, the low-level westerlies become stronger. This is also true with the development of the upper level easterlies equatorward of the front, which also appears with small magnitudes in the midlatitude experiments with higher relative humidity. In all subtropical experiments, these upper-level easterlies expand and dominate most of the upper troposphere equatorward of the front. These results suggest that when the vertical motion above frontal zone is intense, a "reversed Hadley cell" exists equatorward

of the front, with rising motion in the frontal region and sinking motion further equatorward. Such an overturning would provide an easterly Coriolis torque at the upper-level equatorward flow and a westerly Coriolis torque at the lower-level poleward flow, which may explain the upper-level easterlies and the low-level westerly jet. Indirect evidence of the "reversed Hadley cell" to the south of LLJ may be found in an observational study by Ninomiya and Akiyama (1974). They found that moist air is located above the LLJ in the middle and upper troposphere, but the air south of the LLJ is fairly dry throughout the whole troposphere. This is indicative of a large-scale subsidence south of the front.

More evidence of this "reversed Hadley cell" is seen in the temperature distribution of all cases in which strong cumulus convection is indicated. For example, the temperature in Fig. 3.18 (S90 - the typical subtropical case) increases equatorward throughout the troposphere for the first day. Afterward, reversed meridional temperature gradients begin to appear in the tropical region, such that by day 5 the maximum temperature at any level in the middle-upper troposphere is near the frontal zone. This situation is also apparent in Fig. 3.25 for all subtropical cases. The reversed temperature gradient to the south of the maximum upward motion has been

observed both in the Mei-Yu front (Chen and Chang, 1980) and in the Baiu front (Matsumoto et al., 1970; Ninomiya and Akiyama, 1970). Therefore, the equator-side "reserved Hadley cell" is actually thermally direct, with warm air rising in the frontal zone and cool air sinking equatorward. Hence, this circulation can be maintained and as well as continue to provide the upper-level easterly and lower-level westerly accelerations.

The next question concerns the identification of the main mechanism(s) for this equatorward overturning. There appears to be three possible mechanisms:

- 1) The secondary circulation normally associated with the large-scale flow of a front;
- 2) The cumulus convection due to the conditional instability, which can increase the latent heat release and force an enhanced secondary circulation;
- 3) The third possibility is based on the observation that the vertical velocity field of several of the more intense cases exhibits a multi-band structure. Each of the rising branches is upright, and is stacked in a poleward slanting configuration. In a way this structure resembles the "slantwise convection" associated with symmetric instability in a baroclinic atmosphere

(e.g., Emanuel, 1985). This slantwise convection may also be a relevant mechanism.

To differentiate the last two mechanisms, the term "upright convection" will be used to describe the basically single-band, vertically-oriented convection which is normally associated with conditional instability, and "slantwise convection" will be used to describe the slanted and stacked multi-band structure which resembles the convection predicted by the symmetric instability theory. Fig. 4.1 illustrates schematically the differences among the three mechanisms.

The meridional-vertical streamfunction is shown in Figs. 4.2 and 4.3, for the midlatitude and subtropical cases, respectively. For the midlatitude R.H.=60% cases (M60 and M61), the atmosphere remains statically stable, and Figs. 4.2a,c indicate that the large-scale frontal secondary circulation consists of a single cell in the Hadley sense. When R.H.=90%, the initial sounding of the midlatitude cases (M90 and M91) is conditionally unstable in the lower latitudes. At day 4, both cases show a small and very weak "reversed Hadley cell" in the middle troposphere equatorward of the front. Apparently this cell is responsible for the small region of upper level easterlies equatorward of the front. However, the modest cumulus convection through the release of conditional

instability is not intense enough to force a strong reversed Hadley cell that can develop a strong LLJ.

All the subtropical cases are initially conditionally unstable. A larger and stronger "reversed Hadley cell" is present in all cases (Fig. 4.3). This cell is situated poleward and is more vertically confined for the R.H.=60% case than for the R.H.=90% case with the middle-level rising motion occurring poleward of the surface front. This is the situation when the LLJ is either ill-defined (S60 case, Fig. 3.28a) or rather weak (S61, Fig. 28c). When R.H.=90%, the reversed Hadley cell is located more equatorward, is more intense and extends throughout the vertical domain (Figs. 4.3b,d). The LLJ is well-defined in this situation (Figs. 3.28b,d), and clearly coincides with the concentrated poleward flow at the lower branch of the reversed Hadley cell. The cumulus convection is the strongest in these cases and is apparently responsible for generating the intense equator-side meridional circulation which, in turn, leads to the development of the LLJ.

It is clear that the cross-frontal secondary circulation is different from the secondary circulation equatorward of the front, and therefore it can not induce the LLJ. However, the roles of upright convection and slantwise convection are not easy to distinguish. The slantwise convection structure is present in both

midlatitude (when the LLJ is not present) and subtropical (when the LLJ is developed) cases. The slanting is apparently related to the structure of the frontal surface. Although the frontal forcing cannot, by itself, directly cause the equatorward secondary circulation, it exerts a strong influence on the environmental conditions that affect convection. This may involve two mechanisms. The first is the large-scale lifting of moist air. This leads to either stable precipitation or a "CISK" (Conditional Instability of the Second Kind) type convection, where the low-level convergence is provided by the frontal forcing. The second involves the creation of conditions for symmetric instability. These conditions occur when the vertical gradient of equivalent potential temperature ( $\theta_e$ ) becomes negative along the surfaces of pseudo-angular momentum, which is defined by the following function (Emanuel, 1983a,b):

$$M = u + fy.$$

In a symmetrically unstable baroclinic atmosphere, slantwise convection occurs when there is a slantwise displacement of an air parcel along a constant  $M$  surface. Based on a diagnostic semi-geostrophic model, Emanuel (1985) further showed that even in the presence of small symmetric stability, frontal forcing can result in a strong, concentrated, sloping updraft which is located

ahead of the region of maximum geostrophic frontogenetical forcing. This possibility is supported by Sanders and Bosart (1985) who reported observations of a concentrated sloping updraft that resembles slant-wise convection in a mesoscale precipitation band. The sloping updraft remains even after the environment becomes symmetrically stabilized. Apparently the frontogenetical process can force the moist updraft along the sloped M-surfaces where narrow convective bands can develop. Thus, slantwise convection may be expected in areas of neutral or small symmetric stability when frontogenetical forcing is present.

The evolution of  $\theta_e$  and the M-function for the typical midlatitude and subtropical cases (M60 and S90) is shown in Figs. 4.4 and 4.5. In the midlatitude case, the frontogenetical area is statically stable initially and the M-surfaces tilt only slightly (Fig. 4.4a). As the frontogenetical process proceeds, the frontal structure develops and leads to a stronger tilt of the M-surfaces in the highly-baroclinic frontal zone. This results in an area of near-neutral symmetric instability after day 1, although the area is limited to the lowest troposphere. In the subtropical case, conditional instability is present throughout the domain initially (Fig. 4.5a). This condition continues until day 4 when the frontal structure is developed (Fig. 3.19) and the

frontal zone becomes stable in the upright convection sense. As a result of frontogenesis, the M-surfaces tilt more towards the cold air in the frontal zone. This increased tilt leads to a condition of symmetric instability in a relatively deep layer between the surface and 6 km in the frontal zone. As the convective instability is eliminated, a slantwise convection structure develops in the vertical motion field. It appears that this structure is produced by the frontogenesis forcing of moist updrafts along the sloped M-surfaces, similar to Sanders and Bosart's (1985) observations.

Distribution of day-5  $\theta_e$  and the M-function are presented in Figs. 4.6 and 4.7 for the midlatitude and subtropical experiments, respectively. In the R.H.=60% midlatitude cases (M60 and M61, Figs. 4.6a,c), static stability remains positive and the area favorable for slantwise convection is rather limited and is confined to the lowest 2 km in the frontal zone. Thus, the secondary circulation is almost entirely a result of the frontal forcing.

Distribution of  $\theta_e$  and the M-function are given in Figs. 4.6b,d for the R.H.=90% midlatitude cases (M90 and M91). In these cases, the equatorward side of the front is conditionally unstable while the poleward side is stable initially. It is interesting to note that in the

frontal zone the convective adjustment apparently has stabilized the atmosphere in the vertical direction. However, the  $\theta_e$  and M lines are nearly parallel in the frontal zone; and the area favorable for sloping updraft is much greater than that for the R.H.=60% cases. In this case, a low level maximum wind of 5 m/s actually develops near  $z=3$  km.

Similar to the R.H.=90% midlatitude cases, all the subtropical without-flux cases (Fig. 4.7a,b) have conditional unstable profiles equatorward of the front and a stable  $\theta_e$  profile poleward. In the with-flux cases (Fig. 4.7c,d), the conditional instability also exists in the poleward region, a result of the supply of moisture and heat at the surface. The frontal rising motion zones in all cases again have stable  $\theta_e$  profiles, but shows signs of even stronger symmetric instability in lower troposphere.

In the S60 case (Fig. 4.7a), there is a larger area of near neutral  $\theta_e$  profiles along the M-surfaces in the vicinity of the frontal rising motion. In the S61 case (Fig. 4.7c), the  $\theta_e$  profiles in the lower troposphere actually become unstable along the M surfaces in the rising motion zone. The same is true for the S90 and S91 cases (Figs. 4.7b,d), except the area of symmetric instability is even larger than in the R.H.=60% cases. Thus, for all cases when the condition of symmetric

instability is suggested by the  $\theta_e$  profile along M-surfaces, a relatively intense LLJ is developed. While in the present model framework, it is difficult to assess directly the possible roles of symmetric instability, the appearance of the slantwise convection structure seems to be an important factor in the occurrence of the equatorward secondary circulation.

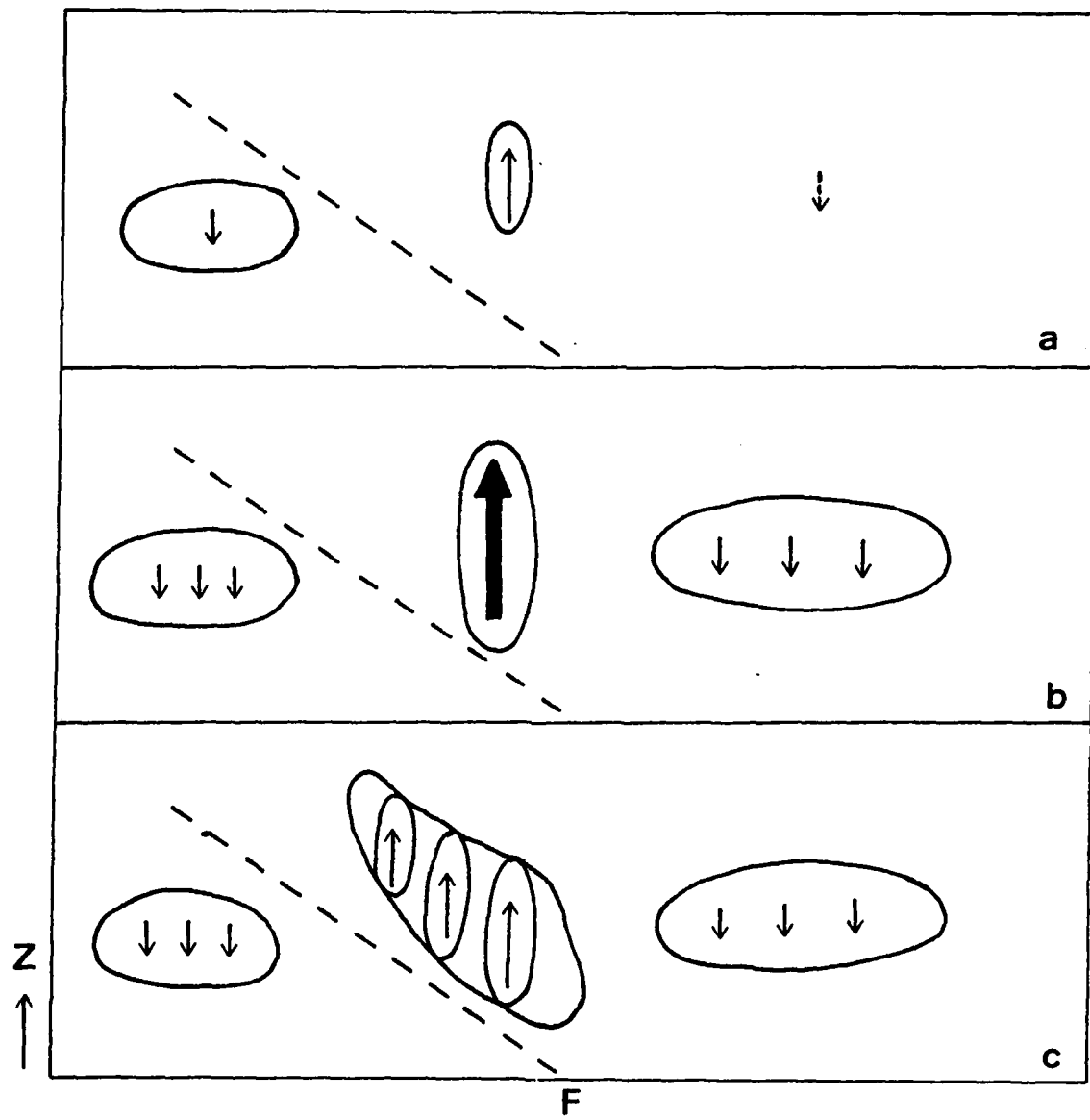


Fig. 4.1 Schematic diagram to show the differences between (a) frontal secondary circulation, (b) upright convection, and (c) slantwise convection.

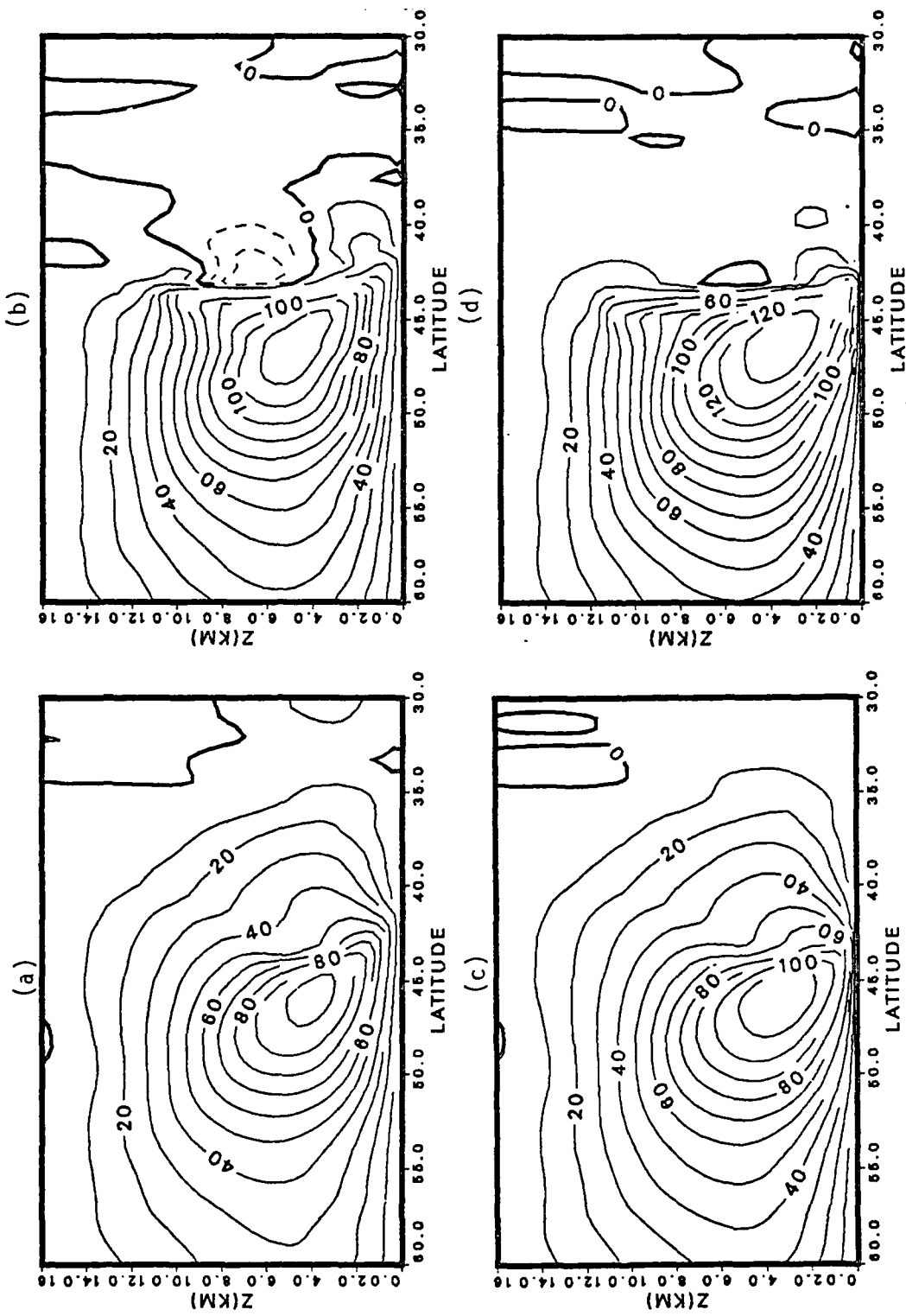


Fig. 4.2 Streamfunction,  $\psi$  ( $\text{mxcb s}^{-1}$ ) at day 4 for different midlatitude cases, (a) M60, (b) M61 and (d) M91.

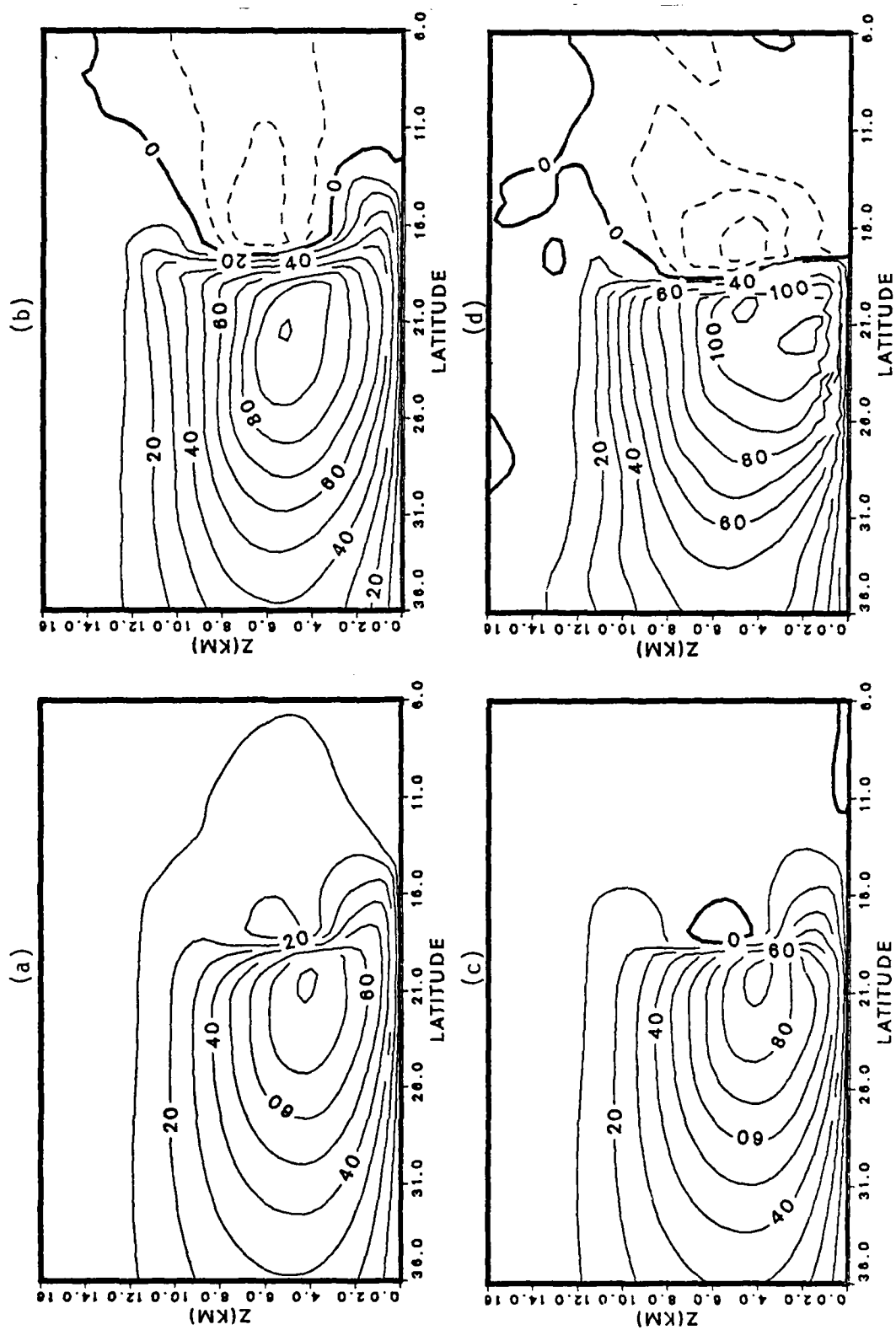
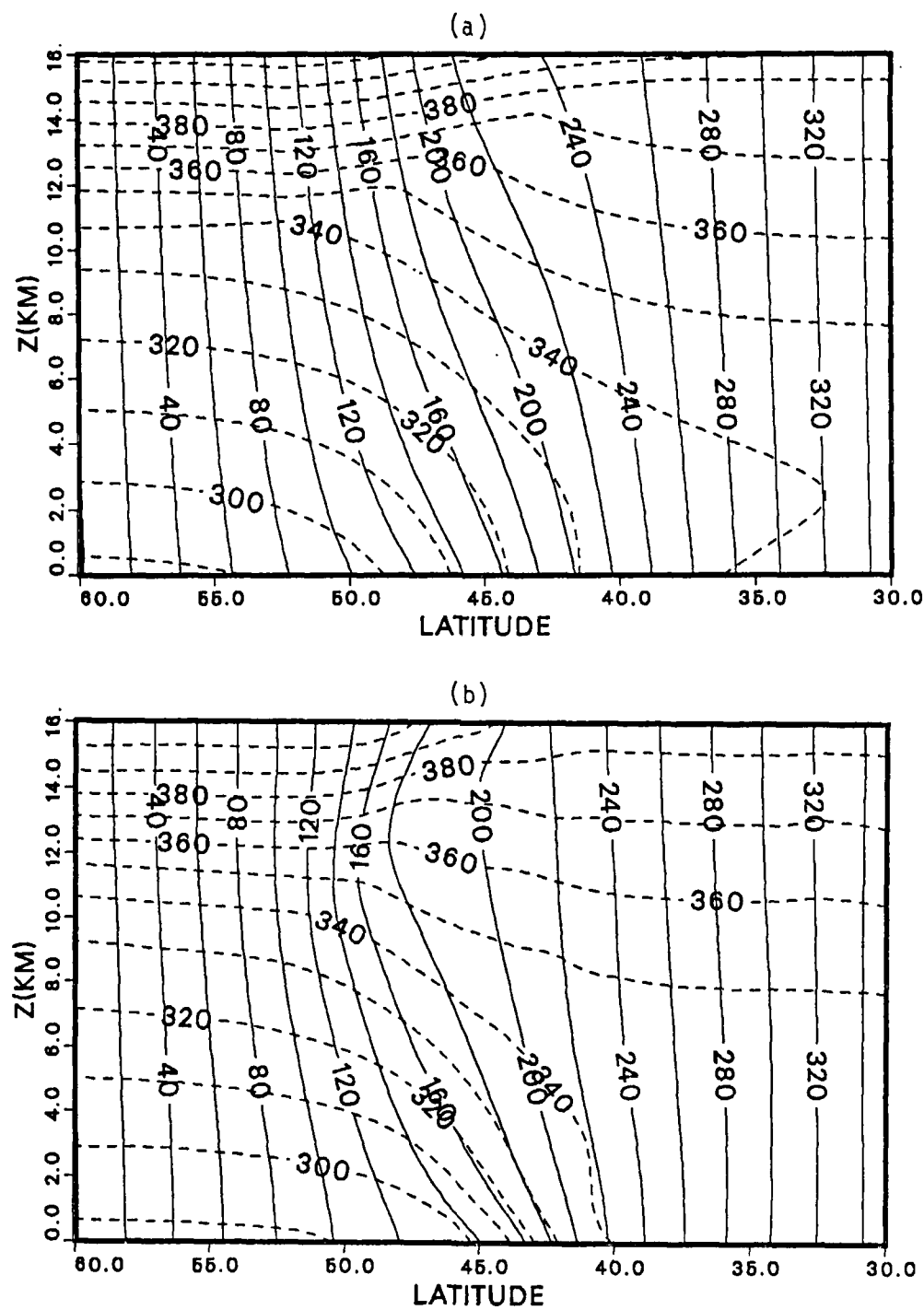


Fig. 4.3 24-hour averaged streamfunction,  $\psi$  ( $\text{m} \times \text{cb s}^{-1}$ ) at day 5 for different subtropical cases, (a) S60, (b) S90, (c) S61, and (d) S91.



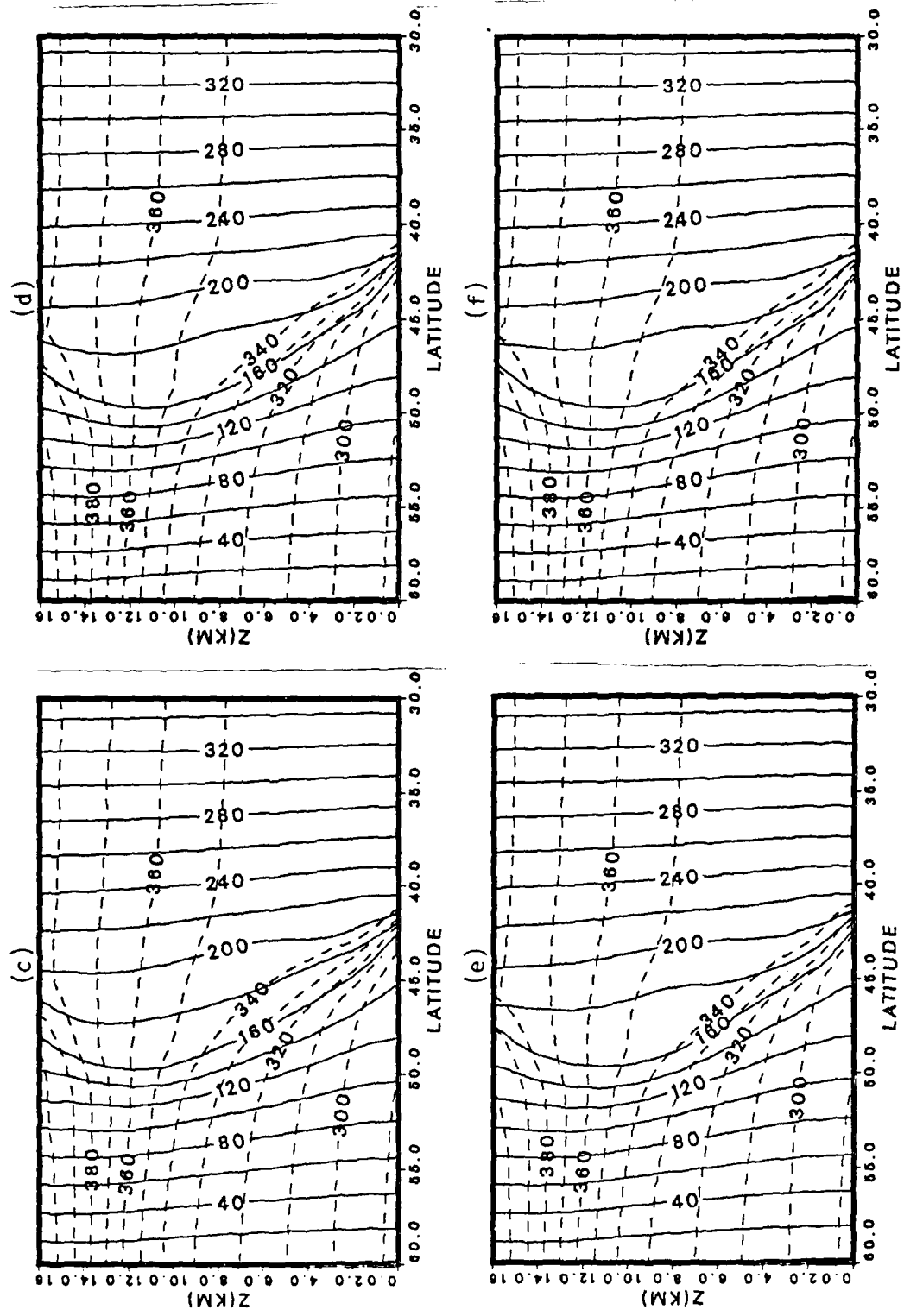


Fig. 4.4  
 (cont.)  
 Cross section of M-function (solid) in unit of  $m s^{-1}$  and equivalent potential temperature (dash),  $\theta_e(^{\circ}K)$  for typical midlatitude case, M60, at (c) day 2.0,  
 (d) day 3.0, (e) day 4.0 and (f) day 5.0.

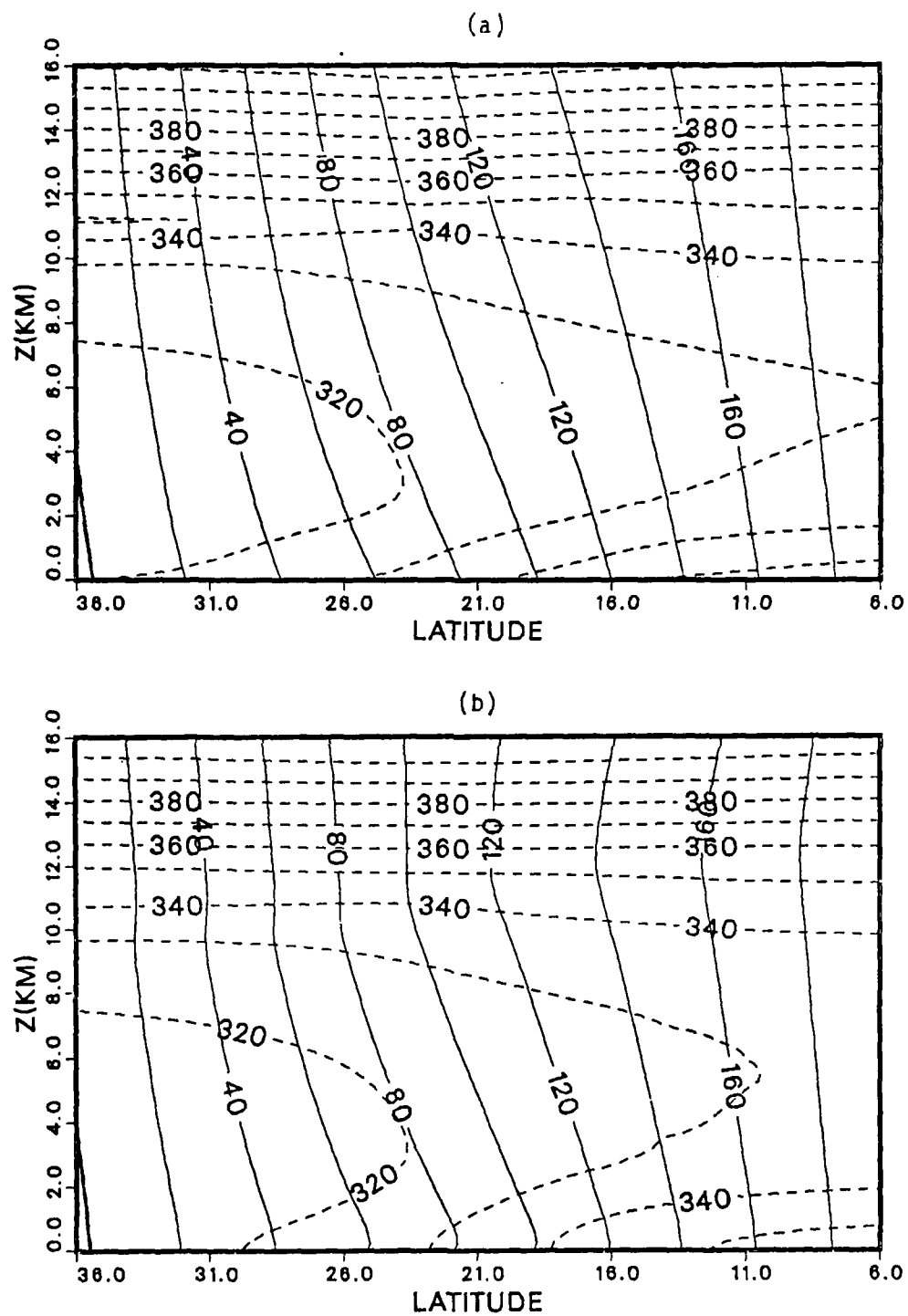


Fig. 4.5 Cross section of 24-hour averaged M-function (solid) in units of  $m s^{-1}$  and equivalent potential temperature (dash),  $\theta_e(^{\circ}K)$  for typical subtropical case, S90, at (a) day 0., (b) day 1.0.

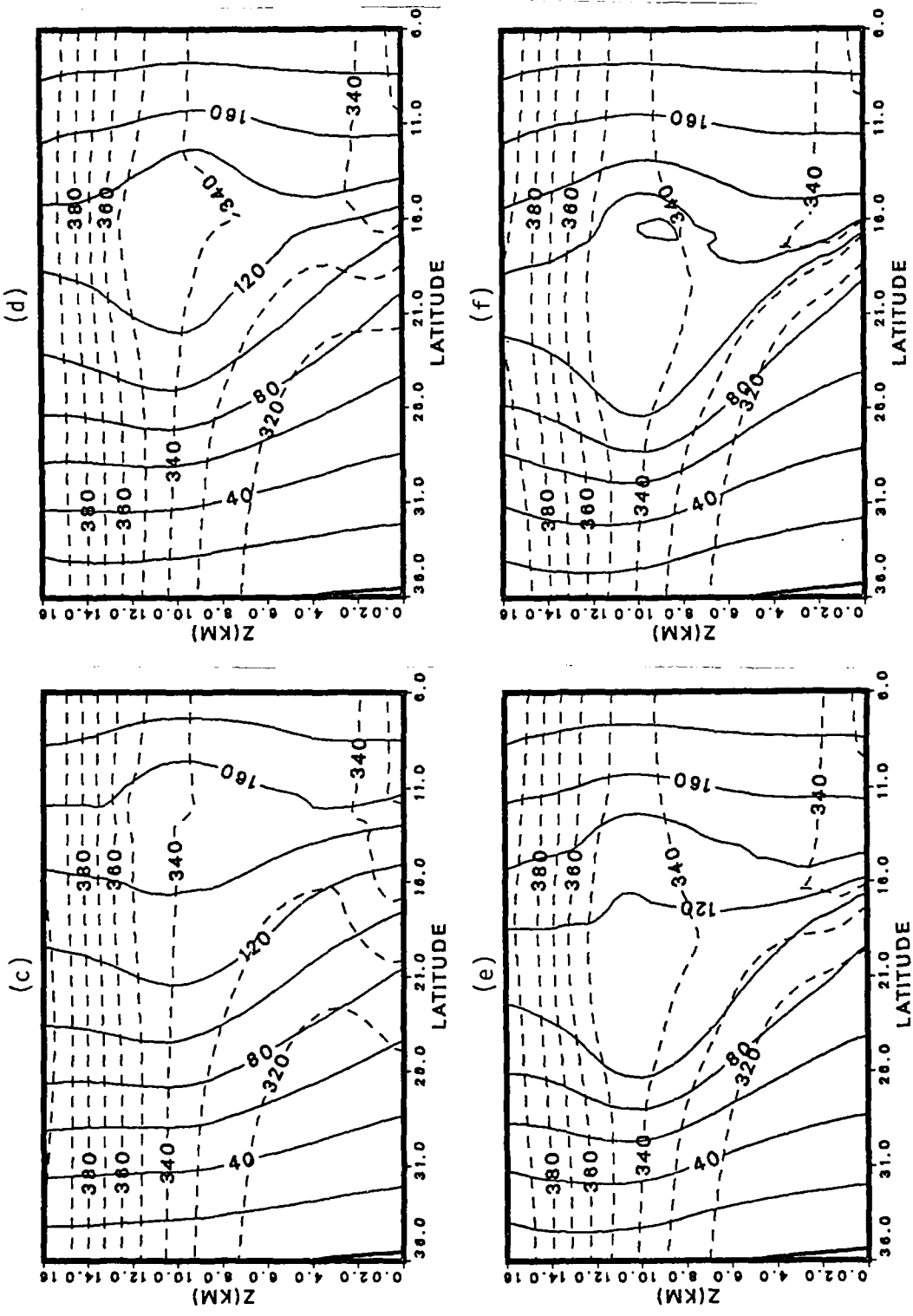
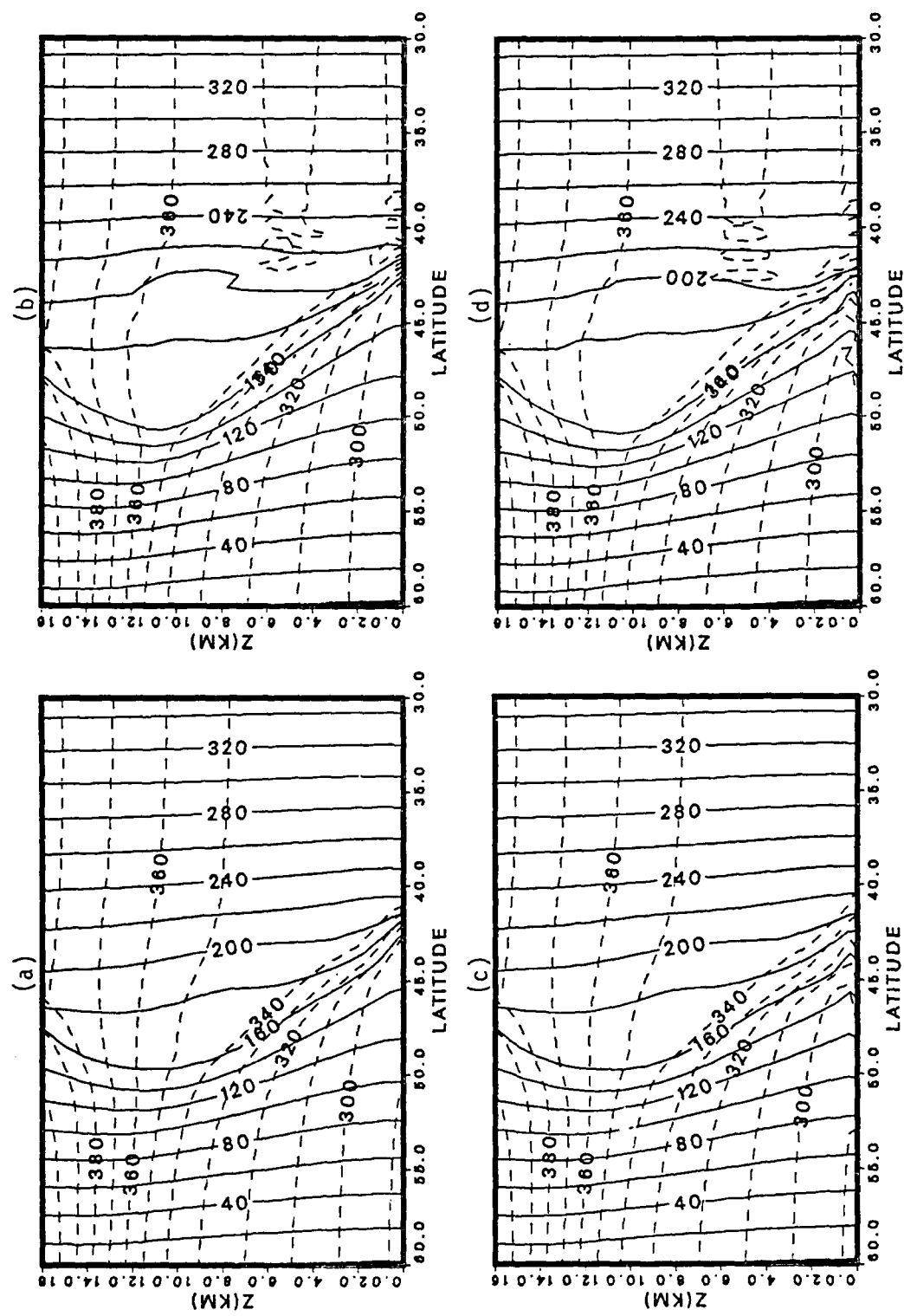


Fig. 4.5 Cross section of 24-hour averaged M-function (solid) in units of  $m s^{-1}$  and (cont.) equivalent potential temperature (dash),  $\theta_e(^{\circ}K)$  for typical subtropical case, S90, at (c) day 2.0, (d) day 3.0, (e) day 4.0 and (f) day 5.0.



As in Fig. 4.2, except for M-function (solid) in units of  $m^{-1}$  and equivalent potential temperature (dash),  $\theta_e(^{\circ}K)$ .

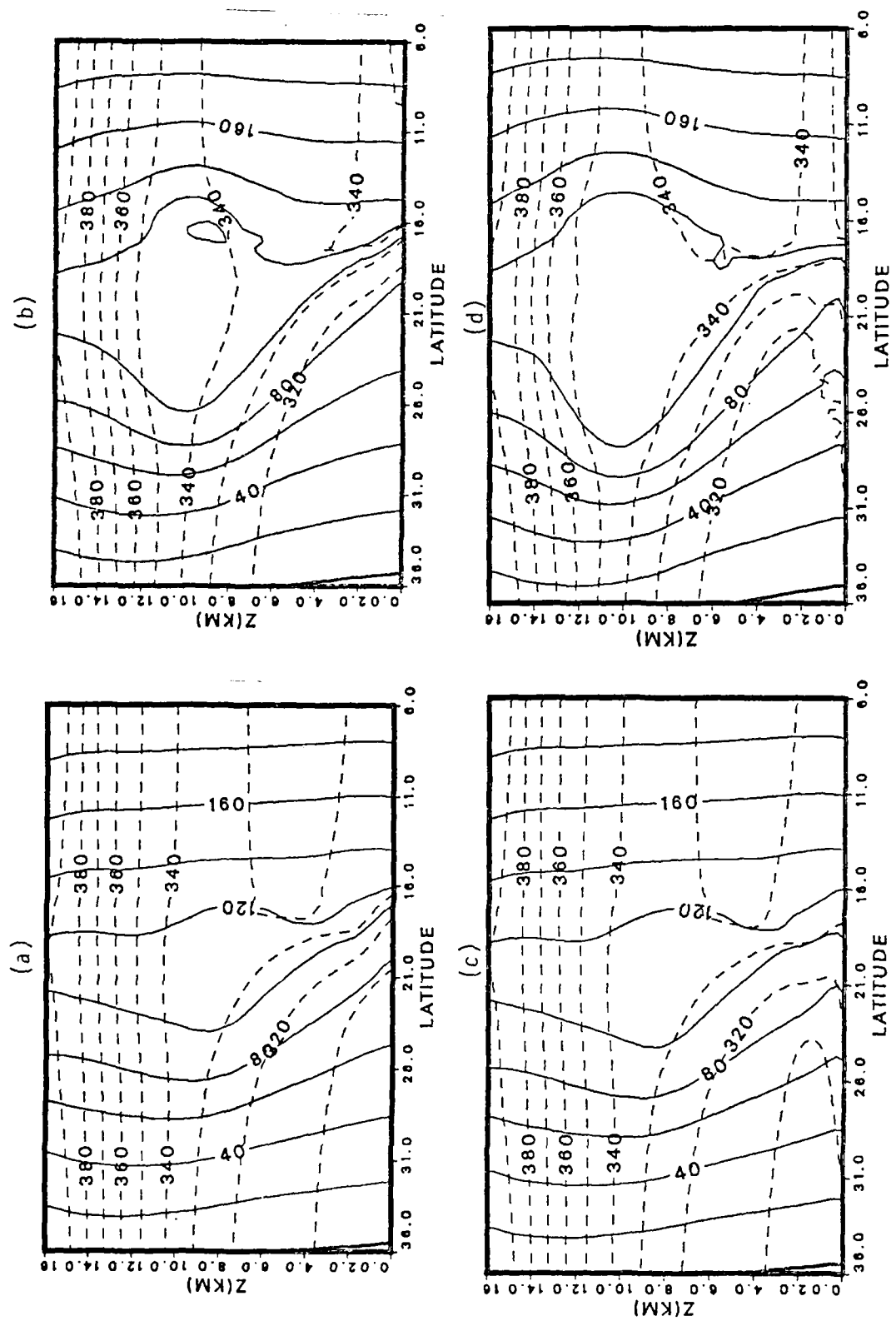


Fig. 4.7 As in Fig. 4.3, except for M-function (solid) in unit of  $\text{m s}^{-1}$  and equivalent potential temperature (dash),  $\theta_e(\text{eK})$ .

## V. SUMMARY AND CONCLUSIONS

In this work a two-dimensional frontal model is used to study the structure and behavior of the Mei-Yu front, with special emphasis on the dynamics of the low-level jet (LLJ) that is frequently observed ahead of the front. The Mei-Yu front develops in the area of the east Asian monsoon trough during early summer, and is the most important rain-producing system over east Asia outside of the typhoon season. This study is motivated by the unique mixed midlatitude-tropical properties of the Mei-Yu front (e.g., Chen and Chang, 1980), where heavy convection and strong low-level horizontal shear are associated with the nearly zonally-oriented front. The occurrence of the LLJ is highly correlated with heavy convective rainfall. The mechanism for the development of this LLJ is the main focus of this study.

In the numerical model, the time-varying response to a constant large-scale forcing was treated by a set of perturbation equations. The large-scale forcing was prescribed by a stretching deformation field which is characteristic of the frontogenetical forcing of the Mei-Yu front. The quasi-steady state responses to this forcing were obtained by integrating the perturbation equations from an initial state which is given by the seasonally-averaged zonal flow. Two major sets of experiments were conducted. The first is based on midlatitude conditions, where the

Coriolis parameter at  $46^{\circ}$  latitude and an initially stable sounding were chosen. The second is based on subtropical conditions, where the Coriolis parameter at  $22.5^{\circ}$  latitude and an initial sounding that is conditionally unstable was chosen. For each set of initial conditions, a number of supplemental cases were integrated to study the effects of varying initial humidity values and surface fluxes of momentum, heat and moisture. In the midlatitude cases, the quasi-steady state is reached within four days of integration. In the subtropical cases, small-scale features due to intense convection cause the motion field to fluctuate throughout the integration. A 24-hour averaging was applied at day 5 (96-120 h). This is considered the quasi-steady state as further integration shows that the motion remains quasi-steady.

For both midlatitude and subtropical experiments, the frontal zone develops equatorward of the dilation axis. The separation between the front and the dilation axis is greater for the subtropical cases than for the midlatitude cases. This larger separation is apparently due to the smaller  $f$  and, therefore, a relatively large ageostrophic secondary circulation around the frontal zone whose lower branch advects the surface front farther equatorward. The midlatitude front extends deeply into the upper troposphere with a strong poleward tilt, whereas the subtropical front is confined to the lower troposphere with less tilt, which

is in good agreement with observations (e.g., Chen and Chang, 1980). Along the sloping front, slantwise updrafts develop with a multi-band structure. This updraft is more evident in the subtropical cases and in the more moist midlatitude cases.

A westerly jet in the upper troposphere and an easterly jet in the lower troposphere develop in both midlatitude and subtropical cases, with smaller intensities in the subtropical cases. The inclusion of higher humidity or surface fluxes leads to stronger upper westerlies, apparently as a result of stronger cumulus convection. The lower level easterlies weaken both in the midlatitudes and the subtropics with the inclusion of surface fluxes. This is apparently due to the effect of momentum dissipation at the surface. An interesting feature in the zonal wind field in the subtropical cases is the concurrent development of upper-level easterlies and low-level westerlies equatorward of the front. The low-level westerly maximum at  $z = 3-4$  km resembles a LLJ, whose intensity increases when higher moisture is included. In the midlatitude cases, only a small downward and equatorward penetration of the upper westerlies appears in the similar area.

While several theories have been proposed for the development of low-level jets in the Mei-Yu and other circulation systems, the choice of the model set up prevents consideration of some of these theories as a possible

explanation for the simulated LLJ. The absence of terrain and diurnal radiation cycles in the model precludes the boundary-layer theories (Wexler, 1961; Holton, 1967; Blackadar, 1957), and the absence of a cumulus momentum transport parameterization precludes the mechanism due to cumulus momentum transport (Masomoto and Ninomiya, 1969; Ninomiya, 1971). In addition, the vertical coupling mechanism suggested by Uccellini and Johnson (1979) also does not apply in the Mei-Yu simulation, because the upper tropospheric westerly jet is located too far from the latitude of the LLJ (Fig. 1.4).

The appearance of an easterly regime in the upper troposphere on the equator side of the front above the LLJ suggests that the LLJ may be the result of a secondary circulation that resembles a "reversed Hadley" cell. This possibility is supported by the temperature distribution, which indicates that the "reversed Hadley" cell is actually a thermally direct circulation that is capable of maintaining the kinetic energy. The lower branch of this circulation is directed poleward toward the front, and it exerts a westerly Coriolis torque which can develop and maintain the LLJ. A meridional-vertical streamfunction reveals the structure of this secondary circulation, with a strong lower branch return flow coinciding with the development of a LLJ in the more moist, subtropical cases.

Several possible mechanisms may generate the reversed Hadley cell. The possibility that the reversed Hadley cell is a secondary circulation associated with the basic frontal structure was ruled out because in the drier midlatitude cases the frontal secondary circulation is a single cell around the front with upward motion on the equator side and downward motion on the pole side. No LLJ is developed in these cases. In the more moist (especially the subtropical) cases, the LLJ developed with the equator-side secondary circulation. This suggests the importance of cumulus convection in developing the reversed Hadley cell and the LLJ.

In all cases where a LLJ is developed, there is a sloping updraft with multi-band rising motion cells. This suggests that, besides regular "upright" convection due to conditional instability, slantwise convection arising out of symmetric instability may also be relevant. The roles of these two types of convection were studied by examining the evolution of the equivalent potential temperature distribution in the vertical and along the pseudo-angular momentum (M-function) surfaces. In the subtropical cases where the atmosphere is conditionally unstable initially, upright convection develops rapidly and the conditional instability is quickly released. During the early stages of the development, the M-function surface is nearly vertical, so that the condition for symmetric instability,  $(\partial\theta_e/\partial z)_M <$

0, is also given by that for conditional instability,  $(\partial\theta_e/\partial z)_y < 0$ . As the frontogenetical process continues, the M-surfaces in the frontal zone begin to slope and the condition for symmetric instability become different from that for conditional instability. As the conditionally unstable soundings adjusts to neutral, the  $\theta_e$  sounding along M surfaces is either neutral or slightly unstable in the middle-lower troposphere below 6 km. At this stage, slantwise convection is observed in the frontal zone and is indicative of the possible importance of symmetric instability processes.

In the more moist midlatitude cases, slantwise convection is also observed. In these cases, the frontal zone remains statically stable. However, the frontogenetic forcing produces slanted M surfaces there, with the  $\theta_e$  profiles on these surfaces reduced to only slightly stable based on the symmetric instability criterion. This result is in agreement with the recent theory of Emanuel (1985) who showed that, under frontogenetic forcing, sloping updrafts can occur in a concentrated region on the warm side of the frontal zone, and result in an enhanced secondary circulation. It also agrees with the observation by Sanders and Bosart (1985) of a mesoscale precipitation band in a winter-time extratropical cyclone over northeastern United States, in which a sloping updraft was observed in an

environment in which the symmetric stability was weakly positive.

The main findings of this study are that the LLJ in a subtropical Mei-Yu front can develop as a result of the Coriolis torque of a secondary circulation on the equator side of the front. This secondary circulation is thermally direct and is in the reversed Hadley sense. It is driven by intense condensation heating due to heavy precipitation. The upward motion takes the form of slantwise convection as a result of the frontogenesis forcing. The slantwise convection begins to appear after the atmosphere is stabilized by the convective adjustment. It is conceivable that, without the slantwise convection, which is concentrated along the frontal surface, the latent heat release would spread out over a broader area. This would give rise to a weaker secondary circulation. These conclusions are consistent with the observations that low-level jets are often associated with intense convection and heavy rainfall in the Mei-Yu front, and the indirect evidence of a sinking region south of the Baiu front as revealed by Matsumoto's (1972) moisture analysis. Further study is needed to clarify the possible roles of the symmetric instability mechanism. However, the strong in-phase correlation between the rising velocity and heating indicates that the main conclusion concerning the role of the secondary circulation should not depend on the details

of the formulation of condensation heating in the model. In fact, the frontal forcing is the dominating factor that determines the region of maximum rising motion. Given the moist subtropical environment for the Mei-Yu system, if a specified (instead of predicted) heating function is appropriately prescribed in the model, a strong secondary circulation equatorward of the front may also be expected.

Observational studies (e.g., Chen and Tsay, 1978) reported that the Mei-Yu convection and heavy rainfall are organized in mesoscale convective complexes (MCC), which can not be treated in the present two-dimensional model. A three-dimensional mesoscale numerical predication model, where the MCC's can be explicitly simulated, should be used to reexamine the relationship between the LLJ, secondary circulation and convection. A three-dimensional model is also necessary to study the entire life cycle of the Mei-Yu front and the LLJ. The development and decaying stages of the LLJ and the Mei-Yu front are of different time scales. While the Mei-Yu front usually persists for several days to one week or more, the appearance of the LLJ is more transient in nature. The time evolution of the LLJ within the quasi-steady Mei-Yu front is therefore an interesting topic for further studies.

The model may also be improved to study additional effects. The inclusion of a planetary boundary layer parameterization that is more sophisticated than the bulk

aerodynamics and is coupled with a diurnal radiation cycle will better represent the effects of friction, especially the interaction with radiation processes. The inclusion of terrain may be particularly important, since the Mei-Yu front is over the mountainous region of southern China, Taiwan and Japan. The topographical effect of the mountains and the land-sea complex in this region undoubtedly play an important role in both the large-scale front and the embedded mesoscale convective systems. In addition, Keyser and Anthes (1982, 1986) have argued that a stratification-dependent boundary layer effect is important for the intensity of vertical velocity in a surface front, while Mak and Bannon (1984) argued that condensation heating alone plays a more critical role. A sophisticated planetary boundary layer parameterization may help to clarify this issue. Finally, further observational studies are also necessary to investigate the Mei-Yu processes both in the planetary boundary layer as well as in the entire troposphere.

## Appendix

### A. SPECIFICATION OF MODEL GRIDS

The horizontal grids are uniform. The grid interval is 60 km. The pressure,  $p$ , is used as vertical coordinates and  $k$  is the vertical grid index. The pressure of  $k$ th level,  $p_k$ , in the model is specified by the exponential relationship with height,  $z_k$ ,

$$p_k = p_0 e^{-z_k} \quad (A.1)$$

where  $p_0$  is the pressure at the model bottom.

Apply (A.1) to the total height of the model,  $z_t$ ,

$$z_t = \ln\left(\frac{p_0}{p_t}\right) ,$$

where  $p_t$  is the pressure at model top.

Using uniform increment of height in vertical, the corresponding pressure is

$$p_k = p_0 e^{-\frac{(k-1)}{k_t} \ln\left(\frac{p_0}{p_t}\right)}$$

where  $k_t$  is the total number of vertical levels in the model.

In this study, the total number of vertical levels,  $k_t$ , is 54. The corresponding pressure levels used in the model are shown in Table A.1

TABLE A.1 FORECAST LEVELS (cb)

LEVEL	p(cb)		p(cb)		p(cb)
1	95.86	19	44.81	37	20.95
2	91.9	20	42.96	38	20.08
3	88.1	21	41.18	39	19.25
4	84.45	22	39.48	40	18.25
5	80.96	23	37.85	41	17.69
6	77.61	24	36.28	42	16.96
7	74.4	25	34.78	43	16.26
8	71.32	26	33.34	44	15.59
9	68.37	27	31.96	45	14.94
10	65.54	28	30.64	46	14.32
11	62.83	29	29.37	47	13.73
12	60.23	30	28.16	48	13.16
13	57.54	31	26.99	49	12.62
14	55.35	32	25.88	50	12.10
15	53.06	33	24.81	51	11.60
16	50.87	34	23.78	52	11.12
17	48.76	35	22.80	53	10.66
18	46.75	36	21.85	54	10.22

## B. GRID ARRANGEMENTS

The model grids and the all field variables are arranged as in Fig. B.1. The vertical level,  $\hat{p}$ , is the midpoint between levels of  $p$ . Vertical velocity is defined at  $p$  levels and the other variables  $u$ ,  $v$ ,  $\theta$ ,  $q$  and  $\pi$  are defined at  $\hat{p}$  levels. The horizontal grids are defined by  $y$  and  $\hat{y}$ . Variables  $\theta$ ,  $q$ ,  $\pi$  and  $\hat{\omega}$  are defined at  $y$  where  $\hat{\omega}_{j,k}$  is defined at  $y$  and  $p$  coordinates and is calculated from the continuity equation.

$$\hat{\omega}_{j,k} = \hat{\omega}_{j,k-1} - \frac{(p_k - p_{k-1})}{\hat{y}_j - \hat{y}_{j-1}} (v_{j,k-1} - v_{j-1,k-1})$$

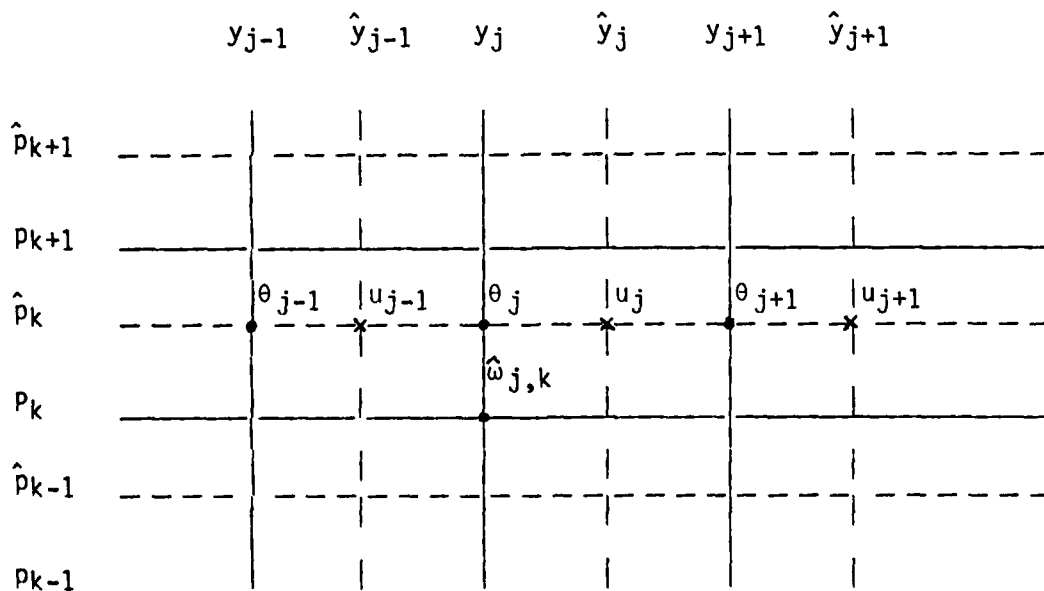


Fig. B.1 The model grid arrangement.

### C. FINITE DIFFERENCE FORMULATION

The equation set (2.1.16) and (2.1.19)-(2.1.23) can be integrated by a pure marching process. In this study a spatially staggered finite-difference scheme is used as compared to the unstaggered scheme used in Williams (1974). The variables  $\theta$ ,  $\pi$  and  $q$  are carried at the same points in  $y$ , and  $u$  and  $v$  are carried equidistant between these points (see Fig. B.1). Winninghoff (1968), Arakawa and Lamb (1977) and Schoenstadt (1980) have shown that this staggered grid, which is known as scheme B, is much better than the unstaggered grid (scheme A) for geostrophic adjustment. This scheme is especially superior when small-scale heating occurs, such as near a front. The nonlinear terms are arranged to conserve mean squares in the advection terms. Leapfrog time differencing is used, except the model is restarted every fifth timestep with an Euler backward step following Arakawa and Lamb (1977).

For the finite difference formulation, we discuss only the spatial derivative terms in the  $u$  and  $v$  equations [i.e., (2.1.16) and (2.1.19)],

$$\begin{aligned} \left[ \frac{\partial}{\partial y} vF \right]_{j,k} &= [(v_{j+1,k} + v_{j,k}) (F_{j+1,k} + F_{j,k}) \\ &\quad - (v_{j,k} + v_{j-1,k}) (F_{j,k} + F_{j-1,k})]/4(y_{j+1} - y_j) \end{aligned}$$

$$[\frac{\partial}{\partial y} \omega F]_{j,k} = [(\hat{\omega}_{j+1,k+1} + \hat{\omega}_{j,k+1}) (F_{j,k+1} + F_{j,k}) \\ - (\hat{\omega}_{j+1,k} + \hat{\omega}_{j,k}) (F_{j,k} + F_{j,k-1})]/4(p_{k+1} - p_k)$$

$$[\frac{\partial F}{\partial y}]_{j,k} = (F_{j+1,k} - F_{j-1,k})/(\hat{y}_{j+1} + \hat{y}_{j-1})$$

$$[\frac{\partial^2 F}{\partial y^2}]_{j,k} = [\frac{(F_{j+1,k} - F_{j,k})}{(\hat{y}_{j+1} - \hat{y}_j)} - \frac{(F_{j,k} - F_{j-1,k})}{(\hat{y}_j - \hat{y}_{j-1})}]/(y_{j+1} - y_j)$$

$$[\frac{\partial}{\partial p} K \frac{\partial F}{\partial p}]_{j,k} = [\frac{K_{k+1} (F_{j,k+1} - F_{j,k})}{(\hat{p}_{k+1} - \hat{p}_k)} - \frac{K_k (F_{j,k} - F_{j,k-1})}{(\hat{p}_k - \hat{p}_{k-1})}]/(p_{k+1} - p_k)$$

where  $F$  is either  $u$  or  $v$ .

For the  $\theta$  and  $q$  equations,

$$[\frac{\partial}{\partial y} vG]_{j,k} = [v_{j,k}(G_{j+1,k} + G_{j,k}) - v_{j-1,k}(G_{j,k} + G_{j-1,k})]/2(\hat{y}_j - \hat{y}_{j-1})$$

$$[\frac{\partial}{\partial y} wG]_{j,k} = [\hat{w}_{j,k+1}(G_{j,k+1} + G_{j,k}) - \hat{w}_{j,k}(G_{j,k} + G_{j,k-1})]/2(p_{k+1} - p_k)$$

$$[\frac{\partial G}{\partial y}]_{j,k} = (G_{j+1,k} - G_{j-1,k})/(y_{j+1} - y_{j-1})$$

$$[\frac{\partial^2 G}{\partial y^2}]_{j,k} = [\frac{(G_{j+1,k} - G_{j,k})}{(y_{j+1} - y_j)} - \frac{(G_{j,k} - G_{j-1,k})}{(y_j - y_{j-1})}]/(\hat{y}_j - \hat{y}_{j-1})$$

$$[\frac{\partial}{\partial p} K \frac{\partial G}{\partial p}]_{j,k} = [\frac{K_{k+1}(G_{j,k+1} - G_{j,k})}{(\hat{p}_{k+1} - \hat{p}_k)} - \frac{K_k(G_{j,k} - G_{j,k-1})}{(\hat{p}_k - \hat{p}_{k-1})}]/(p_{k+1} - p_k)$$

where  $G$  is either  $\theta$  or  $q$ .

#### LIST OF REFERENCES

Akiyama, T., 1973a: The large-scale aspects of the characteristic features of the Baiu front. Paper Meteoro. Geophy., 24, 157-188.

Akiyama, T., 1973b: Frequent occurrence of heavy rainfall along the north side to the low-level jet stream in the Baiu season. Paper Meteoro. Geophy., 24, 379-388.

Akiyama, T., 1974: Mesoscale organization of cumulus convection in the large-scale rainband in the Baiu season. J. Meteor. Soc. Japan, 52, 448-451.

Akiyama, T., 1978: Mesoscale pulsation of convective rain in medium-scale disturbances developed in Baiu front. J. Meteor. Soc. Japan, 56, 267-273.

Arakawa, A., and V. R. Lamb, 1977: Computational design of the basic dynamical processes of the UCLA general circulation model. Methods in Computational Physics, Vol. 17, Academic Press, 174-265.

Bennetts, D. A., and B. J. Hoskins, 1979: Conditional symmetric instability - a possible explanation for frontal rainbands. Quart. J. Roy. Meteor. Soc., 105, 945-962.

Bennetts, D. A., and J. C. Sharp, 1982: The relevance of conditional symmetric instability to the prediction of mesoscale frontal rainbands. Quart. J. Roy. Meteor. Soc., 108, 595-602.

Blackadar, A. K., 1957: Boundary layer wind maxima and their significance for the growth of nocturnal inversions. Bull. Amer. Meteor. Soc., 38, 283-290.

Bonner, W. D., 1968: Climatology of the low level jet. Mon. Wea. Rev., 96, 833-850.

Browning, K. A., and T. W. Harrold, 1970: Air motion and precipitation growth at a cold front. Quart. J. Roy. Meteor. Soc., 96, 369-389.

Browning, K. A., and C. W. Pardoe, 1973: Structure of low level jet streams ahead of mid-latitude cold fronts. Quart. J. Roy. Meteor. Soc., 99, 619-638.

Byers, H. R., 1974: General Meteorology, McGraw Hill Book Company, New York, 461 pp.

Chen, G. T. J., 1977: A synoptic case study on mean structure of Mei-Yu in Taiwan. Atmos. Sci., Meteor. Soc. Rep. of China, 4, 38-47.

Chen, G. T. J., 1977: An analysis of moisture structure and rainfall for a Mei-Yu regime in Taiwan. Proc. Natl. Sci. Counc., 1, 11, 1-21.

Chen, G. T. J., 1978: The structure of a subtropical Mei-Yu system in Southeast Asia. Dept. Atmos. Sci., Natl. Taiwan Univ., Sci. Rep., 2, 9-23.

Chen, G. T. J., 1983: Observational aspects of the Mei-Yu phenomenon in subtropical China. J. Meteor. Soc. Japan, 61, 306-312.

Chen, G. T. J., and C. Y. Tsay, 1978: A synoptic case study of Mei-Yu near Taiwan. Papers Meteor. Res., 1, 25-36.

Chen, G. T. J., and C.-P. Chang, 1980: The structure and vorticity budget of an early summer monsoon trough (Mei-Yu) over southeastern China and Japan. Mon. Wea. Rev., 108, 942-953.

Chen, G. T. J., and S. S. Chi, 1980: On the frequency and speed of Mei-Yu front over southern China and the adjacent areas. Papers Meteor. Res., 3, 1 & 2, 31-42.

Chen, G. T. J., S. Y. Chen, and M. H. Yan, 1983: The winter diurnal circulation and its influence on precipitation over the coastal area of northern Taiwan. Mon. Wea. Rev., 111, 2269-2274.

Chen, O., 1982: The instability of the gravity-inertia wave and its relation to low-level jet and heavy rainfall. J. Meteor. Soc. Japan, 60, 1041-1057.

Djuric, D., and M. S. Damiani, Jr., 1980: On the formation of the low-level jet over Texas. Mon. Wea. Rev., 108, 1854-1865.

Djuric, D., and D. S. Ladwig, 1983: Southerly low-level jet in the winter cyclones of the southwestern great plains. Mon. Wea. Rev., 111, 2275-2281.

Emanuel, K. A., 1979: Inertial instability mesoscale convective systems. Part I: Linear theory of inertial instability in rotating viscous fluid. J. Atmos. Sci., 36, 2425-2449.

Emanuel, K. A., 1982: A variational theorem for circulation integrals applied to inviscid symmetric flows with variable stability and shear. Quart. J. Roy. Meteor. Soc., 108, 825-832.

Emanuel, K. A., 1983a: The Lagrangian parcel dynamics of moist symmetric instability. J. Atmos. Sci., 40, 2368-2376.

Emanuel, K. A., 1983b: On assessing local conditional symmetric instability from atmospheric soundings. Mon. Wea. Rev., 111, 2016-2033.

Emanuel, K. A., 1985: Frontal circulations in the presence of small moist symmetric stability. J. Atmos. Sci., 42, 1062-1071.

Haltiner, G. J., and F. L. Martin, 1957: Dynamical and Physical Meteorology. McGraw Hill Book Company, New York, 470 pp.

Hess, S. L., 1959: Introduction to Theoretical Meteorology. Henry Holt and Company, New York, 362 pp.

Hobbs, P. V., 1978: Organization and structure of clouds and precipitation on the mesoscale and microscale in cyclonic storms. Rev. Geophys. Space Phys., 16, 741-755.

Holton, J. R., 1967: The diurnal boundary layer wind oscillation above sloping terrain. Tellus, 19, 199-205.

Hoskins, B. J., 1975: The geostrophic momentum approximation and the semi-geostrophic equations. J. Atmos. Sci., 32, 233-242.

Hoskins, B. J., and F. P. Bretherton, 1972: Atmospheric frontogenesis models: Mathematical formulation and solution. J. Atmos. Sci., 29, 11-37.

Hoskins, B. J., and I. Draghici, 1977: The forcing of ageostrophic motion according to the semi-geostrophic equations and in an isentropic coordinate model. J. Atmos. Sci., 34, 1859-1867.

Hsie, E. Y., and R. A. Anthes, 1984: Simulation of frontogenesis in a moist atmosphere using alternative parameterizations of condensation precipitation. J. Atmos. Sci., 41, 2701-2716.

Hsueh, Y., 1970: A note on the boundary layer wind structure above sloping terrain. J. Atmos. Sci., 27, 322-327.

Keyser, D., and R. A. Anthes, 1982: The influence of planetary boundary layer physics on frontal structure in the Hoskins-Bretherton horizontal shear model. J. Atmos. Sci., 39, 1783-1802.

Keyser, D., and R. A. Anthes, 1986: Comments on "Frontogenesis in a moist semigeostrophic model." J. Atmos. Sci., 43, 1051-1054.

Lettau, H. H., 1967: Small to large scale features of boundary structures over mountain slopes. Proc. Symp. Mountain Meteor., Colorado State University, 1-74.

Mak, M., and P. R. Bannon, 1984: Frontogenesis in a moist semigeostrophic model. J. Atmos. Sci., 41, 3485-3500.

Matsumoto, S., 1972: Unbalanced low-level jet and solenoidal circulation associated with heavy rainfalls. J. Meteor. Soc. Japan, 50, 194-203.

Matsumoto, S., 1973: Lower tropospheric wind speed and precipitation activity. J. Meteor. Soc. Japan, 51, 101-107.

Matsumoto, S., and K. Ninomiya, 1969: On the role of convective momentum exchange in the mesoscale gravity wave. J. Meteor. Soc. Japan, 47, 75-85.

Matsumoto, S., S. Yoshizumi, and M. Takeuchi, 1970: On the structure of the "Baiu" front and the associated intermediate-scale disturbances in the lower atmosphere. J. Meteor. Soc. Japan, 48, 479-491.

Matsumoto, S., K. Ninomiya, and S. Yoshizumi, 1971: Characteristic features of "Baiu" front associated with heavy rainfall. J. Meteor. Soc. Japan, 49, 267-281.

Moore, G. W. K., 1985: The organization of convection in narrow cold-frontal rainbands. J. Atmos. Sci., 42, 1777-1791.

Naistat, R. J., and J. A. Young, 1973: A linear model of boundary layer flow applied to the St. Patrick's Day storm of 1965. J. Appl. Meteor., 12, 1151-1162.

Newton, C. W., 1956: Mechanisms of circulation change during a lee cyclogenesis. J. Meteor., 13, 528-539.

Newton, C. W., 1967: Severe convective storms. Advances in Geophysics, Vol. 12, Academic Press, 257-303.

Ninomiya, K., 1971: Mesoscale modification of synoptic situation from thunderstorm development as revealed by ATS III and aerological data. J. Appl. Meteor., 10, 1103-1121.

Ninomiya, K., 1980: Mesoscale aspects of heavy rainfalls in the Japan islands. Proceedings of CIMMS Symposium, 110-188.

Ninomiya, K., and T. Akiyama, 1971: The development of the medium-scale disturbances in the Baiu front. J. Meteor. Soc. Japan, 49, 663-677.

Ninomiya, K., and T. Akiyama, 1972: Medium-scale echo clusters in the Baiu front as revealed by multi-radar composite echo maps. (Part I). J. Meteor. Soc. Japan, 50, 558-569.

Ninomiya, K., and T. Akiyama, 1973: Medium-scale echo clusters in the Baiu front as revealed by multi-radar composite echo maps. (Part II). J. Meteor. Soc. Japan, 51, 108-118.

Ninomiya, K., and T. Akiyama, 1974: Band structure of mesoscale echo cluster associated with low-level jet stream. J. Meteor. Soc. Japan, 52, 300-313.

Paegle, J., 1978: A linearized analysis of diurnal boundary layer convergence over the topography of the United States. Mon. Wea. Rev., 106, 492-502.

Paegle, J., and G. E. Rasch, 1973: Three-dimensional characteristics of diurnally varying boundary-layer flows. Mon. Wea. Rev., 101, 746-756.

Parsons, D. B., and P. V. Hobbs, 1983: The mesoscale and microscale structure and organization of clouds and precipitation in midlatitude cyclones. XI: Comparisons between observational and theoretical aspects of rainbands. J. Atmos. Sci., 40, 2377-2397.

Reiter, E. R., 1969: Tropopause circulation and jet streams. World Survey of Climatology, Vol. 4: Climate of the Free Atmosphere. D. F. Rex, Ed., Elsevier, 85-193.

Ross, B. B., and I. Orlanski, 1978: The circulation associated with a cold front. Part II: Moist case. J. Atmos. Sci., 35, 445-465.

Sanders, F., and L. Bosart, 1985: Mesoscale structure in the megalopolitan snowstorm of 11-12 February 1983. J. Atmos. Sci., 42, 1050-1061.

Schoenstadt, A. L., 1980: A transfer function analysis of numerical schemes used to simulate geostrophic adjustment. Mon. Wea. Rev., 108, 1248-1259.

Stone, P. H., 1966: Frontogenesis by horizontal wind deformation fields. J. Atmos. Sci., 23, 455-465.

Tao, S.-Y., 1980: Severe Rainstorms in China. Science Press, Beijing, 223 pp (in Chinese).

Tao, S.-Y., and Y.-H. Ding, 1981: Observational evidence of the influence of the Qinghai-Xizang (Tibet) Plateau on the occurrence of heavy rain and severe convective storms in China. Bull. Amer. Meteor. Soc., 62, 23-30.

Tao, S.-Y., and L.-X. Chen, 1987: A review of recent research on the East Asian summer monsoon in China. Reviews in Monsoon Meteorology. C.-P. Chang and Krishnamurti, Eds., Oxford University Press (to be published).

Thorpe, A. J., and K. A. Emanuel, 1985: Frontogenesis in the presence of small stability to slantwise convection. J. Atmos. Sci., 42, 1809-1824.

Thorpe, A. J., and C. A. Nash, 1984: Convective and boundary layer parameterizations in a diagnostic model of atmospheric fronts. Quart. J. Roy. Meteor. Soc., 110, 443-466.

Tsay, C. Y., and G. T. J. Chen, 1980: Dynamic processes for vertical motions in a Mei-Yu system. Papers Meteor. Res., 3, 67-77.

Uccellini, L. W., 1980: On the role of upper tropospheric jet streaks and lee side cyclogenesis in the development of low-level jet in the great plains. Mon. Wea. Rev., 108, 1689-1696.

Uccellini, L. W., and D. R. Johnson, 1979: The coupling of upper and lower tropospheric jet streaks and implications for the development of severe convective storms. Mon. Wea. Rev., 107, 682-703.

Wexler, H., 1961: A boundary layer interpretation of the low-level jet. Tellus, 13, 368-378.

Williams, R. T., 1967: Atmospheric frontogenesis: A numerical experiment. J. Atmos. Sci., 24, 627-641.

Williams, R. T., 1968: A note on quasi-geostrophic frontogenesis. J. Atmos. Sci., 25, 1157-1159.

Williams, R. T., 1972: Quasi-geostrophic versus non-geostrophic frontogenesis. J. Atmos. Sci., 29, 3-10.

Williams, R. T., 1974: Numerical simulation of steady-state fronts. J. Atmos. Sci., 31, 1286-1296.

Williams, R. T., and J. Plotkin, 1968: Quasi-geostrophic frontogenesis. J. Atmos. Sci., 25, 201-206.

Williams, R. T., L. C. Chou and C. J. Cornelius, 1981: Effects of condensation and surface motion on the structure of steady-state fronts. J. Atmos. Sci., 38, 2365-2376.

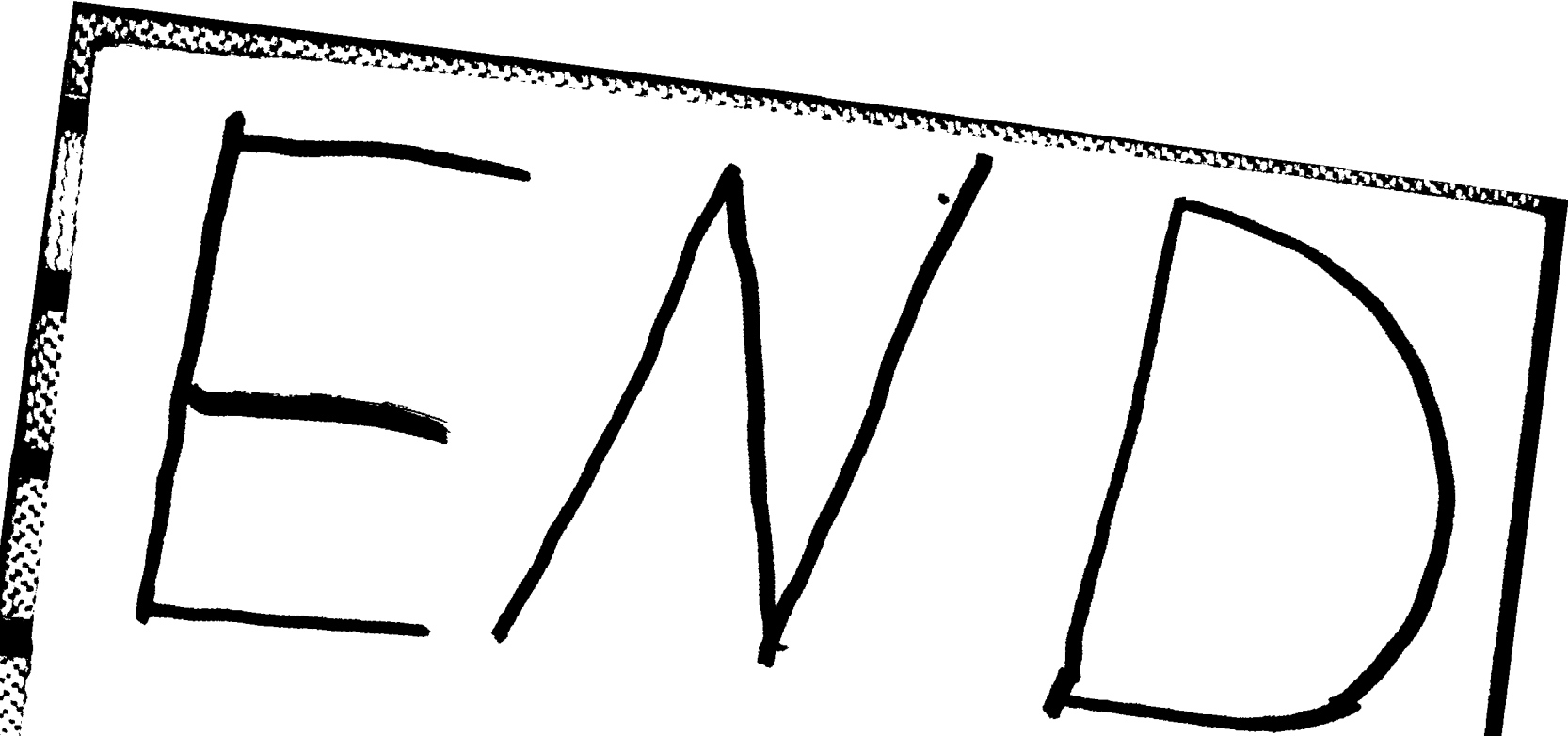
Winninghoff, F. J., 1968: On the adjustment toward a geostrophic balance in a simple primitive equation model with application to problems of initialization and objective analysis. Ph.D. thesis, Department of Meteorology, UCLA, 161 pp.

INITIAL DISTRIBUTION LIST

	No. of copies
1. Defense Technical Information Center Cameron Station Alexandria, Virginia 22304-6145	2
2. Library, Code 0142 Naval Postgraduate School Monterey, California 93943-5002	2
3. Professor R. J. Renard, Code 63Rd Naval Postgraduate School Monterey, California 93943	1
4. Professor C.-P. Chang, Code 63Cp Naval Postgraduate School Monterey, California 93943	4
5. Professor R. T. Williams, Code 63Wu Naval Postgraduate School Monterey, California 93943	4
6. Mr. Lang C. Chou, Code 63Cq Naval Postgraduate School Monterey, California 93943	4
7. Director Naval Oceanography Division Naval Observatory 34th and Massachusetts Avenue NW Washington, D. C. 20309	1
8. Commander Naval Oceanography Command NSTL Station Bay St. Louis, Mississippi 39522	1
9. Commanding Officer Naval Oceanographic Office NSTL Station Bay St. Louis, Mississippi 39522	1
10. Commanding Officer Fleet Numerical Oceanography Center Monterey, California 93940	1
11. Commanding Officer Naval Environmental Prediction Research Facility Monterey, California 93940	1

12.	Chief of Naval Research 800 N. Quincy Street Arlington, Virginia 22217	1
13.	Office of Naval Research, Code 1122 800 N. Quincy Street Arlington, Virginia 22217	1
14.	Professor R. L. Elsberry, Code 63Es Naval Postgraduate School Monterey, California 93943	1
15.	Professor G. T. J. Chen Department of Atmospheric Sciences National Taiwan University Taipei, Taiwan	1
16.	Professor C. Y. Tsay Department of Atmospheric Sciences National Taiwan University Taipei, Taiwan	1
17	Dr. Arakawa Department of Meteorology University of California Los Angles, California 90024	1
18	Dr. B. J. Hoskins Department of Geophysics University of Reading Reading, United Kingdom	1
19	Dr. J. Young Department of Meteorology University of Wisconsin Madison, Wisconsin 53706	1
20	Dr. A. Kasahara National Center for Atmospheric Research P. O. Box 3000 Boulder, Colorado 80303	1
21	Prof. N. A. Phillips National Meteorological Center/NOAA World Weather Building Washington, D. C. 20233	1
22	Dr. T. Rosmond Naval Environmental Prediction Research Facility Monterey, California 93943	1

23	Prof. A. L. Schoenstadt, Code 53Zh Naval Postgraduate School Monterey, California 93943	1
24	Dr. M. J. P. Cullen Meteorological Office Bracknell, Berks, United Kingdom	1
25	Dr. Andrew Staniforth Recherche en Prevision Numerique West Isle Office Tower, 5 ieme etage 2121 route Trans-Canada Dorval, Quebec H9P1J3, Canada	1
26	Dr. J. Hoverrmale Naval Environmental Prediction Research Facility Monterey, California 93943	1
27	Prof. W. Blumen Campus Box 391 University of Colorado Boulder, Colorado 80309	1
28	Dr. M. Peng, Code 63Pg Naval Postgraduate School Monterey, California 93943	1
29	Dr. R. B. Smith Department of Geology and Geophysics Yale University P. O. Box 6666 New Haven, Connecticut 06511	1
30	Dr. Peter Bannon Department of Geophysical Sciences University of Chicago Chicago, Illinois 60637	1
31	Dr. R. Gall Institute of Atmospheric Physics The University of Arizona Tucson, Arizona 85721	1



2- 81-

